The role of phase transformation as a softening mechanism in saline ice
by Ladean Robert McKittrick

A thesis submitted in partial fulfillment of the requirements for the degree of Doctor of Philosophy in Engineering Applied Mechanics
Montana State University

Abstract:
To gain insight into the behavior of saline ice relative to non-saline ice, single crystals of saline and non-saline ice were loaded in compression. Responses from these experiments indicate that single crystals of saline ice are significantly more compliant during the initial load response. Analyses presented in this dissertation indicate that phase transformations in brine cells have the potential to play a significant role in increasing the compliance of saline ice during the initial load response.

Cooling of a sealed brine cell, leading to the precipitation of ice, provides a mechanism for the accumulation of "large" localized stresses. Based on mathematical models, this mechanism has the potential to be a significant source for the nucleation or multiplication of dislocations, and can conceivably make a significant contribution to the greater compliance (softness) of saline ice relative to non-saline ice. These results are consistent with the observation that laboratory grown saline crystals sometimes display extensive differences in mechanical behavior that appears to be due to variations in the growth and storage conditions experienced by the crystals.

The brine cell model presented in this dissertation indicates that there is a transition in deformation modes for brine cell cooling rates on the order of 0.1 °C hr-1. At lower rates, local deformation is dislocation dominated; at higher rates, it is fracture dominated. Whether the pressure build-up in a cooling brine cell is relieved by inelastic deformation or cracking, the change in the internal structure is likely to play a role in the macroscopic behavior of saline ice. In particular, with the proper temperature history, the phase transformation mechanism can significantly increase the density of dislocations, and can therefore make a significant contribution to the macroscopic compliance of saline ice.

THE ROLE OF PHASE TRANSFORMATIONS AS A SOFTENING MECHANISM IN SALINE ICE

by

Ladean Robert McKittrick

A thesis submitted in partial fulfillment
of the requirements for the degree

of

Doctor of Philosophy

in

Engineering

Applied Mechanics

MONTANA STATE UNIVERSITY-BOZEMAN
Bozeman, Montana

May 1997

APPROVAL

of a thesis submitted by

Ladean Robert McKittrick

This thesis has been read by each member of the thesis committee and has been found to be satisfactory regarding content, English usage, format, citations, bibliographic style, and consistency, and is ready for submission to the College of Graduate Studies.

Robert Brown — (Signature) — Date 5/19/97

Approved for the Department of Civil Engineering

Donald Raburn — (Signature) — Date 5/15/97

Approved for the College of Graduate Studies

Robert Brown — (Signature) — Date 5/19/97

STATEMENT OF PERMISSION TO USE

In presenting this thesis in partial fulfillment of the requirements for a doctoral degree at Montana State University-Bozeman, I agree that the Library shall make it available to borrowers under rules of the Library. I further agree that copying of this thesis is allowable only for scholarly purposes, consistent with "fair use" as prescribed in the U.S. Copyright Law. Requests for extensive copying or reproduction of this thesis should be referred to University Microfilms International, 300 North Zeeb Road, Ann Arbor, Michigan 48106, to whom I have granted "the exclusive right to reproduce and distribute my dissertation for sale in and from microform or electronic format, along with the non-exclusive right to reproduce and distribute my abstract in any format in whole or in part."

Signature Lindsay M. Kittredge

Date 15 MAY 97

TABLE OF CONTENTS

LIST OF TABLES

LIST OF FIGURES

ABSTRACT

To gain insight into the behavior of saline ice relative to non-saline ice, single crystals of saline and non-saline ice were loaded in compression. Responses from these experiments indicate that single crystals of saline ice are significantly more compliant during the initial load response. Analyses presented in this dissertation indicate that phase transformations in brine cells have the potential to play a significant role in increasing the compliance of saline ice during the initial load response.

Cooling of a sealed brine cell, leading to the precipitation of ice, provides a mechanism for the accumulation of "large" localized stresses. Based on mathematical models, this mechanism has the potential to be a significant source for the nucleation or multiplication of dislocations, and can conceivably make a significant contribution to the greater compliance (softness) of saline ice relative to non-saline ice. These results are consistent with the observation that laboratory grown saline crystals sometimes display extensive differences in mechanical behavior that appears to be due to variations in the growth and storage conditions experienced by the crystals.

The brine cell model presented in this dissertation indicates that there is a transition in deformation modes for brine cell cooling rates on the order of 0.1 °C hr^{-1}. At lower rates, local deformation is dislocation dominated; at higher rates, it is fracture dominated. Whether the pressure build-up in a cooling brine cell is relieved by inelastic deformation or cracking, the change in the internal structure is likely to play a role in the macroscopic behavior of saline ice. In particular, with the proper temperature history, the phase transformation mechanism can significantly increase the density of dislocations, and can therefore make a significant contribution to the macroscopic compliance of saline ice.

CHAPTER 1

INTRODUCTION

On the subject of sea ice, there are two classes of problems that are of primary concern to the engineering community. The first class of problems concerns the maximum force that ice can exert on structures. These interaction forces can occur between a moving ice sheet and a stationary structure (e.g., oil drilling platforms) or between a stationary ice sheet and a moving structure (e.g., ice breakers). The second class of problems concerns the safe bearing capacity of ice covers under static or moving loads (e.g., airplanes).

This dissertation presents a set of observed variations in the initial load response of saline ice and a possible explanation for these observed variations. The analyses and observations presented provide evidence that phase transformation mechanisms can significantly increase the initial compliance of saline (NaCl) ice. The relevance of the proposed phase transformation mechanism is then extended, in an approximate sense, to sea ice. An understanding of these initial load response variations is necessary if the ice-structure interaction forces are to be modeled in a knowledgeable fashion.

Purpose

The intent of this dissertation is to present, in some detail, the role that phase transformations might play in the observed variations in the initial compliance of saline ice. Phase transformations are also considered as the mechanism that leads

to distinct and somewhat unexpected differences between the initial load responses of saline and non-saline ice crystals. The potential role that phase transformations might play in the structural response is also extended to sea ice.

Overview

Relative to ordinary ice, sea ice has a highly complex internal structure. A large part of this complexity is due to the way that sea ice accommodates brine as a liquid phase. Because of this added complexity, sea ice is poorly understood relative to ordinary ice. To study sea ice, because NaCl is the primary component of salt in sea brine, it is reasonable to first study ice grown from a solution of NaCl brine and then extend that experience base to sea ice.

To gain insight into the differences between saline (NaCl) ice and non-saline ice crystals, quasi-single crystals[1] of saline and non-saline ice were grown from non-saline seed crystals (Kawamura 1986). When these quasi-single crystals were loaded in compression under a constant strain rate, the non-saline crystals displayed a distinct peak stress and then "softened" or displayed decreasing resistance to deformation until eventually approaching a "steady state" stress. To the contrary, the saline crystals often, but not always, lacked the peak stress response displayed by the non-saline crystals. An example of these differences is displayed in Figure 1.

Saline ice crystals typically are conceptualized as a bridged matrix of non-saline ice platelets with a regularly spaced system of brine cavities and possibly air bubbles interspersed throughout. With this conceptual model, one would expect saline ice to display a response similar to that of non-saline ice, though with somewhat lower

[1] A *single crystal* may be defined as a specimen that grows solely from one nucleus, so that no part of the specimen is greater than 5 degrees from the mean crystallographic orientation (Winegard 1964, Ch. XII). Using the method developed by Kawamura (1986), a quasi-single is grown from as many as four sintered nuclei or plates with the same orientation. Though we would expect the resulting specimen to behave structurally as a single crystal, it does not meet the definition of a single crystal; therefore, specimens grown by this technique are referred to as *quasi-single crystals*.

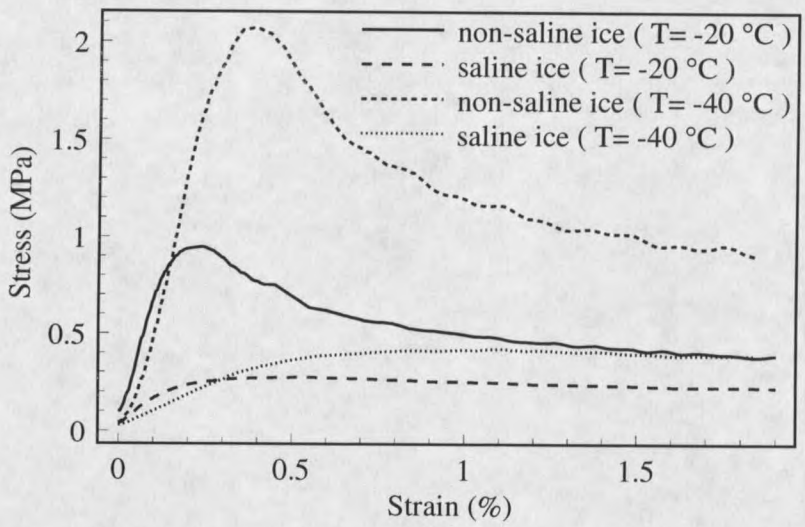

Figure 1. Stress response for constant strain rate ($\dot{\varepsilon} = 1 \times 10^{-6}$ s^{-1})

macroscopic stresses; indeed there are such cases. For an example of such an analogous behavior between saline and non-saline ice, consider the experimental results of Brown & Kawamura (1991).

Typical models for the strength of sea ice (Anderson 1958, Assur 1958, Weeks & Assur 1967, Michel 1978, Weeks & Ackley 1982) connect the reduction in strength of sea ice relative to non-saline ice using a function of brine content with models of the form

$$\sigma^S = c\sigma^N(1 - f(\psi)), \tag{1.2}$$

where σ^S and σ^N are the strength of saline ice and non-saline ice, respectively. ψ is a measure of brine content or porosity of the sea ice and c is a reduction coefficient and is commonly used to include stress concentration factors or other structural characteristics. These models, which use porosity (geometric reduction) to explain the reduced strength of saline ice, indicate that the responses of saline ice and non-saline ice should differ only by a scale factor. As a consequence, these models do not explain the absence of a peaked stress response in saline crystals when such a response is lacking; however, as displayed in Figure 1, it is clear that there are cases

where saline ice does not display the peaked stress response or large yield drops that the non-saline ice does such that the initial response differs by more than a porosity scale factor. In this dissertation, the transformation of encapsulated brine to ice will be considered as a means for the alteration of the internal structure of ice such that saline crystals will not display the peaked stress response when subjected to mechanical loads. Saline crystals that have been altered in such a manner are likely to provide much less resistance to deformation and will in essence be much more compliant. As a result, initial forces resulting from structure-ice interactions will be reduced significantly and the increasingly compliant ice will tend to support loads more readily without fracturing in a brittle fashion.

In Chapter 2, a set of experimental observations will be presented concerning the differences between the structural responses of saline and non-saline ice crystals. These observations include variations in the initial responses of saline crystals. Chapter 3 is used to present an analysis of phase transformations as a source of these observed variations. Chapter 4 is used to present a corresponding set of conclusions and a set of related studies that would be helpful in further understanding the mechanisms involved in the structural response of saline ice.

CHAPTER 2

EXPERIMENTAL OBSERVATIONS

This chapter details a set of experimental observations that point to the role that phase transformations may play in the initial compliance of saline ice. Other than these observations, there is very little literature that addresses this issue.

This chapter first presents the results of two experimental programs. One was conducted here at Montana State University (MSU) and the other at the Institute of Low Temperature Science (LTS) in Japan. These programs were conducted to gain insight into the behavior of single crystals of ice. Saline and non-saline ice crystal specimens were loaded with similar restraints so that differences in the structural responses could be observed. The specimens, taken from large quasi-single crystals of both ordinary and saline (NaCl) ice, were tested in compression under constant displacement (strain) rates. The specimens were tested over a range of strain-rates, temperatures, and with varied crystallographic orientations.

The test program initiated here at Montana State University encountered technical difficulties and has not yet been completed; however, the data that was gathered will be reviewed. Similar, tests were run at the Institute of Low Temperature Science by Brown & Kawamura (1991). To provide a more complete overview, a subset of these LTS results will also be reviewed.

MSU Test Program

This section presents a review of the partially completed MSU test program for the structural behavior of saline and non-saline crystals of ice.

Specimen Preparation

To test monocrystal specimens of ice, it is necessary to first grow large crystals from which the specimens can be formed. To grow single crystals of ice in relatively large quantities, it is convenient to first grow a large single crystal of ordinary ice that can be sliced into sections that will serve as a seed for an array of saline and non-saline single crystals of ice. These seed crystals are usually obtained by freezing still water in a large insulated tank. Care must be taken to minimize the number of sites for ice crystal nucleation. To minimize the number of foreign particles that could serve as nuclei, degassed (boiled) and filtered distilled water is used. The water is cooled in a completely filled airtight container to a temperature between 2 and 3 °C. The cooled water is then poured into an insulated tank, that has been prewarmed to prevent ice from nucleating on the sides, and allowed to continue cooling in a quiescent state until an initial ice skim has formed. After an initial skim is established, the size of the crystals forming the skim is evaluated. If there are no crystals of sufficient size the process is repeated.

Once a large single crystal is established, the crystal is allowed to grow until bubbles begin to nucleate below the surface of the ice. This typically occurs after the ice has grown to a thickness of approximately ten centimeters. The orientation of the crystal is then evaluated using an etching technique (Higuchi & Muguruma 1958, Higuchi 1958). Crystals that display a vertical c-axis[2] are suitable as seed crystals, others are discarded. Because ice crystals with a horizontal c-axis have a marked tendency to dominate during growth, particularly in sea ice, it is preferable to construct a seed crystal with horizontal c-axis. Following the technique of Kawamura

[2]Ordinary ice has a hexagonal crystalline structure. Based on this crystalline structure, a *c-axis* (also known as the optic axis) is defined parallel to the axis of hexagonal lattice-symmetry. A *basal plane* is then defined as a plane that is perpendicular to the c-axis. Three a-axes (a_1, a_2, a_3) are then defined in the basal plane such that each axis is separated by 120° and is parallel a sector boundary of the hexagon corresponding to the crystalline structure (Hobbs 1974).

(1986), the original crystal is sliced into thin planar sections (~1 cm thick) perpendicular to one of the a-axes. These plates are then rotated 90° so that the c-axes of each plate are aligned. The aligned plates are then sintered back together to form a plate approximately 25 cm square. The resulting quasi-single crystals are then used as "seeds" to grow both saline and non-saline quasi-single ice crystals. Due to the orientation of the seed crystal, the corresponding quasi-single crystals grows with a horizontal c-axis and a vertical a-axis.

To clarify the use of the term quasi-single crystal, it is worthwhile to consider the definition of a single crystal. A *single crystal* may be defined as a specimen that grows solely from one nucleus, so that no part of the specimen is greater than 5 degrees from the mean orientation (Winegard, 1964, Ch.XII). Using Kawamura's (1986) method, when the rotated plates from the original crystal are sintered together, often there is a fine line of small, randomly oriented crystals that develop at the interface between plates. These lines will sometimes extend into a specimen grown from the seed. If carefully applied, this approach yields specimens with crystal orientations within 3 degrees of the mean, except for small (< 1 mm) crystals on the interface planes. The specimens are often seeded from as many as four or five nuclei (plates). Though the resulting specimen would be expected to behave structurally as a single crystal, it does not meet the definition of a single crystal; therefore, specimens grown by this technique are referred to as *quasi-single crystals*.

After using the previous method to establish an array of seed crystals, large quasi-single non-saline ice crystals were grown from distilled and degassed water. As a result, the test specimens had a very low bubble content and most were completely bubble free.

From the same array of seed crystals, large quasi-single crystals of saline ice were grown from a brine solution of distilled water and table salt (NaCl) that had

a salinity of 0.0035 at a slow and reasonably controlled rate of approximately 1 cm per day. The slow rate was maintained to minimize the nucleation of bubbles. Once the crystals grew to a depth exceeding 20 cm, they were removed from the growth tank and the saline crystals were allowed to drain for more than a week. The saline crystals were drained for an extended period of time so that they would have approximately the same "drained" brine content at the time of testing. After draining, the crystals were cut into sheets perpendicular to the growth direction. Thin sheets, approximately 1 cm thick were taken from the top, middle, and bottom of the crystal. These thin sheets were used to evaluate crystal quality throughout the presumed quasi-single crystal, using cross polarized light to determine the existence of large spurious inclusions. The remaining thicker sheets were cut into specimens 5 centimeters square and 22 centimeters long where the c-axis was oriented at 45 degrees relative to the long axis of the specimen (see Figure 2). Spurious inclusions were avoided if at all possible, though small ($\sim$1 cm diameter) inclusions remained in the end sections of a small subset of the specimens.

After the lab specimens were trimmed to the prescribed dimensions (5 cm $\times$ 5 cm $\times$ 22 cm $\pm$ 2 mm), the ends were squared and flattened to provide an accurate match with the load platens. However, some of the specimens still demonstrated initial load responses indicative of an imperfect match.

Test Program

As displayed in Figure 2, all specimens tested at Montana State University were oriented with the c-axis at a 45° angle to the long axis of the specimen with an a-axis exiting one of the lateral surfaces at a 90° angle. All specimens were compressed under a constant displacement rate that correlated with a constant strain rate of 10^{-6} s^{-1}. During each test, the temperature was held constant ($\pm 0.5\,^{\circ}C$). Test temperatures

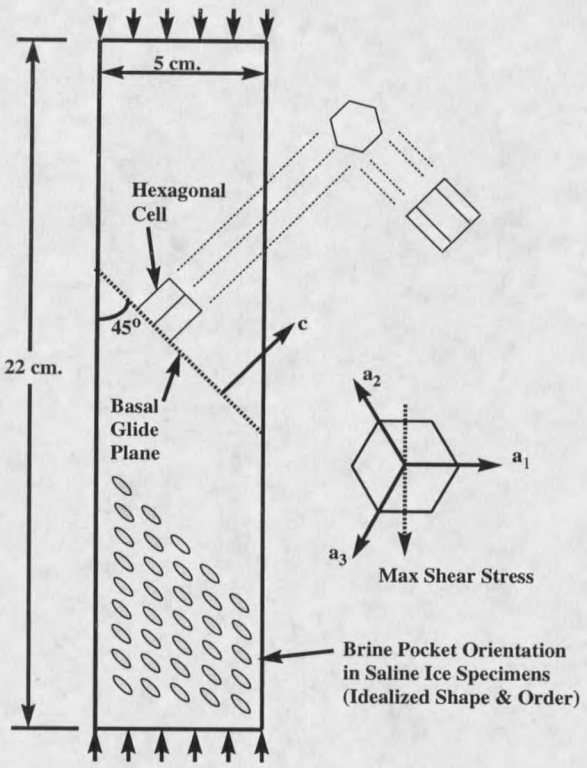

(a) Sketch of Experimental Specimen

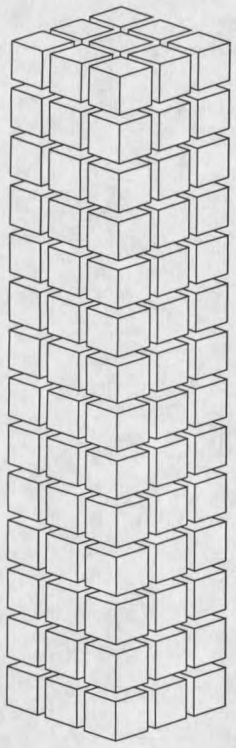

(b) Specimen Geometry

Figure 2. Geometry of experimental test specimens

were varied from -10 to $-45\,^{\circ}\mathrm{C}$.

Test Results

The saline ice crystals had bulk salinities that were grouped around 0.006, though they ranged from 0.0045 to 0.0075; two specimens had salinities outside this range. The densities for the saline and non-saline specimens were closely grouped around 913 and 916 kg m^{-3}, respectively, as measured at a temperature of $-10\,^{\circ}\mathrm{C}$. The range of salinities and densities presumably reflect variations in specimens taken from different vertical ranges of the original crystals. Overall, approximately 40 quasi-single crystal specimens were tested. Typically, two non-saline and three saline specimens were tested at each temperature.

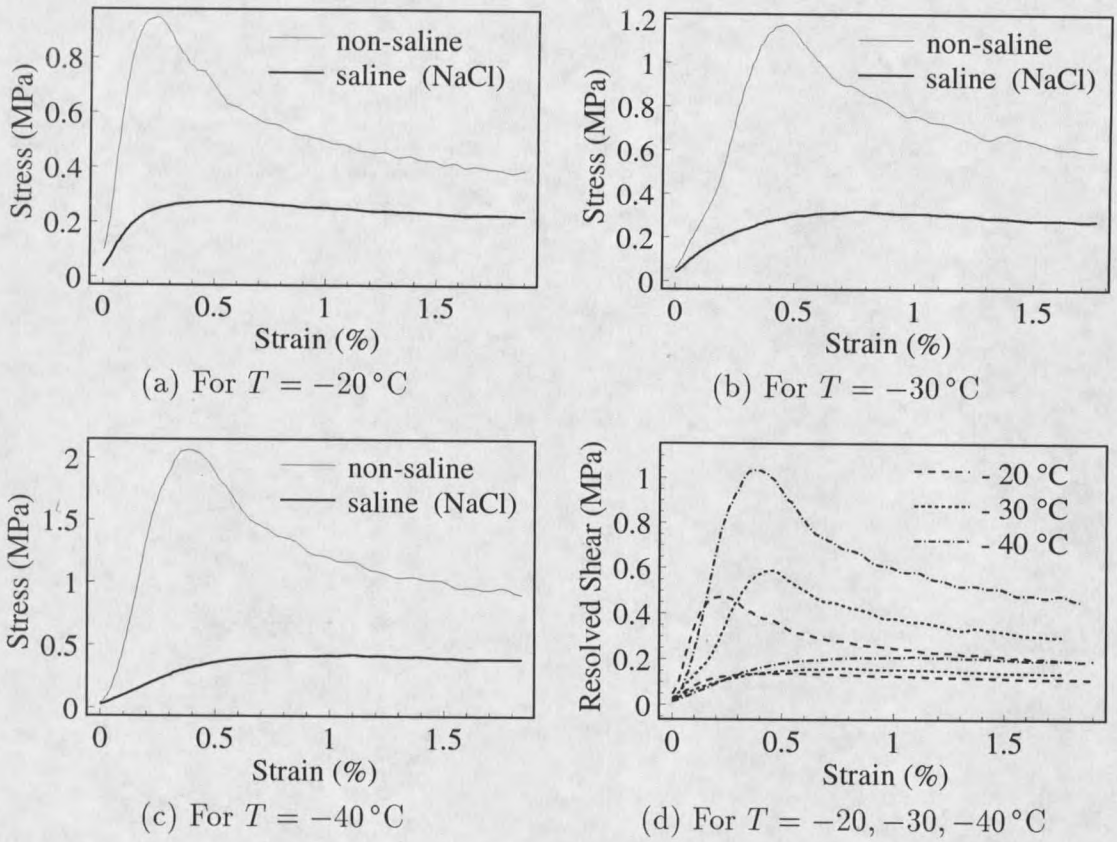

Figure 3. Stress response comparison for saline and non-saline ice crystals. Each curve represents the averaged response of two specimens under a constant strain rate ($\dot{\varepsilon} = 10^{-6}\ \mathrm{s}^{-1}$). The averaged data was smoothed using a least squares technique (Savitzky & Golay 1964) with a smoothing interval of 0.05% strain. (d) provides a comparison of responses in (a), (b), and (c) in terms of the shear stress resolved on the basal plane.

Figure 3 displays the averaged responses of saline and non-saline monocrystalline specimens tested at $-20, -30$, and $-40\,^{\circ}\mathrm{C}$. The averaged data was smoothed using a least squares technique (Savitzky & Golay 1964) with a smoothing interval of 0.05% strain.

In particular, notice that though both the saline and non-saline were grown from the same seeds and by the same technique, the non-saline ice displays a peaked response while the responses displayed by the saline ice crystals demonstrates almost

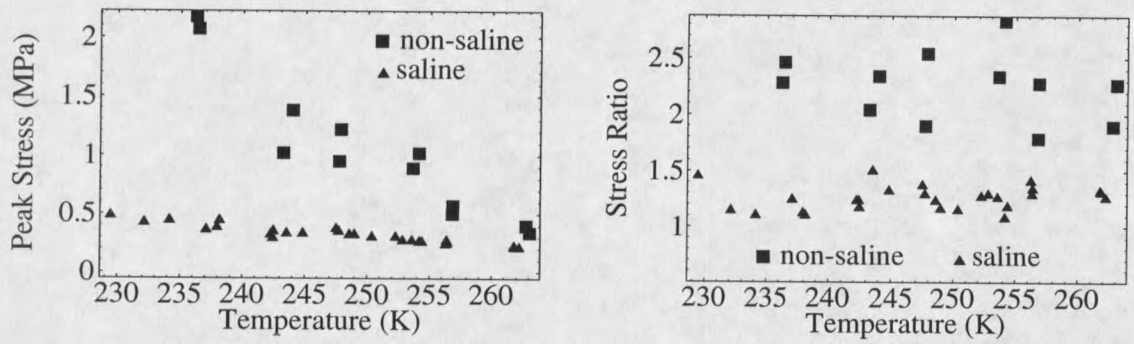

(a) Peak stresses

(b) Stress Ratio

Figure 4. Peak Stress Comparison. (a) provides a comparison between peak stresses displayed by saline and non-saline quasi-single ice crystals. (b) displays the ratio of the peak stress to the stress at 2% strain.

no peak at all.

The peak stress for each specimen tested at MSU is displayed as a function of temperature in Figure 4a. A rather surprising difference between specimen behavior is displayed in Figure 4a. In particular, the peak stress displayed by the non-saline specimens is much more temperature dependent than the peak stresses displayed by the saline specimens. Based on a linear fit to the data, the peak stress of the non-saline specimens displays a sensitivity of -65 KPa $^{\circ}C^{-1}$, compared to -7.7 KPa $^{\circ}C^{-1}$ for the saline specimens. Also notice the consistency with which the peak stress of the saline specimens increases with decreasing temperature while the non-saline specimens display a similar trend but in a more sporadic fashion. To further illustrate the difference in the responses of the saline ice specimens and the non-saline ice specimens, the peak stress has been divided by the corresponding stress at 2% strain and displayed as a ratio in Figure 4b. Though these "2% stresses" cannot be considered steady flow stresses,[3] they serve as a characteristic values that can be used to provide

[3]A few specimens were run to strains on the order of 4%. Stresses were observed to approach a steady value at strains near 3%.

a measure of the stress drop. Notice that in terms of these stress ratios (Figure 4b), the saline specimens display values on the order of 1.25 while the non-saline specimens typically display values greater than 2. Such a significant difference in the stress ratio indicates that there are significant differences in the internal crystal structure of the two forms of ice.

LTS Test Program

This section presents review of the LTS test program for the structural behavior of saline and non-saline crystals of ice.

Specimen Preparation

The technique used for specimen preparation at LTS was essentially the same as that used at MSU. Actually many of the techniques used at MSU were derived from the LTS program. The significant differences in the manner of specimen preparation were tied to specimen length and orientation. In particular, the long dimension of the LTS specimens was 20 cm rather than 22 cm. For orientational differences, the c-axis was oriented relative to the long axis of the LTS specimens at angles of $45, 60, 66$, and $90°$ rather than the $45°$ angle used for the MSU specimens.

Test Program

As with the MSU specimens, the LTS specimens were also loaded in compression at a constant displacement rate; however, the displacement rate varied from one set of specimens to the next. The cross-head rate of the test machine was limited to a minimum rate of 0.5 mm min^{-1} so that the minimum strain rates attainable were approximately 4×10^{-5} s^{-1}. Though displacement rates varied, test temperatures were held constant at $-11\,°\text{C}$ for all specimens.

Test Results

The saline ice crystals had bulk salinities that ranged from 0.007 to 0.009. The densities for both the saline and non-saline specimens ranged from 905 to 917 kg m^{-3} with a median at 912 kg m^{-3} , as measured at a temperature of $-10\,^{\circ}C$. Overall, 17 quasi-single crystal specimens were tested (five non-saline specimens and twelve saline specimens).

The data from the LTS program provides a record of variations in the stress response of saline ice under a wide range of load conditions. Unfortunately, the data sets are not large enough to accurately quantify the range of variations that occur under each set of load conditions.

To study the variations in the stress response of saline ice crystals due variations in crystal orientation, a set of specimens was deformed at a constant strain rate of approximately 4×10^{-5} s^{-1}. Two specimens were deformed with the c-axis initially oriented at a 45° angle to the load direction and two additional specimens were deformed with the c-axis initially oriented at a 66° angle to the load direction. The averaged responses are displayed in Figure 5. Notice that, contrary to the MSU saline specimens (Figure 3), these saline specimens display a peaked stress response.

As strains approached 10% for the 45° and 66° specimens (Figure 5), Brown & Kawamura (1991) observed the development of slip bands parallel to the basal plane. Assuming deformation for both orientations dominated by basal slip, the responses for both orientations (45° and 66°) are plotted in terms of the shear stress resolved on the basal plane. Notice, as displayed in Figure 5, that the resolved shear stress responses are in relatively close agreement indicating that even at the 66° orientation that deformation is dominated by slip or shear on the basal plane. Due to the small size of the data sets, it is not clear whether the small difference in the resolved responses is due to statistical variations or whether there may be an additional mechanism that

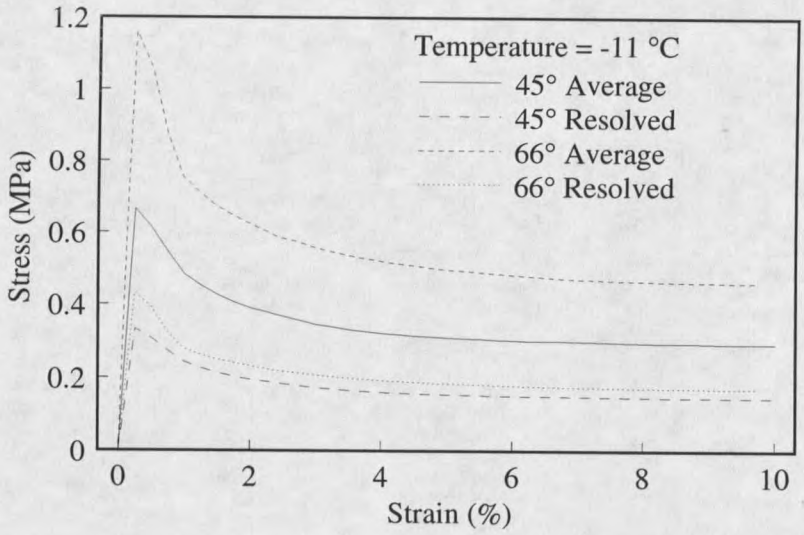

Figure 5. Variations in the stress response of saline ice crystals at a constant strain rate ($\dot{\varepsilon} \approx 4 \times 10^{-5}$ s^{-1}) due to basal plane orientation (45° and 66°). The average 45° and 66° curves represent the axial stress responses of three and four specimens, respectively; the curves were smoothed by an unknown technique. The resolved curves represent the averaged responses in terms of the shear stress resolved on the basal plane, using the Schmid factor [adapted from (Brown & Kawamura 1991, Fig. 3)].

somewhat limits basal plane slip at the 66° orientation. It is likely that there is a geometrical effect due to the manner in which brine cells align themselves with the basal plane (Weeks & Ackley 1982).

For additional data on orientational dependencies, a second set of specimens was deformed at a constant strain rate of approximately 6.3×10^{-5} s^{-1}. Two of these specimens were deformed with the c-axis initially oriented at a 60° angle to the load direction and two additional specimens were deformed at a 90° angle. The averaged responses are displayed in Figure 6. The stress responses for these specimens were not expressed in terms of the resolved shear stress on the basal plane as the resolved shear stress for the 90° orientation is zero. Notice that the stress response for the 90° orientation varies significantly from the response for the 60° orientation. In particular, the averaged initial stress response for the 90° specimens is significantly higher

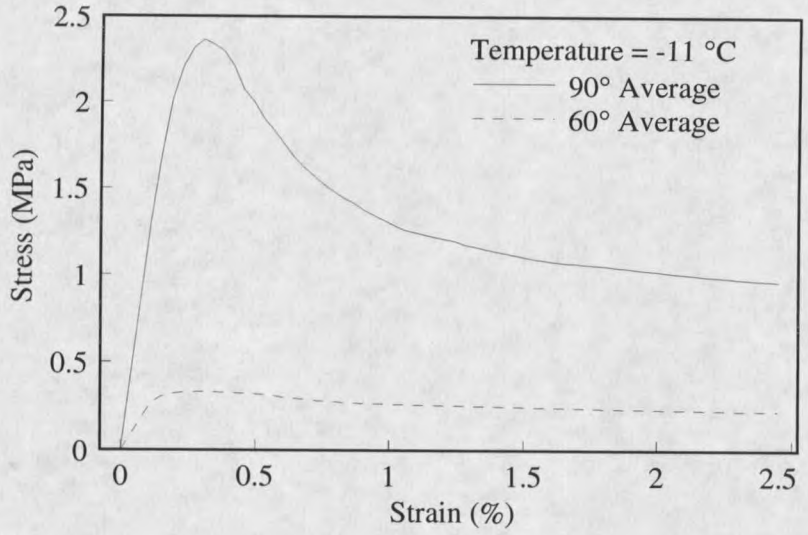

Figure 6. Variations in the stress response of saline ice crystals with the c-axis oriented at 60° and 90° to the load direction at a constant strain rate ($\dot{\varepsilon} \approx 6.3 \times 10^{-5}$ s^{-1}). The average 60° and 90° curves each represent the axial stress responses of two specimens; the curves were smoothed by an unknown technique [adapted from (Brown & Kawamura 1991, Fig. 5)].

than the averaged response for the 60° specimens. This difference is most likely due to a combination of geometric factors. First, because the basal plane is oriented at a 90° angle to the load direction, slip or shear on the basal plane is not active. Corresponding to similar observations for ordinary ice (Higashi 1966), Figure 6 indicates that the non-basal components of slip are much more resistant to deformation that are the basal components of slip. Also, the anisotropic alignment of brine cells in arrays that lie parallel to the basal plane is likely to enhance the difference between basal plane shear deformation and non-basal deformation (Weeks & Ackley 1982). In essence, the initial response is in agreement with observations of the structural nature of non-saline ice. However, the somewhat surprising characteristic of the 90° response is the display of strain softening after the initial stress peak. The non-basal response ordinary ice displays a strain hardening character (Higashi 1966, Fig. 4). Based on

the observations of Brown & Kawamura (1991, Fig. 6), the strain softening characteristic displayed by the 90° specimens is most likely due to a geometric instability resulting from brine channels. In both specimens, Brown and Kawamura observed localized bulges near pre-existing brine drainage channels in the specimens. Volumetric measurements of the bulges indicated that as much as 30% of the deformation could be accounted for in the mass of the bulges. Though both specimens tested by Brown & Kawamura (1991, Fig. 7) displayed remarkably similar responses, this mode of deformation is likely to be extremely scale dependent due to the inhomogeneous nature of brine channels at scales on the order of centimeters. At scales on the order of meters, the distribution of brine channels can be treated as homogeneous (Lake & Lewis 1970). As a result, the role they play as deformation mechanisms at larger scales is likely to be significantly different than the role they play in specimens of the size used in this test program.

All of the comparisons for saline ice crystals considered thus far from the LTS program have been based on orientational variations. To extend the range of variables, Figure 7 displays a comparison of the 60° and 66° responses displayed in Figure 6 and 5, respectively. Notice that the 60° and 66° specimens were deformed under a constant strain rates of approximately 6.3×10^{-5} and 4×10^{-5} s^{-1}, respectively. The specimens tested at the higher strain rate display a significantly elevated stress response. The stress responses are also displayed in terms of the shear stress resolved on the basal plane to minimize differences due to orientational effects.

To compare the behavior of saline ice to non-saline ice, Brown & Kawamura (1991) tested three non-saline quasi-single crystal ice specimens with the c-axis oriented at 60° to the load axis under a constant strain rate ($\dot{\varepsilon} \approx 6.3 \times 10^{-5}$ s^{-1}). Of these three, the first two fractured and broke shortly after reaching peak stresses of 1.7 and 2.2 MPa. The response of the unfractured specimen is displayed in Figure 8 along

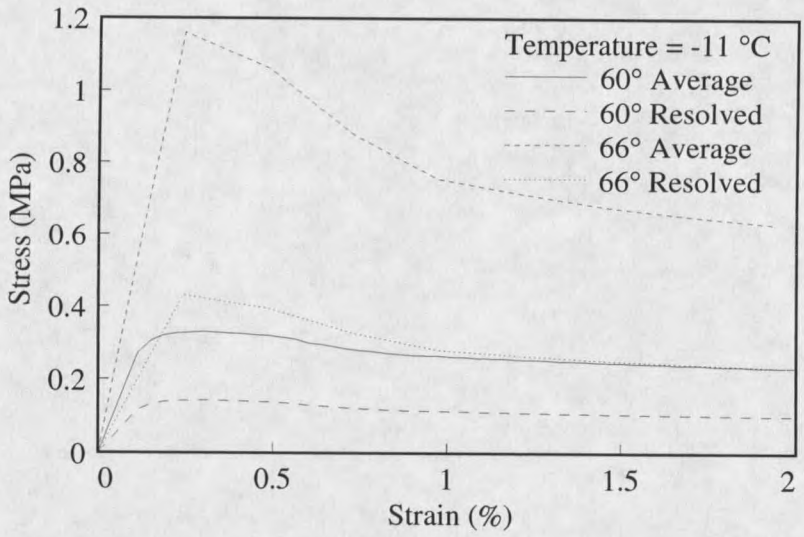

Figure 7. Strain-rate dependence of the stress response for saline ice crystals. The 60° and 66° specimens were deformed under a constant strain rates of approximately 6.3×10^{-5} and 4×10^{-5} s^{-1}, respectively. The average 60° and 66° curves represent the axial stress responses of two and four specimens, respectively; the curves were smoothed by an unknown technique. The resolved curves represent the averaged responses in terms of the shear stress resolved on the basal plane, using the Schmid factor [adapted from (Brown & Kawamura 1991, Fig. 2&4)].

with the corresponding averaged response of two saline specimens. Notice that the comparison bears a striking similarity to the responses from the MSU test program.

In the following chapter, the primary focus will be on variations in the stress response that might be due to phase transformations that occur in saline ice crystals at temperatures above the eutectic temperature ($-21.2\,°C$).[4] In light of this possibility, consider the following variation in stress responses.

On the subject of stress variations, the averaged 60° response displayed in Figure 6 is the average of the two responses displayed in Figure 9. Of particular interest is the lack of a peaked stress response for Test #13. The response displayed by this specimen is remarkably similar to the responses displayed by specimens in

[4]The *eutectic temperature* is the temperature at which brine "freezes" into a eutectic (mixed) phase. For NaCl brine the eutectic phase is $NaCl{\cdot}2H_2O$.

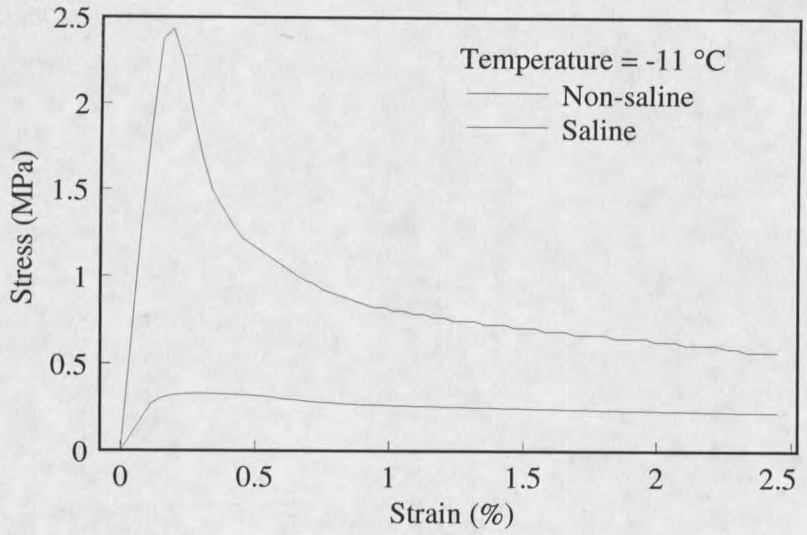

Figure 8. Variations with between responses of saline and non-saline crystals with the c-axis oriented at 60° to the load direction at a constant strain rate ($\dot{\varepsilon} \approx 6.3 \times 10^{-5}$ s^{-1}). The non-saline and saline curves represent the axial stress responses of one and two specimens, respectively; the curves were smoothed by an unknown technique [adapted from (Brown & Kawamura 1991, Fig. 9)].

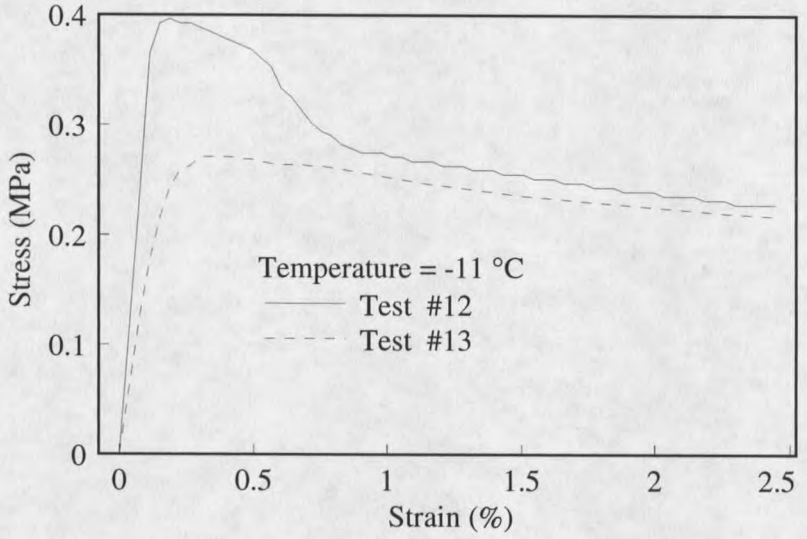

Figure 9. Stress response variations in saline crystals under non-varying load conditions with the c-axis oriented at 60° to the load direction at a constant strain rate ($\dot{\varepsilon} \approx 6.3 \times 10^{-5}$ s^{-1}). The data was smoothed by an unknown technique [adapted from (Brown & Kawamura 1991, Fig. 4)].

the MSU test program; all other specimens tested in the LTS program display some form of a peaked stress response. Because the quasi-single ice crystal specimens used in both test programs (MSU and LTS) were grown by the same technique, it is reasonable to expect that the responses should be quite similar. Saline crystals tested in both programs would be expected to consistently display peaked stress responses or otherwise the lack of peaked stress responses. That two specimens with such a similar background (Test #12 and #13) can display such different initial responses indicates that very minor differences in a saline crystals history can lead to large variations in the crystals initial resistance to deformation.

Non-saline ice responses

In the two test programs discussed previously, non-peaked stress responses were observed only for the saline crystals. However, as illustrated in Figure 10, Higashi, Koinuma & Mae (1964) have recorded similar non peaked stress responses for non-saline specimens. But these non-peaked stress responses were observed only for pre-strained specimens.

If we view the peak stress in terms of dislocation theory[5] then, in essence, we can view these peaks as the response of a crystalline structure with a low initial dislocation density. Once dislocations begin to move, multiplication mechanisms will act to rapidly increase the mobile dislocation density, providing a more responsive network of mobile dislocations. Figure 10 provides evidence that such a view point is reasonable. As displayed, if a crystal is loaded and then abruptly unloaded, the stress response returns to follow the same general softening trend that was abruptly

[5] *Dislocation theory* is based on the concept that permanent deformation occurs through the movement of internal "linear" imperfections in the crystalline structure known as dislocations (Hirth & Lothe 1982). As these imperfections move, they often tend to multiply, increasing the density of dislocations in the crystal. With an increased dislocation density, inelastic deformation can occur more readily. For an introduction to dislocation theory, consider Hull & Bacon (1984).

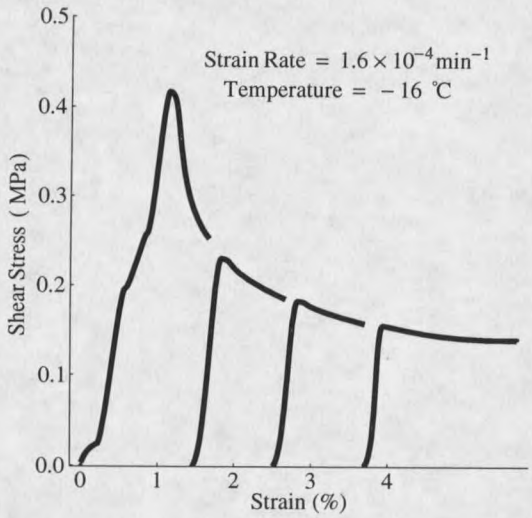

Figure 10. Stress response for basal slip in single crystals under a constant strain rate [after (Higashi et al. 1964, Fig. 4)].

truncated. Such behavior indicates that the primary changes in the stress response are due to deformation induced changes in the crystalline structure (i.e., an increase in the mobile dislocation density). As a result, the magnitude of the original stress peak is highly dependent on the previous deformation history or, more accurately, on the mobile dislocation density.[6]

One relatively distinctive characteristic of basal plane deformation in monocrystalline ice is its propensity to strain soften rather that strain harden. This tendency seems to be driven by the manner in which the primary slip system dominates as an inelastic deformation mode. In many crystalline materials, particularly those with cubic lattice structures, slip is simultaneously active on intersecting planes. As the dislocation density increases on each of these intersecting planes, the interactions between dislocations on different slip planes increase in a manner that serves to immobilize or annihilate dislocations, effectively decreasing the mobile dislocation

[6]To understand the hypothesis of this dissertation, it is not necessary to understand dislocation theory. However, it is important to understand that as the crystal structure is altered through permanent deformation, the crystal's resistance to deformation changes.

density. In monocrystalline ice, when the primary system is allowed to dominate, such interactions are minimized and the mobile dislocation density is allowed to approach a stationary (steady-state) value in an asymptotic fashion.

Thermal Variations

Because the specimens in the MSU and LTS test programs were not knowingly pre-strained, other mechanisms had to be considered for the lack of a peaked stress response in the saline crystals. Though the rate of crystal growth was maintained at a rather slow rate in both test programs, growth and storage conditions were not otherwise monitored very closely. After observing the variations in the responses of the saline crystals, the general growth and storage conditions were reviewed with the hope of gaining insight into the observed variations in the saline crystal responses.

The LTS quasi-single crystals of saline ice were subjected to very little thermal cycling. Upon removal from the crystal growth bath, the LTS specimens were stored at $-11\,^{\circ}\mathrm{C}$, both during the period they were allowed to drain and after they were cut into specimens. During the entire period, the temperature variations were probably no more than $\pm 0.1\,^{\circ}\mathrm{C}$ as the specimens were placed in insulated boxes that were stored inside a cold room that had temperature control to within $\pm 1\,^{\circ}\mathrm{C}$. Prior to testing, each specimen was slowly cooled to the test temperature.

The MSU tests followed a similar procedure, but the cold room had a larger temperature oscillation and the test specimens were subjected to a very low thermal cycling between $-10\,^{\circ}\mathrm{C}$ and $-20\,^{\circ}\mathrm{C}$ while they were stored. This cycling occurred when the cold room temperature was slowly lowered over the period of approximately one month in order to grow new saline quasi-single crystals.

Relative to these temperature histories, the MSU saline crystal specimens, which were subjected to much more thermal cycling, displayed a consistent lack of

peaked stress responses. The LTS saline crystal specimens, which were subjected to very little thermal cycling (predominantly during growth), displayed significant variations in peaked stress responses. Because of these differences, it seems reasonable to consider the role that thermal cycling might play in the reduction or absence of a peaked stress response.

In a review of the literature, only two papers were found that addressed possible mechanisms for variations in the initial compliance of saline ice. Both Knight (1962) and Bennington (1963) observed strain figures in the neighborhood of brine cells in ice that indicated that the ice had been strained locally. Both of these authors assumed that the strain figures resulted from thermally-driven mechanisms. Knight (1962) further observed low angle grain boundaries that presumably resulted from the migration of dislocations generated by the localized straining. However, the significance of these observations was not quantified in any fashion. The first attempts at quantifying this mechanism were presented by (McKittrick & Brown 1993) and (Gupta, Picu & Frost 1993)[7]; however, both of these presentations appear to contain significant errors.

In the following chapters, thermal cycling will be addressed, from a mathematical point of view, as a factor in the structural response of saline ice. In particular, cyclic phase transformations of encapsulated brine will be considered as a possible mechanism for the pre-deformation of saline crystals before they are ever subjected to external mechanical loads.

[7](Gupta et al. 1993) explored such thermally driven mechanisms as a means for crack nucleation.

CHAPTER 3

PHASE TRANSFORMATION MECHANISM

This chapter addresses phase transformations as a factor in the behavior of saline ice, as these transformations seem likely to induce deformation in the saline ice crystal due to cooling during growth or storage. If this is the case, then any mechanical testing performed on test specimens is actually done on specimens which have been pre-deformed in the neighborhood of the brine cells. If this mechanism induces stress sufficient to produce local deformation well into the plastic regime then, in the case of ice monocrystals, softening will effectively occur without the necessity of external loads.

Ice crystallization from brine

As crystals of ice form in a brine solution, nearly all of the solute (salt, air, etc.) remains in solution Weeks & Ackley (1982, pg. 4). As the crystals grow into the melt they form a series of parallel blade-like platelets, which are on the order of 0.5 mm thick. As growth proceeds, observers (Anderson & Weeks 1958, Weeks & Ackley 1982, Grenfell 1983) report that the platelets thicken and bridges begin to form approximately 2.5 cm above the lower tip of the platelets. The bridging process between platelets develops around vertical columns of brine which might extend vertically through the entire crystal. As the ice cools further, the columns of brine collapse into arrays of nearly spherical brine cells. As the brine cells age, they have an increased tendency to take on an ellipsoidal geometry.

Utilizing this outline of crystal development, assume that the ice crystal and trapped brine are stress-free immediately after the brine columns collapse into arrays of nearly spherical brine cells. Then the driving question becomes, what happens as the ice and brine are cooled further?

The next task is to consider the transformation of encapsulated brine as the crystal temperature drops either during the growth stage or while in storage.

Phase changes

To quantify the composition of the brine phase, define the salinity of the brine (s^B) by the non-dimensional form

$$s^B = \frac{m^S}{m^B} = \frac{mass\ of\ salt}{mass\ of\ brine} \tag{3.1}$$

To understand the relationship between the phases of brine and ice, consider the phase diagram cartoon (Figure 11), from Weeks & Ackley (1982). For a brine solution with a salinity of 0.035, when the temperature drops to $-2\,^\circ$C water precipitates out of the brine in the form of ice. If the brine is contained in a small closed system, then the transformation from water to ice implies that the mass of brine decreases significantly while the mass of salt in solution remains "constant"[7]; thus the salinity of the brine increases. The increase in brine salinity requires a further decrease in temperature before more ice can precipitate out. This process will continue until the brine reaches the eutectic point, at a salinity of 0.233 and a corresponding temperature of $-21.2\,^\circ$C. Before the temperature of the brine can drop below the eutectic point, the brine solution must assume the solid form of sodium chloride dihydrate ($NaCl{\cdot}2H_2O$).

As modeled by the Gibbs phase rule (Weeks & Ackley 1982), the phase equilibrium and hence conditions for phase transformations are dependent on changes in

[7]A very small amount of salt (~0.01%) enters the ice phase (Harrison & Tiller 1963).

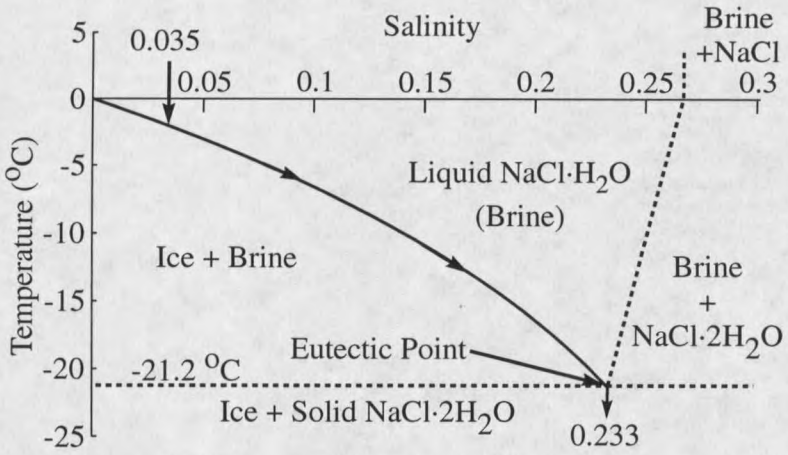

Figure 11. Phase Diagram for $H_2O$and NaCl

pressure and temperature. As pressure increases the phase curve typically depresses. As a first approximation, it is reasonable to assume that the phase equilibrium curve is independent of pressure. Cox & Weeks (1975, Tab. I) use the following third order polynomial to model the phase relationship between the brine salinity (s^B) and the freezing/melting temperature (T):

$$s^B = \left(-17.573\,T - 0.381246\,T^2 - 3.28336 \times 10^{-3}\,T^3\right) \times 10^{-3} \tag{3.2}$$

where the transformation temperature (T) is in degrees Celsius. Their equation is based on a statistical fit of experimental data with a correlation coefficient of 0.999927 and a standard error equal to 0.4334×10^{-3}.

Phase densities

For brine density, assume that pressure and temperature are independent variables and that temperature and salinity are directly correlated. For the stress-free density of brine (ρ^B), the approximation for sea brine given by Cox & Weeks (1983, Eq. 16) is

$$\rho^B = \rho^W \left(1 + \frac{s^B}{\zeta^B}\right), \tag{3.3}$$

where

$$\zeta^B = 1.25 \tag{3.4}$$

and ρ^W is the density of water at 0 °C. For the density of non-saline ice (ρ^I), the approximation given by Pounder (1965, Eq. 29) is

$$\rho^I = \rho_o^I \, (1 - 1.53 \times 10^{-4} T), \tag{3.5}$$

where the temperature T is in degrees Celsius and ρ_o^I represents the density of ice at 0 °C with the value:

$$\rho_o^I = 916.8 \text{ Kg m}^{-3}. \tag{3.6}$$

When the temperature of the brine drops below the eutectic point and the brine takes on the solid form of sodium chloride dihydrate ($NaCl{\cdot}2H_2O$), the density of the solid is approximately 1630 Kg m^{-3} Weeks & Ackley (1982, Tab. I). A comparison of the density of this eutectic phase with the density of brine (3.3) at the eutectic point ($\rho_e^B = 1186$ Kg m^{-3}) implies that the brine contracts as it transforms into solid form. Given the nature of the present query (i.e, expansion induced deformation), there is no need to consider temperatures below the eutectic point.

Volumetric Strain (due to Phase Transformations)

This section addresses the stress-free variations in the volume of the components contained in a brine cell due solely to phase transformations. To quantify the changes, suppose that there is an imaginary boundary around an arbitrary brine cell when it is first sealed or completely surrounded by ice but is yet stress-free. Then consider the changes in component volumes (brine and ice), assuming components are allowed to overlap. This imaginary process is illustrated in Figure 12.

This model of a brine cell consists three distinct structural components. First is the ice external to the brine cell. Second is the brine trapped in the brine cell. The

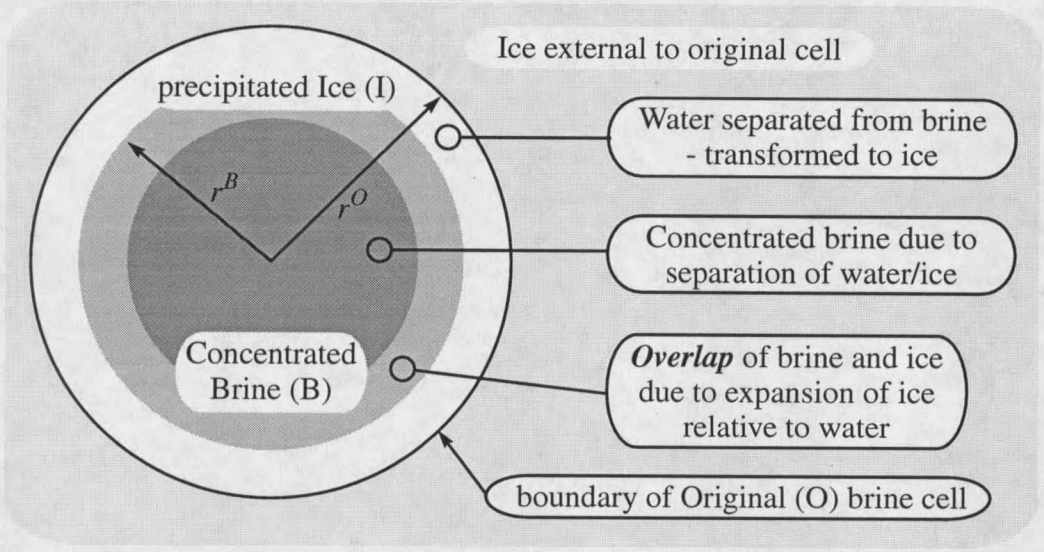

Figure 12. Conceptual (spherical) model for a brine transformations

third component is the ice that precipitates out of the brine to form an icy shell on the inside of the original brine cell. This precipitation continues as the temperature of the brine cell is drops. Given the lower density of ice, as ice precipitates out, the total system must expand.

This section addresses only the volume changes resulting from the two components on the interior of the original brine cell. Though Figure 12 illustrates polar or spherical geometry, the volume changes modeled in this section are independent of geometry.

Notation

For state variables, m represents mass, s represents salinity, ρ represents density, and V represents volume. For the components, the superscripts S, B, I, and W designate salt, brine, precipitated ice, and non-saline water, respectively. Superscript O will identify combined components of the "Original" brine system. Subscripts index the state; in particular, o denotes the initial state, T denotes variations due to the phase

transformation from brine to ice.

Brine Transformation-Volume

Because the most significant volume changes hinge on the transformation from brine to ice, it is reasonable to start by modeling the transformation volume of the brine (V_T^B).

Given the closed nature of a brine cell, the mass of salt contained in a cell remains constant. In addition, assume that all of the salt mass is retained within the brine since, upon freezing, ice rejects practically all of the salt. Based on experimental results (Harrison & Tiller 1963), this assumption is a good approximation for density calculations. Based on the preceding statements,

$$m^S = s_o^B \rho_o^B V_o^B = s^B \rho^B V_T^B. \tag{3.7}$$

If the terms are rearranged, the transformation brine volume (V_T^B) can be represented by

$$V_T^B = V_o^B \left(\frac{s_o^B \rho_o^B}{s^B \rho^B} \right). \tag{3.8}$$

Representing the brine density as a function of salinity (3.3) yields

$$\frac{V_T^B}{V_o^B} = \frac{s_o^B(\zeta^B + s_o^B)}{s^B(\zeta^B + s^B)}. \tag{3.9}$$

If $T \leq T_o$, then $\zeta^B = 1.25 > .233 \geq s^B \geq s_o^B$ implies the volume is approximately inversely proportional to the salinity and is related in a similar fashion to temperature,[8] i.e.,

$$\frac{\tilde{V}_T^B}{V_o^B} \approx \frac{s_o^B}{s^B}. \tag{3.10}$$

[8]The relative difference in these two approximations (3.9, 3.10) can be written as

$$\frac{V_T^B - \tilde{V}_T^B}{V_T^B} = \frac{s_o^B - s^B}{\zeta^B + s_o^B}$$

. If $s_o^B = 0.035$, this difference reaches a maximum of 15%, near the eutectic point.

The term $\tilde{V}_T^B$ indicates an approximation of the transformation brine volume (V_T^B); this approximation emphasizes the relationship between the brine volume and the brine salinity. In essence, as the salinity increases, there is less and less brine volume for ice to precipitate from; therefore, the most significant changes should occur immediately after a sealed brine cell begins to cool.

Differential Changes for the Total Transformation-Volume

The stress-free (transformation) volume of the brine cell (V_T^O) will be defined as the sum of the reduced brine volume (V_T^B) and the precipitated ice volume (V_T^I).

$$V_T^O = V_T^B + V_T^I = \frac{m^B}{\rho^B} + \frac{m^I}{\rho^I} \tag{3.11}$$

As indicated earlier, the superscript O denotes the original brine system. Here, after the temperature is lowered, the original system consists of the remaining brine and the ice that has precipitated out of the brine. Differentiating the preceding expression yields

$$dV_T^O = \frac{dm^B}{\rho^B} - \frac{m^B d\rho^B}{(\rho^B)^2} + \frac{dm^I}{\rho^I} - \frac{m^I d\rho^I}{(\rho^I)^2} \tag{3.12}$$

In this expression, the stress-free brine density can be written as a function of temperature or salinity. In particular, the density changes can be expressed as a function of salinity such that temperature effects are included implicitly, Equations (3.2) and (3.3); thus

$$\rho^B = \rho^W + \frac{\rho^W}{\zeta^B} s^B \tag{3.13}$$

and differentiating yields

$$d\rho^B = \frac{\rho^W}{\zeta^B} ds^B \tag{3.14}$$

Considering the differential density change for ice, all but a very small amount of salt is rejected from ice so that salinity can be neglected. Also, for temperature

changes on the order of 20 °C, density changes will be small so that the density differential may be neglected. [9]

Returning to the expression for the differential volume change (3.12), substituting for the brine density differential (3.14), recalling $V_T^B = m^B/\rho^B$, and allowing the density differential for the precipitated ice to vanish, yields

$$dV_T^O \approx \frac{dm^B}{\rho^B} + \frac{dm^I}{\rho^I} - V_T^B \frac{\rho^W ds^B}{\rho^B \zeta^B} \tag{3.15}$$

Focusing on the first two terms in the differential volume expression, the mass of the brine in the original system (m_o^B) can be written as

$$m_o^B = m^B + m^I \tag{3.16}$$

because the mass of precipitated ice in the original system is zero (i.e., $m_o^I = 0$). Differentiating the preceding mass relation yields

$$dm^I = -dm^B. \tag{3.17}$$

Substituting into the volumetric differential (3.15) and simplifying,

$$dV_T^O = -\frac{dm^B}{\rho^B}\left(\frac{\rho^B}{\rho^I} - 1\right) - V_T^B \frac{\rho^W ds^B}{\rho^B \zeta^B}. \tag{3.18}$$

To make this equation more useful, the first term can be expressed in terms of salinity rather than mass. Using the definition of brine salinity (3.1), the brine mass (m^B) can be written as:

$$m^B = \frac{m^S}{s^B} \tag{3.19}$$

[9] Differentiating Equation (3.5), setting $d\rho^I = \Delta\rho^I$ and $dT = \Delta T = -20\,°\mathrm{C}$,

$$\Delta\rho^I = \rho_0^I(-1.53 \times 10^{-4}\Delta T) \approx 0.003\rho_0^I$$

implies the density of the precipitated ice changes less than 0.3% for temperature changes less than 20 degrees Celsius.

Recalling that the salt mass (m^S) is constant, differentiating, and substituting $m^S = m^B s^B$ and $m^B = \rho^B V_T^B$, yields

$$dm^B = -\frac{m^B}{s^B} ds^B = -\frac{\rho^B V_T^B}{s^B} ds^B \tag{3.20}$$

Returning to the volumetric differential (3.18) and substituting for dm^B (3.20) yields

$$\frac{dV_T^O}{V_T^B} = \left[\left(\frac{\rho^B}{\rho^I} - 1 \right) \frac{1}{s^B} - \frac{\rho^W}{\rho^B} \frac{1}{\zeta^B} \right] ds^B. \tag{3.21}$$

Substituting for ρ^B as a function of salinity (3.3) implies

$$dV_T^O = V_T^B \left[\frac{\rho^W}{\rho^I \zeta^B} + \xi \frac{1}{s^B} - \frac{1}{s^B + \zeta^B} \right] ds^B \tag{3.22}$$

where

$$\xi = \left(\frac{\rho^W}{\rho^I} - 1 \right) \tag{3.23}$$

This differential relation gives us a measure of the increasing interference between the two phases, i.e., brine and ice.

Strain Function

Consider the use of the preceding volumetric differential (3.22) as a strain measure. The total volume differential (dV_T^O) gives us a measure of the total volume change of the original brine cell contents under stress-free conditions. If the brine volume is considered as a reference volume, then it appears as if all of the expansion is taking place in the brine. Integrating this strain measure between the initial state and the current state yields a measure of the total strain (e_T^B) relative to the brine volume,[10]

[10]In some cases it may be appropriate to define the reference volume as the sum of the brine volume and the expansion volume (volume increase due to the transformation from water to ice). This altered reference volume ($\acute{V}_T^B$) can be defined by

$$\acute{V}_T^B = V_T^O - \frac{m^I}{\rho^W} = V_T^B + \xi V_T^I$$

The strain using this definition is 20% less by the time the eutectic point is reached. For this analysis, the strain will be defined relative to the brine volume (3.25) as it yields a reasonable strain measure for the pressure analysis.

i.e.,

$$e_T^B(V, V_o) = \int_{V_o=V_o^B}^{V} \frac{dV_T^O}{V_T^B}. \tag{3.24}$$

Notice that this strain measure is analogous to a logarithmic strain measure. Making the change of variables from volumetric measures to salinity (3.22), the strain can be described by

$$\begin{aligned} e_T^B(s^B, s_o^B) &= \int_{s_o^B}^{s^B} \left[\frac{\rho^W}{\rho^I \zeta^B} + \xi \frac{1}{s^B} - \frac{1}{s^B + \zeta^B} \right] ds^B \\ &= \left[\frac{\rho^W}{\rho^I} \left(\frac{s^B - s_o^B}{\zeta^B} \right) + ln \left(\frac{s^B}{s_o^B} \right)^{\xi} \left(\frac{\zeta^B + s_o^B}{\zeta^B + s^B} \right) \right], \end{aligned} \tag{3.25}$$

where ξ is defined in Equation (3.22).

To obtain the volumetric strain measure as a function of temperature, replace the brine salinity (s^B) with a function of temperature, $s^B(T)$ defined in Equation (3.2), so that

$$e_T^B = e_T^B(s^B, s_o^B) = e_T^B(s^B(T), s^B(T_o)). \tag{3.26}$$

To study the behavior of this strain function, recall $\zeta^B = 1.25$ as defined in Equation (3.3), let the specific gravity of ice (ρ^I/ρ^W) equal 0.917, and let the initial temperature $T_o = -2\,^\circ\mathrm{C}$[11]; the resulting volumetric strain profile is shown in Figure 13.

Polynomial Approximations

For numerical models, polynomials are much easier to work with. By choosing an initial temperature (T_o), corresponding to the initial salinity of the brine (s_o^B) immediately after the cell is sealed, the volumetric strain can be approximated by a fifth order polynomial. For the initial temperature, let $T_o = -2\,^\circ\mathrm{C}$.

[11]For the present, assume the trapped brine starts with a salinity of 0.035, though it is likely to be higher.

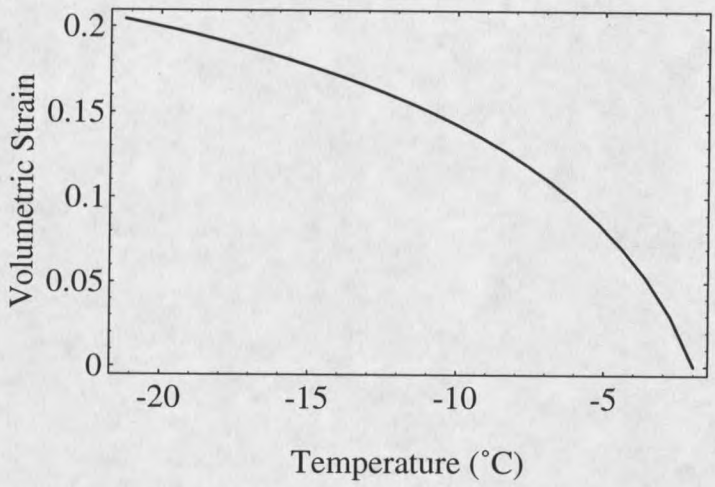

Figure 13. Volumetric Transformation Strain (e_T^B)

To model the entire range between the initial temperature and the eutectic temperature ($T_e = -21.2\,°\mathrm{C}$), the Chebyshev polynomials were used as a basis[12], obtaining a polynomial approximation with a maximum offset of 1.24×10^{-3}, which occurred at T_o.

The polynomial approximation takes the following form

$$\tilde{e}_T^B = -\left(\sum_{j=0}^{5} \gamma_j T^j\right) \times 10^{-6} \tag{3.27}$$

with the coefficients listed in Table 1, where T is in degrees Celsius.

In some cases, it is advantageous to model the transformation expansion as thermal expansion. If large (logarithmic) strain components are used, the volumetric

[12]For polynomial approximations of the form required here, Chebyshev proved that Chebyshev polynomials minimize the maximum error for such an approximation (Hamming 1973, §28.5).

For the Chebyshev approximation ($\tilde{e}_T^B$), the least squares technique (Atkinson 1989, §4.5) was used. Starting with a basis of the Chebyshev polynomials (τ_j) yields

$$\tilde{e}_T^B(x) = \frac{c_o}{2} + \sum_{j=1}^{4} c_j \tau_j(x), \qquad \text{where} \qquad c_j = \frac{2}{\pi} \int_{-1}^{1} \frac{e_T^B(x)\tau_j(x)dx}{\sqrt{1-x^2}}$$

and x is related to the temperature (T) by $T = [(T_o - T_e)x + (T_o + T_e)]/2$. The resulting approximation can then be rearranged into standard form (3.27).

	$\tilde{e}_T^B$			α
γ_0	98675.9		β_0	16714.8
γ_1	63399.2		β_1	2245.22
γ_2	7756.88		β_2	172.983
γ_3	558.147		β_3	6.63967
γ_4	20.5021		β_4	0.0987772
γ_5	0.296332		$\tilde{T}_o$ [°C]	-1.96783

Table 1. Polynomial parameters

strain can be represented by

$$e_T^B = 3\alpha\Delta T, \tag{3.28}$$

where α is the coefficient of thermal (transformation) expansion for one dimension and $\Delta T = T - T_o$ is the temperature difference between the initial stress-free temperature (T_o) and the brine temperature (T). To approximate the expansion coefficient, recall the expansion is zero at the initial temperature (T_o). As a consequence, for the polynomial approximation (3.27), there is a root ($\tilde{T}_o$) near T_o; therefore $\Delta T = (T - \tilde{T}_o)$ can be factored out of the polynomial model (i.e.,$\alpha = \tilde{e}_T^B/(3\Delta T)$), so that

$$\alpha[^\circ\mathrm{C}^{-1}] = -\left(\sum_{j=0}^{4} \beta_j T^j\right) \times 10^{-6} \tag{3.29}$$

for $T_e \leq T \leq T_o$ with the parameters given in Table 1, where T is in degrees Celsius.[13]

Discussion

Notice that the volumetric strain (e_T^B) is larger than might be expected relative to a simple transition from water to ice.[14] This discrepancy results from the difference in

[13]To clarify the relationship between the two polynomial approximations, notice

$$\sum_{j=0}^{5} \gamma_j T^j = 3(T - T_o) \sum_{j=0}^{4} \beta_j T^j.$$

[14]The volumetric strain resulting from a transition from water to ice can be simply modeled by

$$\frac{\Delta V}{V} = \frac{\rho^W - \rho^I}{\rho^I} = 0.0905.$$

reference volumes, i.e., the volumetric strain is measured relative to the brine volume rather than the the total cell volume. This apparent strain, when multiplied by the brine pressure, would allow us to approximate the work required to deform the ice-brine interface into its equilibrium configuration, while the standard strain measure would not yield such a correlation. In other words, the strain represented by e_T^B is not small; therefore *engineering* strain measures do not make good approximations.

Elastic Model for Brine Pressure

In this section, the volume changes modeled in the previous section are used to evaluate the build up of hydrostatic pressure in the brine. The stress fields in the surrounding ice are of primary interest, but the brine pressure will serve as a boundary condition for the stresses in the ice.

For the pressure estimate itself, a sequence of differentials can be combined to obtain a solution and explore the salinity-temperature dependence of the pressure build up in the brine cells. The approach used here is similar to one used by Picu, Gupta & Frost (1994, §1.2), though the results appear to be significantly different.[15]

In the previous section, the volume changes in the components were modeled by assuming the brine and precipitated ice were allowed to overlap, Figure 12. In this section, compatibility will be enforced between the brine and ice as illustrated in Figure 14, so that the pressure that accumulates as ice precipitates from the brine can be modeled.

[15]Based on the inverse relationship between the brine volume and the brine salinity (3.10), one would expect the slope of the pressure profile to decrease at the lower temperatures due to the decrease in the volume of brine available for the precipitation of ice. The pressure profile plotted by Picu et al. (1994, Fig. 3) displays an increasing slope at lower temperatures (higher salinities). The differential relations used here are similar to those used by Picu, Gupta, and Frost; therefore, the lapse most likely occurred in the integration of the differential relations.

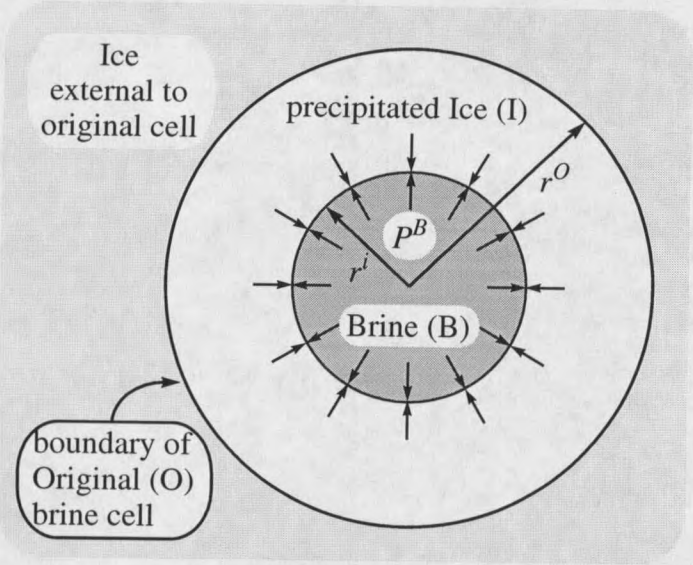

Figure 14. Conceptual (spherical) model for a brine cell

As a first approximation, a brine cell will be modeled as spherical in shape with surrounding ice that extends ad infinitum.

Notation

In addition to the notation of the previous section, the subscript E denotes components due to material constraints and the superscript i denotes parameters related to the brine-ice interface.

In particular, let r^i represent the radius of the brine-ice interface and P^B represent the hydrostatic pressure in the brine and hence the pressure at the interface.

Compatibility

If compatibility is enforced at the interface between the precipitated ice (I) and the brine (B), the displacement for each side of the interface can be divided into two components. The first component expresses the displacement of the interface due to phase transformations, denoted with the subscript T. The second component expresses the

displacement of the interface due to the pressure at the interface, denoted with the subscript E. To satisfy compatibility, the total displacement differential must be the same for each side of the interface, i.e.,

$$du_T^I + du_E^I = du_T^B + du_E^B \tag{3.30}$$

Using an elastic model for concentric spheres (Love 1944, §98) and assuming the outer radius of the ice mass is very large with no external pressure implies

$$du_E^I = \frac{r^i dP^B}{4\mu^I}, \tag{3.31}$$

where du_E^I is the radial displacement of the inner radius of the surrounding ice mass due to a brine pressure increment (dP^B) and μ^I represents the shear modulus of ice.

For the stress free displacement of the ice interface,

$$V_T^I = V_T^O - \frac{4}{3}\pi(r^i)^3. \tag{3.32}$$

Because the primary concern is with the transformation displacement and the original cell is constrained by the surrounding ice, assume the precipitation of ice results in displacement of the interface rather than changing the outer boundary (i.e., $dV_T^I = 0 - 4\pi(r^i)^2 du_T^I$), so that

$$du_T^I = -\frac{dV_T^I}{4\pi(r^i)^2}. \tag{3.33}$$

For the differential displacement of the brine interface resulting from the constraining forces of the surrounding ice

$$dV_E^B = -\frac{V^i}{K^B} dP^B, \tag{3.34}$$

where K^B is the bulk modulus of the brine. If this relation is expressed in terms of the spherical geometry of the conceptual model, then

$$4\pi(r^i)^2 du_E^B = -\frac{4\pi(r^i)^3}{3K^B} dP^B \tag{3.35}$$

so that

$$du_E^B = -\frac{r^i}{3K^B} dP^B. \tag{3.36}$$

For the stress free displacement of the interface viewed from the brine,

$$V_T^B = \frac{4}{3}\pi (r^i)^3 \tag{3.37}$$

implies

$$dV_T^B = 4\pi (r^i)^2 du_T^B. \tag{3.38}$$

Solving for the differential displacement yields

$$du_T^B = \frac{dV_T^B}{4\pi (r^i)^2}. \tag{3.39}$$

This gives us expressions for all of the displacement components.

Pressure Model

To finish the development of the pressure model, the expressions for the differential displacements (3.31, 3.33,3.36, 3.39) can be substituted into the compatibility equation (3.30), to get

$$\frac{r^i}{4\mu^I} dP^B - \frac{dV_T^I}{4\pi (r^i)^2} = -\frac{r^i}{3K^B} dP^B + \frac{dV_T^B}{4\pi (r^i)^2}. \tag{3.40}$$

Combining terms and solving for dP^B,

$$dP^B = \left(\frac{3}{4\mu^I} + \frac{1}{K^B}\right)^{-1} \frac{dV_T^B + dV_T^I}{V^i}. \tag{3.41}$$

Recognizing that $dV_T^O = dV_T^B + dV_T^I$ and that the the brine volume (V_T^B) is a reasonable approximation for the volume enclosed by the interface (V^i), then

$$dP^B = \left(\frac{3}{4\mu^I} + \frac{1}{K^B}\right)^{-1} \frac{dV_T^O}{V_T^B}. \tag{3.42}$$

Integrating

$$P^B = \left(\frac{3}{4\mu^I} + \frac{1}{K^B}\right)^{-1} e_T^B, \tag{3.43}$$

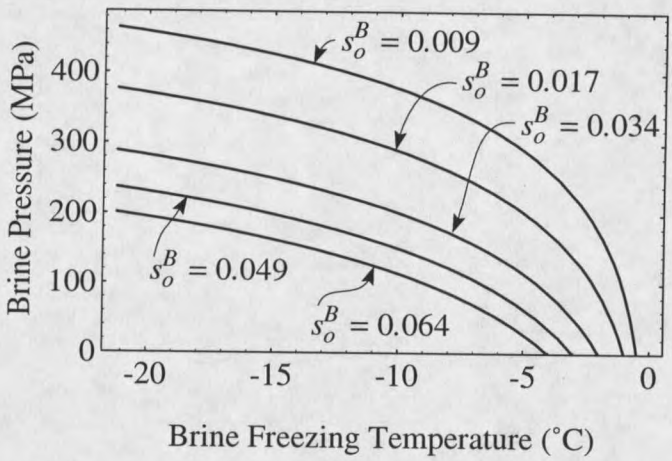

Figure 15. Brine pressure (P^B) as a function of temperature and initial salinity (s_o^B).

where the volumetric strain (e_T^B) was defined previously, Equation (3.25). This model seems fairly intuitive.[16]

Example

To study the behavior of the resulting pressure function, let the bulk modulus of the brine (K^B) equal 2.0 GPa and let the shear modulus for the ice (μ^I) equal 3.6 GPa. Then using the volumetric strain function (3.25) with initial temperatures of $T_o = -0.5, -1, -2, -3$, and $-4\,°\text{C}$, yields the pressure profiles shown in Figure 15.

Notice the pressure becomes significant immediately after the brine cell is

[16]In essence, the elastic deformation can be represented by two springs in series. The modulus for one spring ($4\mu^I/3$) represents the ice and the modulus for the other spring (K^B) represents the brine. Then the effective modulus for the series combination is the reciprocal of the sum of the reciprocals of the two separate moduli.

For an upper bound, assume the ice is rigid so that the entire volume change due to the phase transformation must be absorbed by the brine. Using an elastic model, where the brine has a bulk modulus (K^B), the upper bound for the brine pressure (P_{ub}^B) is

$$P_{ub}^B = K^B \int_{V_o^B}^{V_T^B} \frac{dV_T^O}{V_T^B} = K^B e_T^B.$$

This upper bound corresponds with $lim_{\mu^I \to \infty} P^B$, using the definition of P^B in Equation (3.43).

sealed and begins to cool, particularly for cases with low initial salinity. For the cell model with an initial temperature $T_o = -2\,^\circ\mathrm{C}$, by the time the temperature drops one degree, the brine pressure (P^B) approaches 50 MPa and reaches a maximum of 285 MPa at the eutectic point ($T_e = -21.2\,^\circ\mathrm{C}$).

As might be expected, given the inverse relationship between brine volume and salinity (3.10), the rate of change in the pressure for a change in temperature is dependent on the salinity of the brine. Brine cells which start with a low initial salinity display pressure profiles that are much steeper initially, but that leveling off to profiles that are parallel to pressure profiles for brine cells that started with a higher initial salinity.

Discussion

As can be ascertained, the elastic model would not be valid after inelastic deformation begins and as illustrated, Figure 15, the pressure modeled at the brine-ice interface approaches the theoretical maximum strength for ice, $\mu^I/10 = 360$ MPa; hence, there is little doubt that the stresses are sufficient to induce inelastic deformation. Though the model is inaccurate for large temperature changes, the model may be useful for estimating the temperature change required to induce yielding or for estimating the extent of possible yielding.

Elastic Model for Stress Distributions

Though the pressures in the brine cell can become so large that the elastic model becomes invalid, it is still worthwhile to consider the range of material that might be affected by such a pressure build up.

As a model of the stress distribution in the neighborhood of the brine cell, consider an elastic model of concentric spheres (Timoshenko & Goodier 1970, §136), and

take the limit as the outer radius grows large. Let R_i represent the non-dimensional radius, r/r^i, where r^i is the radius to the interface between the brine and the precipitated ice. Using the brine pressure (P^B) as a boundary condition at the interface, the stress components take the following form:

$$\sigma_{rr} = -\frac{P^B}{R_i^3}\,;\ 1 \leq R_i < \infty \tag{3.44}$$

$$\sigma_{tt} = +\frac{P^B}{2R_i^3}\,;\ 1 \leq R_i < \infty \tag{3.45}$$

$$(\tau_{xz})_{max} = -\frac{3P^B}{4R_i^3}\,;\ 1 \leq R_i < \infty \tag{3.46}$$

In the case of the brine cell, as the pressure accumulates, the radial location of the interface (r^i) decreases. To approximate the location of the interface relative to the initial position of the interface (r_o^i), recall the ratio of the brine volume relative to the initial brine volume (3.9), substitute for the volume in terms of the spherical geometry of the brine cell model ($V = 4\pi r^3/3$), and approximate the interface radius (r^i) by the brine radius (r^B), to get

$$\frac{r^i}{r_o^i} \approx \frac{r^B}{r_o^B} = \left[\frac{s_o^B(\zeta^B + s_o^B)}{s^B(\zeta^B + s^B)}\right]^{1/3} \tag{3.47}$$

Using this relationship, it is possible to define a new non-dimensional radius (R_o) relative to the initial radius, i.e.,

$$R_o = \frac{r^i}{r_o^i} R_i = \frac{r}{r_o^i} \tag{3.48}$$

With the preceding information, the elastic stress profiles in the neighborhood of the brine cell, due to phase transformations, can be modeled.

Example

Let the initial interface radius $r_o^i = 1$ for an initial temperature $T_o = -2\,^\circ\mathrm{C}$. Then the stress profiles for temperatures $T = -2.5, -3, -8$, and $-21.2\,^\circ\mathrm{C}$ are shown in Figure 16 with corresponding interface radii $r^i = 0.93$, 0.88, 0.64, and 0.50.

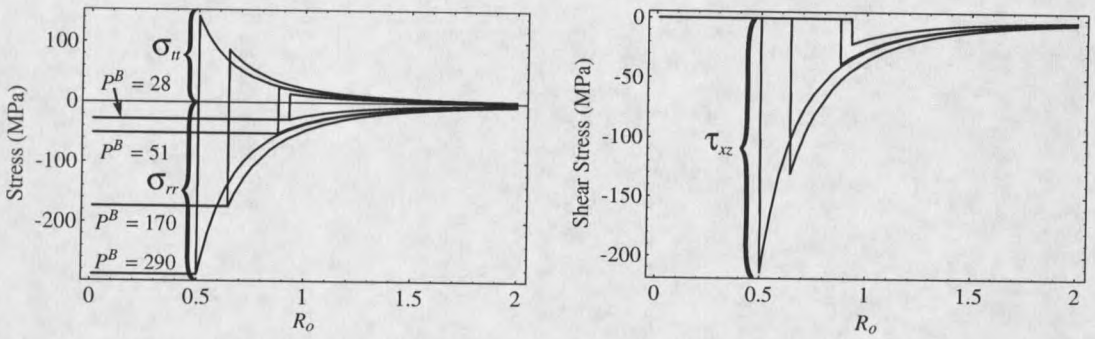

(a) Principal components (b) Maximum Shear

Figure 16. Stress Profiles for the brine cell

Notice the stresses transferred to the region outside of the original brine cell change relatively little as the temperature drops. As the brine pressure increases, the pressure increase is born by the precipitating ice that generates the pressure increase.

Discussion

The predominant concern regards the extent of inelastic deformation that might occur in the neighboring ice due to the pressures generated in the brine. As discussed in the previous section, the stresses resulting from the elastic model are well beyond the yield stress for ice. Higashi (1964) shows yield in non-saline single crystals of ice for basal plane shear stresses ranging from 0.06 to 0.44 MPa with strain rates in the range of $0.13 - 2.7 \times 10^{-6}$ s^{-1} and temperatures in the range of -21 to $-15\,°C$. At warmer temperatures and lower rates, where phase transformations would be expected to have a more significant impact, yield would likely occur at even lower stresses.

Comparing this observation with the results in Figure 16, one can conclude that inelastic deformation takes place almost immediately after the brine pocket has sealed off and the temperature begins to drop. Therefore the pressure/stress curves shown in Figure 16 are unrealistic for saline ice and serve only to show the significance

of inelastic deformation that might occur during crystal growth, if the ice surrounding the cell does not fracture immediately.

Wakahama (1966) deduced that for temperatures near $-10\,^{\circ}\mathrm{C}$, basal slip would occur in ice single crystals for basal plane shear stresses between 0.02 and 2 MPa. For shear stresses above 2 MPa, the ice crystals would fracture. For the sake of argument, assume the shear stress at the interface is near the maximum ($\tau^i_{xz} = 2$ MPa) for basal slip. Using the elastic model (3.46), it is possible to estimate brine pressure ($P^B = -4\tau^i_{xz}/3$), as well as the radial location at which shear stresses have decayed to the minimum "yield" point ($\tau^r_{xz} = 0.02$ MPa), i.e.,

$$R_i = \left(\frac{\tau^i_{xz}}{\tau^r_{xz}}\right)^{1/3} \approx 5 \tag{3.49}$$

Indicating that there is the potential for inelastic deformation at distances up to 5 times the interface radius (r^i) away from the brine cell. Because inelastic deformation would occur over the range ($r^i \leq r \leq 5r^i$), this estimate, from the elastic model, of the range of inelastic deformation is only a rough approximation.

Elastic-Anisotropic Finite Element Model

Thus far the ice forming the brine cell has been modeled as isotropic. Since brine cells will in general be embedded in single or quasi-single crystals, it is worthwhile to consider the behavior of the model using anisotropic properties. For this analysis, a finite element model will be used. Also, in the future, it would be preferable to use a model that is a closer approximation to the expected brine cell in saline ice, both in terms of geometry and constitutive relations. By comparing this model with the preceding closed form models, the finite element techniques can be validated for future use.

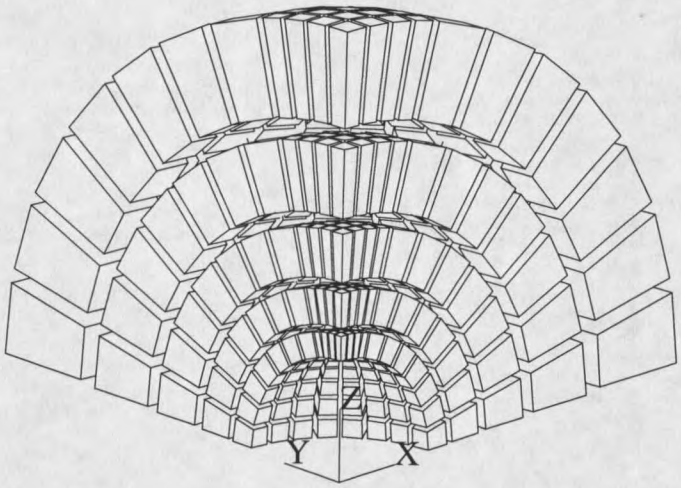

Figure 17. Inner section of the finite element model of a spherical ice cell

Set Up

The stress field that develops in the ice was modeled using the (ANSYS 1995) finite element (FE) model shown in Figure 17.

Due to the rapid decay of the stress field near the ice-brine interface (Fig. 16), the shape functions in an FE model will tend to underestimate the stresses at the interface. The accuracy of the FE model was evaluated with a test case where an internal pressure ($P^B = 100$ MPa) was applied. The results were then compared with the equilibrium stress relations for concentric spheres (3.44-3.46). With the curved boundaries and somewhat distorted elements, better results were achieved by using elements with quadratic shape functions (i.e. ANSYS, SOLID95). Additionally, to obtain results that were accurate at the inner radius, it was necessary to use a sub-modeling (mesh refinement) technique. The coarse model had an outer radius which was twenty times greater than the inner radius. This "coarse" mesh was then used to define displacement boundary conditions for the outer radius of a much finer model where the outer radius was only four times as large as the inner radius. By using this

sub-modeling technique, the maximum discrepancy between the FE model and the exact solution (3.44-3.46), which occurred at the interface radius, r^i, was reduced to less than 3%. If only the coarse mesh was used, the stresses at the inner radius were underestimated by more than 10%.

To model the brine, the spherical vacancy was filled with a second mesh. The same element type was used for both the brine and the ice shell, though the material parameters were altered.

It was assumed that the model took the "stress-free" configuration at $-2\,^{\circ}\mathrm{C}$. To model the interference between the brine and ice due to the phase transformations, the ice interface was used as a frame of reference, so that the interference was due to the "apparent" transformation expansion of the brine. To model the "apparent" expansion of the brine in the finite element model, the volumetric strain was modeled as a thermal expansion, using the large (logarithmic) strain capabilities of ANSYS. The components of thermal (transformation) strain were represented by

$$\{\epsilon_T^B\}_i = \alpha \Delta T = e_T^B/3, \tag{3.50}$$

where $\Delta T = T - T_o$ is the temperature difference between the initial stress-free temperature (T_o) and the brine temperature (T) and α is the coefficient of thermal (transformation) expansion, defined in Equation (3.29).

The elastic parameters of the brine were defined as a bulk modulus of 2 GPa and a Poisson's ratio of .498. For the surrounding ice, the coefficient of thermal expansion was, $\alpha^I \approx 53 \times 10^{-6}$, as given in Fletcher (1970), though it is negligible relative to the transformation coefficient.

To validate the accuracy of the FE model relative to the preceding closed form model, the FE model was evaluated for $T = -8\,^{\circ}\mathrm{C}$ using the following isotropic elastic parameters for the ice (Derradji-Aouat 1992, Table 4.3),

$$E^I = 9.41 \text{ GPa} \qquad \text{and} \qquad \nu^I = 0.308.. \tag{3.51}$$

To evaluate the differences in the two isotropic models, the radial stress data from the FE model was modeled using a least squares fit of the form $-\tilde{P^B}/R_i^3$, obtaining $\tilde{P}^B = -170$ MPa with a correlation coefficient of 0.9991 and a standard error of 1.02 MPa. Comparing this pressure estimate with the pressure estimate from the closed form model (3.43) yielded a difference of 2.5%, presumably due to the included thermal contraction of the ice and interpolation errors.

To determine the significance of the anisotropic material model relative to the isotropic material model, the following orthotropic material parameters were used:

$$\begin{aligned} E_x^I = E_y^I = \frac{1}{S_{11}} &= 9.70 \text{ GPa} & E_z^I = \frac{1}{S_{33}} &= 11.9 \text{ GPa} \\ \nu_{xz}^I = \nu_{yz}^I = -\frac{S_{13}}{S_{33}} &= 0.223 & \nu_{xy}^I = -\frac{S_{12}}{S_{11}} &= 0.427 \\ G_{xz}^I = G_{yz}^I = \frac{1}{S_{44}} &= 3.03 \text{ GPa} & G_{xy}^I = \frac{1}{S_{66}} &= 3.40 \text{ GPa} \end{aligned} \tag{3.52}$$

Numerical values are based on Dantl's (Dantl 1968, Dantl 1969) polynomial models for the compliance parameters (S_{ij}), evaluated at a temperature of $-8\,^\circ$C.

Analysis

Using the preceding isotropic properties, the FE model produced the tangential (σ_{tt}) and shear (τ_{xz}) stress fields shown in Figure 18a and Figure 18c, respectively. The corresponding maximum stresses are shown in Table 2. Using the anisotropic properties, the FE model rendered the tangential (σ_{tt}) and shear (τ_{xz}) stress fields shown in Figure 18b and Figure 18d, respectively. The corresponding maximum stresses are shown in Table 2.

The stress contours shown in Figures 18c and 18d represent the magnitude of the shear stress that would result on the basal plane of the ice crystal, if it remained elastic.

Given that most of the anisotropic elastic parameters (3.52) are within 30% of the isotropic components (3.51), it is reasonable to expect the stress results to

	Maximum Stresses (at the interface)	
Stress Component	Isotropic Model	Anisotropic Model
σ_{rr} [MPa]	- 164	- 164
σ_{tt} [MPa]	+ 88.5	+ 151
τ_{xz} [MPa]	- 126	- 114

Table 2. Stress components at the interface

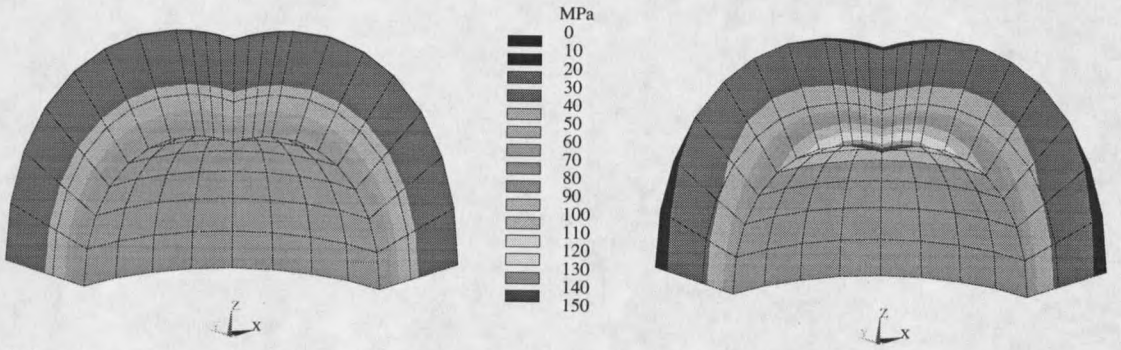

(a) σ_{tt} contours (Isotropic Model)

(b) σ_{tt} contours (Anisotropic Model)

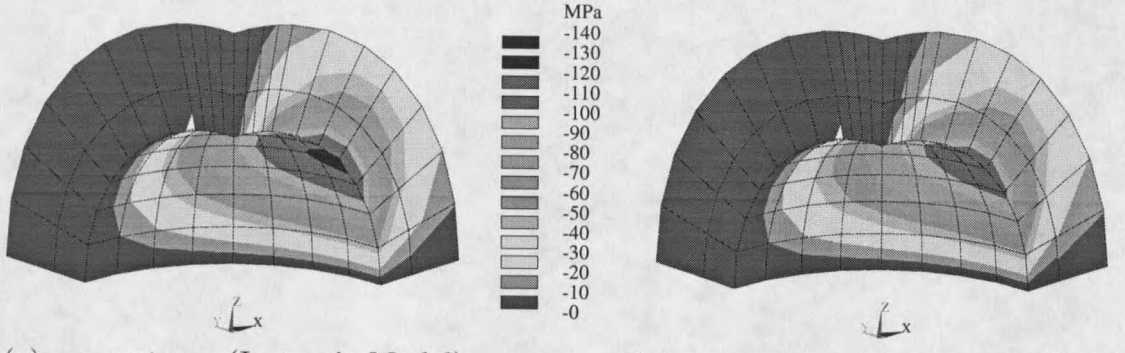

(c) τ_{xz} contours (Isotropic Model)

(d) τ_{xz} contours (Anisotropic Model)

Figure 18. Stress contours ($T = -8\,^{\circ}\mathrm{C}$)

reflect the same order of similarity. The contour plots in Figure 18 demonstrate such a case. The radial stress contour plots displayed so much similarity that they were not deemed worth including.

Consider the stresses in the xy plane. Because the z-axis in Figure 18 corresponds with the crystalline c-axis; the elastic model is isotropic in the xy (basal)

plane. In this plane, the only noticeable difference relative to the isotropic model is that the magnitude of the radial and tangential stress components decay slightly slower and faster, respectively, relative to R_i.

For stresses along the z-axis, the behavior is again very similar to the isotropic case, except the rate of decay in the magnitude of the radial stress component is significantly slower, yielding a magnitude 100% greater when $R_i = 4$.

Given the magnitude of the stresses predicted, this model is primarily useful for predicting the onset of yielding. Therefore, the primary concern is the magnitude of the shear components that would act on the basal plane. Comparing the shear stress contour plots (Figure 18c and 18d), it is clear that the change in the shear stress field due to anisotropic properties is small. The only notable observation is that in the anisotropic case, the shear stress displays a maximum which is about 10% less, combined with a slightly faster rate of radial decay relative to the isotropic case.

The shear stress contours (Figure 18c and 18d) illustrate that basal plane shear stresses will be significant only at specific points on the surface of the brine pocket model. These are the points where the basal plane makes a forty-five degree angle with direction perpendicular to the brine pocket surface. As a consequence, one would expect to first see dislocations emerging from these preferred regions on the brine pocket interface.

Discussion

In summary, based on comparisons between models with isotropic and anisotropic material parameters for single crystals of ice, the isotropic elastic model yields approximations that are very reasonable relative to the anisotropic case. In particular, the isotropic model works quite well for predicting the onset of yield, though it may be a bit conservative.

Inelastic Model

Thus far the elastic components of deformation have been modeled while the inelastic components have been ignored. As discussed in the previous sections, the elastic model demonstrates that stresses are more than sufficient to activate inelastic deformation. As a result, the next step is to include the inelastic component.

Rate Compatibility

As with the elastic component, the model will be tied together by requiring the compatibility of displacements at the brine-ice interface. To include the history dependence of inelastic components, the model will be defined in terms of displacement rates. The deformation rate of the ice will be modeled as the sum of a thermal (transformation) part ($\dot{u}_T^I$), an elastic part ($\dot{u}_E^I$) resulting from material constraints, and a plastic part ($\dot{u}_P^I$). Spherical symmetry requires the deformation to be purely radial so that the time derivative of the compatibility equation takes the form:

$$\dot{u}_P^I + \dot{u}_E^I + \dot{u}_T^I = \dot{u}_E^B + \dot{u}_T^B \tag{3.53}$$

Except for the elastic and plastic parts of the ice deformation, the differential displacement components have been modeled (Equations 3.33, 3.36, and 3.39) and were converted to the following displacement rates by dividing each component by a time differential.

$$\dot{u}_T^I = -\frac{\dot{V}_T^I}{4\pi(r^i)^2} \qquad \dot{u}_T^B = \frac{\dot{V}_T^B}{4\pi(r^i)^2} \qquad \dot{u}_E^B = -\frac{r^i}{3K^B}\dot{P}^B \tag{3.54}$$

Notice the displacement rate ($\dot{u}_E^I$) derived for the elastic model cannot be used because of its dependence on an elastic stress distribution. Now consider models for the elastic ($\dot{u}_E^I$) and plastic ($\dot{u}_P^I$) components. To model these components, relationships have been adapted from other works (Finnie & Heller 1959, Mendelson 1968, Wilkinson & Ashby 1975, Picu et al. 1994).

Strain-Displacement Rate Relations

With spherical symmetry, principal strain components can described as radial (ϵ_r^p) or tangential ($\epsilon_t^p = \epsilon_\theta^p = \epsilon_\phi^p$). At the same time, principal strain directions cannot rotate and the principal strain components can be differentiated directly with respect to time; therefore, for the spherical brine cell model, the strain-displacement relations,

$$\epsilon_r = \frac{du^I}{dr} \qquad \text{and} \qquad \epsilon_t = \frac{u^I}{r}, \tag{3.55}$$

differentiated with respect to time, are represented by,

$$\dot{\epsilon}_r = \frac{d\dot{u}^I}{dr} \qquad \text{and} \qquad \dot{\epsilon}_t = \frac{\dot{u}^I}{r} - \frac{u}{r^2}\dot{r} \approx \frac{\dot{u}^I}{r}. \tag{3.56}$$

Notice the tangential component of the strain-rate is directly related to the displacement-rate. If this component is evaluated at the interface,

$$\dot{u}^I = r^i \dot{\epsilon}_t. \tag{3.57}$$

Consider this relationship for the elastic component ($\dot{u}_E^I$), then

$$\dot{u}_E^I = r\dot{\epsilon}_t = \frac{r^i}{E^I}\left[\dot{\sigma}_t - \nu^I(\dot{\sigma}_t + \dot{\sigma}_r)\right] + r^i\alpha\dot{T} \tag{3.58}$$

$$\approx \frac{r^i}{E^I}\left[(1-\nu^I)\dot{\sigma}_t - \nu^I\dot{\sigma}_r\right], \tag{3.59}$$

where σ_t and σ_r are the tangential and radial stress components, respectively. Because the thermal strain is negligible relative the transformation strain (3.50), it is reasonable to neglect the thermal component ($r^i\alpha\dot{T}$). Though it is reasonable to represent the elastic component locally by a linear elastic model (3.59), it is not reasonable to represent the global stress field by a linear elastic stress distribution[17] if

[17]For a linear elastic stress distribution,

$$\dot{u}_E^I = \frac{r^i}{E}\left[(1-\nu)\frac{\dot{P}^B}{2} + \nu\dot{P}^B\right] = \frac{r^i(1+\nu)}{2E}\dot{P}^B = \frac{r^i}{4\mu^I}\frac{dP^B}{dt}.$$

inelastic deformation is also occurring. Because the stress field cannot be represented by a linear elastic stress distribution, there is not a direct method for relating the two stress components to the brine pressure; therefore this definition will be completed later in the chapter.

For the inelastic component of the ice ($\dot{u}_P^I$), recall strain-displacement rate relation (3.57). Then, if the isotropic Prandtl-Reuss constitutive model (Mendelson 1968, §7.2) is used, the tangential component of the plastic strain rate can be expressed as

$$\dot{u}_P^I = r^i \dot{\epsilon}_t^p = r^i \frac{\dot{\epsilon}_e^p}{2} \operatorname{sgn}(\sigma_t - \sigma_r), \tag{3.60}$$

where $\dot{\epsilon}_e^p$ is the equivalent plastic strain rate, i.e.,

$$\dot{\epsilon}_e^p = \frac{2}{3} |\dot{\epsilon}_t^p - \dot{\epsilon}_r^p|. \tag{3.61}$$

The sign function, $\operatorname{sgn}(\cdot)$, takes the value of ± 1 based on the sign ($\pm$) of its argument.

For those cases where the radial stress is compressive and the tangential stress is less in magnitude, as for the case of concern, the sign function takes a value of 1.

Volumetric Compatibility

Substituting for each of the displacement rate components (3.54, 3.59, 3.60) in the differential compatibility equation, $\dot{u}_P^I + \dot{u}_E^I + \dot{u}_T^I = \dot{u}_E^B + \dot{u}_T^B$ (3.53) yields

$$\frac{r^{i\cdot}}{2}\dot{\epsilon}_e^p + \frac{r^i}{E^I}\left[(1-\nu^I)\dot{\sigma}_t - \nu^I \dot{\sigma}_r\right] - \frac{1}{4\pi(r^i)^2}\frac{dV_T^I}{dt} = -\frac{r^i}{3K^B}\frac{dP^B}{dt} + \frac{1}{4\pi(r^i)^2}\frac{dV_T^B}{dt} \tag{3.62}$$

Recognize that the spherical volume enclosed by the brine-ice interface can be expressed as $V^i = 4\pi(r^i)^3/3$ and the overall differential transformation volume can be expressed as $dV_T^O = dV_T^B + dV_T^I$. Applying these changes and substituting the brine volume (V^B) as an approximation of the volume enclosed by the interface (V^i) implies

$$\underbrace{\frac{\dot{P}^B}{K^B} + \frac{3}{E^I}\left[(1-\nu^I)\dot{\sigma}_t - \nu^I\dot{\sigma}_r\right]}_{Elastic} + \underbrace{\frac{3}{2}\dot{\epsilon}_e^p}_{Inelastic} = \underbrace{\frac{\dot{V}^O}{V^B}}_{Transform} \tag{3.63}$$

Each term in this differential expression (3.63) gives us a measure of the apparent volumetric strain rate due to each of the deformation components in the spherical brine cell model.

For this analysis, assume it is possible to define the temperature history of a brine cell and therefore its transformation strain rate. If the equivalent strain rate is defined in terms of the equivalent stress, it will be necessary to relate the two spherical stress components (σ_r and σ_t) and their derivatives to the brine pressure (P^B) and its derivative. Notice that at the interface, the radial stress and its derivative are the negative of the brine pressure and its derivative, respectively. If this differential equation is linearized, for the creep strain rate, the tangential components can be related to the radial components in a rather straight forward manner. Unfortunately, in the non-linear case, the equilibrium equation cannot be applied so easily. To obtain a reasonably simple solution, the equilibrium equation can be applied only in an approximate manner. With the finite element method (ANSYS 1995), it is possible to be more exact in the modeling process. The details of these procedures will be discussed in the following sections.

Equivalent Plastic Strain Rate Model

To solve the differential compatibility equation (3.63), it is necessary to first determine an adequate model for the equivalent plastic strain rate. For low stresses, it is common to define the equivalent plastic strain rate with a power-law dependence on equivalent stress and an Arrhenius-type (exponential) dependence on temperature.

$$\dot{\epsilon}_e^p = A(\sigma_e)^n \exp\left(-Q/kT\right). \tag{3.64}$$

where A is a constant and n is the stress exponent. Q is the activation enthalpy, k is Boltzmann's constant, and T is the absolute temperature. Because the primary

concern is with the power law relation between the equivalent plastic strain-rate increment and the equivalent stress, this relationship can be written as

$$\dot{\epsilon}_e^p = B\sigma_e^n, \tag{3.65}$$

where

$$B = A \exp(-Q/kT). \tag{3.66}$$

For uniaxial loading, Glen (1953) demonstrated that such a power law relationship modeled minimum creep rates reasonably well for stresses between 0.1 and 1 MPa. As a result, this model will be used as a first approximation and as a tool to gain insight into the modeling process.

Flow Stress Distribution

To define the stress distribution, it is necessary to consider the balance between elastic and inelastic mechanisms; however, due to the intractable nature of such considerations, it will be assumed that the stress distribution is dominated by viscous resistance or inelastic flow. The consequences of this simplification will be discussed in the next section.

The Prandtl-Reuss constitutive model chosen for plastic deformation assumes that there is no volume change due to the plastic strains.[18] Expressing the volumetric constancy in terms of the principal strain and differentiating with respect to time yields

$$\dot{\epsilon}_r^p = -2\dot{\epsilon}_t^p. \tag{3.67}$$

[18]Plastic deformation is considered to be predominantly due to the exchange of molecular bonds rather than the expansion and contraction of molecular bonds. As a result, the corresponding volume change is considered to be quite small. In addition, experimental observations indicate that volume changes are negligible even after significant plastic deformation has occurred Mendelson (1968, §2.4).

Substituting the corresponding strain-displacement rate relations (3.56) into the volumetric constraint (3.67) and separating variables:

$$\frac{d\dot{u}^p}{\dot{u}^p} = -2\frac{dr}{r}. \tag{3.68}$$

Integrating and solving for the displacement rate ($\dot{u}^p$) and substituting back into the strain-rate expressions (3.56, 3.67) implies

$$\dot{\epsilon}_r^p = -2\dot{\epsilon}_t^p = \frac{\mathcal{K}}{r^3}, \tag{3.69}$$

where $\mathcal{K}$ is an integration constant.

For the spherically symmetric model, the equilibrium constraint takes the form:

$$\frac{d\sigma_r^I}{dr} + \frac{2}{r}(\sigma_r^I - \sigma_t^I) = 0. \tag{3.70}$$

Similarly, the definitions for equivalent stress (σ_e) and equivalent plastic strain-rate ($\dot{\epsilon}_e^p$), [19] with the constant volume constraint (3.69), become

$$\sigma_e = \left|\sigma_t^I - \sigma_r^I\right| \tag{3.71}$$

$$\dot{\epsilon}_e^p = \frac{2}{3}\left|\dot{\epsilon}_t^p - \dot{\epsilon}_r^p\right| = \left|\dot{\epsilon}_r^p\right| = \frac{|\mathcal{K}|}{r^3} \tag{3.72}$$

while for the power law flow model, the equivalent stress is related to the equivalent plastic strain-rate by

$$\sigma_e = \left(\frac{\dot{\epsilon}_e^p}{B}\right)^{1/n} \tag{3.73}$$

Combining the previous relations (3.71-3.73), substituting into the equilibrium equation (3.70), and rearranging implies

$$r\frac{d\sigma_r^I}{dr} = 2\left(\frac{|\mathcal{K}|}{Br^3}\right)^{1/n} \tag{3.74}$$

[19] In general, the equivalent stress (σ_e) and equivalent plastic strain-rate ($\dot{\epsilon}_e^p$) are defined by

$$\sigma_e = \sqrt{3J_2} = \frac{1}{\sqrt{2}}\left[(\sigma_x - \sigma_y)^2 + (\sigma_y - \sigma_z)^2 + (\sigma_z - \sigma_x)^2 + 6(\tau_{xy}^2 + \tau_{yz}^2 + \tau_{zx}^2)\right]^{\frac{1}{2}}$$

$$\dot{\epsilon}_e^p = \frac{2}{3}\sqrt{3J_2'^p} = \frac{\sqrt{2}}{3}\left[(\dot{\epsilon}_x^p - \dot{\epsilon}_y^p)^2 + (\dot{\epsilon}_y^p - \dot{\epsilon}_z^p)^2 + (\dot{\epsilon}_z^p - \dot{\epsilon}_x^p)^2 + 6((\dot{\epsilon}_{xy}^p)^2 + (\dot{\epsilon}_{yz}^p)^2 + (\dot{\epsilon}_{zx}^p)^2)\right]^{\frac{1}{2}}$$

where J_2 and $J_2'^p$ are the 2nd invariants of the deviatoric stress tensor and the plastic strain-rate tensor, respectively.

Separating variables,

$$d\sigma_r^I = 2\left(\frac{|\mathcal{K}|}{B}\right)^{1/n} \frac{dr}{r^{3/n+1}} \tag{3.75}$$

and integrating,

$$\sigma_r^I = -\frac{D}{r^{3/n}} + F \tag{3.76}$$

where

$$D = \frac{2n}{3}\left(\frac{|\mathcal{K}|}{B}\right)^{1/n} \tag{3.77}$$

and F is a constant of integration.

To determine values for the constants D and F, use the boundary conditions:

$$\sigma_r^I(r^i) = -P^B \qquad \text{and} \qquad \lim_{r\to\infty} \sigma_r^I(r) = 0. \tag{3.78}$$

Applying the boundary conditions yields

$$\sigma_r^I = -P^B\left(\frac{r^i}{r}\right)^{3/n} \tag{3.79}$$

for $r \geq r_i$. Taking the derivative of σ_r^I and substituting back into the original equilibrium equation (3.70) and solving for σ_t^I implies

$$\sigma_t^I = \left(\frac{3-2n}{n}\right)\frac{P^B}{2}\left(\frac{r^i}{r}\right)^{3/n} \tag{3.80}$$

and

$$\sigma_e^I = \left(\frac{3}{2n}\right)P^B\left(\frac{r^i}{r}\right)^{3/n}. \tag{3.81}$$

Notice that the stress distributions are independent of the material coefficients in the constitutive model but are not independent of the stress exponent. These distributions model stresses due to steady state viscous resistance; the stresses supported by elastic strains have been considered separately. Also notice that if the stress exponent (n) is one, these equations simplify to the Lame equations for a linear elastic model. In the elastic case the stresses decay as a functions of the inverse of the radius cubed while in the inelastic case the stresses decay as a function of the inverse of the radius

to the $3/n$ power. Notice that if n assumes a value near 3, the stresses are inversely proportional to the radius r.

To solve for the equivalent strain rate, substitute the definition for the equivalent stress back into the power-law relation (3.65), so that

$$\dot{\epsilon}_e^p = B\left(\frac{3}{2n}\right)^n (P^B)^n \left(\frac{r^i}{r}\right)^3, \tag{3.82}$$

where the Arrhenius coefficient (B) was defined previously, Equation (3.66).

Differential Equation

Evaluating the equivalent plastic strain rate (3.82) and the stress components (3.79, 3.80) at the interface and substituting into the volumetric strain rate relation (3.63) yields

$$\underbrace{\frac{\dot{P}^B}{\mathcal{M}}}_{Elastic} + \underbrace{\mathcal{N}(P^B)^n}_{Inelastic} = \underbrace{\frac{\dot{V}^O}{V^B} = \dot{e}_T^B}_{Transform}, \tag{3.83}$$

where

$$\frac{1}{\mathcal{M}} = \frac{3}{E^I}\left[(1-\nu^I)\frac{3-2n}{2n} + \nu^I\right] + \frac{1}{K^B} \tag{3.84}$$

and

$$\mathcal{N} = B\frac{3}{2}\left[\frac{3}{2n}\right]^n. \tag{3.85}$$

At this point, it is not difficult to see that the differential equation has been reduced to the form represented by Maxwell visco-elastic model with non-linear viscous component as demonstrated in Figure 19. With this observation, it is easier to understand the significance of the error that results from the assumption that the stress distribution in the ice is dominated by the flow stress. The Maxwell model (Figure 19) is represented by the series combination of an elastic component and a viscous component. Due to the procedure used to incorporate the brine pressure into the differential

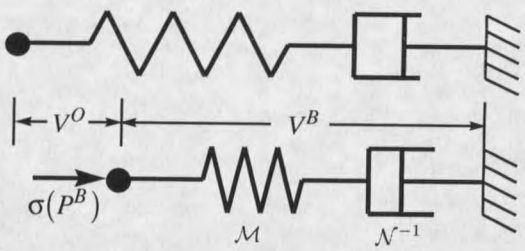

Figure 19. Maxwell Visco-Elastic Model

equation, the stress distribution was defined by the viscous component alone, though it is actually defined by both the elastic and the viscous components. To express this assumption in terms of the Maxwell model, it is assumed that the elastic component was nearly rigid, relative to the viscous component. However, because it is not rigid, the calculated brine pressure response is likely to be higher than that based on the combination of the components.

If the elastic strain components are small relative to their viscous counterparts, the errors will be relatively small (i.e., once a flow state is reached). Also, in the case where the stress exponent is 1, the stress distributions for the elastic and inelastic cases coincide and there is no error. The significance of this flow assumption will be evaluated further in the following sections.

Volumetric Strain Rate due to Phase Transformations

For the differential volumetric strain ratio (dV_T^O/V_T^B), recall that earlier (Equation 3.22), an expression of the following form was derived, i.e.,

$$\frac{dV_T^O}{V_T^B} = \left[\frac{\rho^W}{\rho^I \zeta^B} + \xi \frac{1}{s^B} - \frac{1}{s^B + \zeta^B}\right] ds^B, \tag{3.86}$$

where

$$\xi = \left(\frac{\rho^W}{\rho^I} - 1\right). \tag{3.87}$$

In the preceding expression, s^B is the salinity of the brine (3.2), $\zeta^B = 1.25$ is a constant (3.3), ρ^W represents the density of water and ρ^I represents the density of ice (3.5).

Integrating the previous expression (3.86) with respect to time yields

$$e_T^B = \int_{t_o}^{t} \left[\frac{\rho^W}{\rho^I \zeta^B} + \xi \frac{1}{s^B} - \frac{1}{s^B + \zeta^B} \right] \frac{ds^B}{dt} dt \tag{3.88}$$

$$= \int_{s_o^B}^{s^B} \left[\frac{\rho^W}{\rho^I \zeta^B} + \xi \frac{1}{s^B} - \frac{1}{s^B + \zeta^B} \right] ds^B, \tag{3.89}$$

so that

$$e_T^B(s^B, s_o^B) = \left[\frac{\rho^W}{\rho^I} \left(\frac{s^B - s_o^B}{\zeta^B} \right) + \ln \left(\frac{s^B}{s_o^B} \right)^{\xi} \left(\frac{\zeta^B + s_o^B}{\zeta^B + s^B} \right) \right]. \tag{3.90}$$

In this expression, s_o^B refers to the salinity of the brine in a cell when the brine pressure (P^B) is still zero. Recall that by assuming an initial salinity, this volumetric strain model can be approximated reasonably well by a fifth order polynomial of temperature (3.27). A polynomial approximation may be more useful in numerical routines.

Because the temperature history of a brine cell is easier to determine than the salinity history of the brine, the volumetric strain-rate ($\dot{V}^O/V^B$) will most easily be defined in differential form by

$$\frac{\dot{V}^O}{V^B} = \dot{e}_T^B = \frac{de_T^B}{ds^B} \frac{ds^B}{dT} \dot{T} = \frac{1}{V^B} \frac{dV^O}{ds^B} \frac{ds^B}{dT} \dot{T}. \tag{3.91}$$

Notice that though the volumetric strain (e_T^B) depends on the initial stress-free salinity of the brine cell (s_o^B), the volumetric strain rate ($\dot{e}_T^B$) is independent of s_o^B.

Volumetric strain rates due to phase transformations ($\dot{e}_T^B$) can be determined from values plotted in Figure 20. To estimate the strain rate at a specific temperature with a given cooling rate ($-\dot{T}$), use the value from Figure 20 for the temperature and multiply by the cooling rate. For example, if a brine cell is presently at -3 °C and is cooling at a rate of 2 °C per day, the approximate volumetric strain rate ($\dot{e}_T^B$)

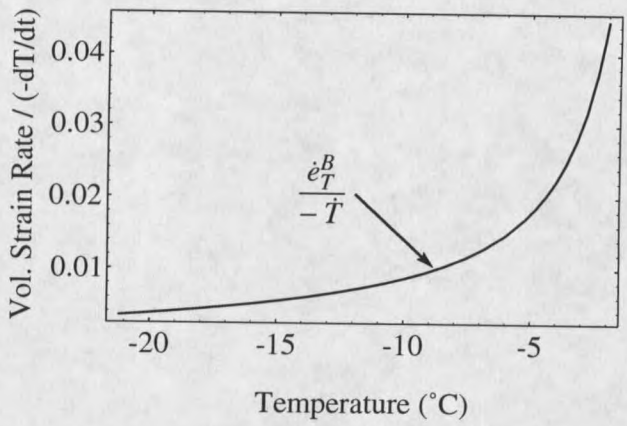

Figure 20. Volumetric Strain Rates for Varied Temperature Rates

is $0.018 * 2 = 0.036$ day^{-1}. In other words, Figure 20 represents volumetric strain rates for cooling rates of 1 °C s^{-1}, 1 °C hr^{-1}, 1 °C day^{-1}, etc. Notice the strain rates decrease significantly at lower temperatures.

In finite difference form, the volumetric strain rate can be approximated by

$$\frac{\dot{V}^O}{V^B} \approx e_T^B(s_i^B, s_{i-1}^B)\frac{\Delta s^B}{\Delta t}, \tag{3.92}$$

where

$$\Delta s^B = s_i^B - s_{i-1}^B \qquad \text{and} \qquad \Delta t = t_i - t_{i-1}.$$

and each salinity state (s_i^B) is defined by the temperature, Equation (3.2), at the corresponding time (t_i).

Solution Techniques

Three separate techniques will be considered for obtaining an approximate solution to the differential constitutive equation (3.63). The first technique will be referred to as a solution because it yields a numerical solution to the original differential equation with out neglecting the elastic component of the stress field. Both of the other two techniques neglect the role of the elastic components in the stress field.

Because they include this additional assumption, the results of these two techniques will be considered approximations, though all three techniques are approximations in one sense or another.

Finite Element Solution

With the finite element model, it is not necessary to assume that the stress-pressure relationships are defined by the flow stress (i.e., viscous component of deformation as given in Equations (3.79) and (3.80)). Instead, with the finite element technique, the stress distribution can be left undefined initially, as in Equation (3.63). By assuming a Prandtl-Reuss constitutive model and a relationship between the equivalent plastic strain-rate and stress, numerical techniques can be used to converge to an equilibrium solution that combines the elastic and inelastic components of deformation at each time step.

Finite Difference Approximation

As an alternative to the finite element solution, consider the pressure-differential constitutive equation (3.83). Unless the stress exponent (n) is 1, the nonlinear nature of this differential equation implies that the solution (pressure function) must be resolved numerically. Using a forward difference scheme, the differential equation can be represented in finite difference form by

$$(P_i^B - P_{i-1}^B) + \Delta t \mathcal{M}\mathcal{N}(P_{i-1}^B)^n = \mathcal{M}\Delta e_T^B, \tag{3.93}$$

where the subscript i indexes the end of a time step and $i-1$ indexes the end of the previous time step. Solving for the pressure at the end of the time step (P_i^B) implies

$$P_i^B = P_{i-1}^B + \mathcal{M}\Delta e_T^B - \Delta t \mathcal{M}\mathcal{N}(P_{i-1}^B)^n \tag{3.94}$$

or, in terms of salinity,

$$P_i^B = P_{i-1}^B + \mathcal{M} e_T^B(s_i^B, s_{i-1}^B) - \Delta t \mathcal{M}\mathcal{N}(P_{i-1}^B)^n, \tag{3.95}$$

where the salinity for state i is related to the temperature for state i by $s_i^B = s^B(T_i)$, Equation (3.2). To integrate these difference forms numerically, the Runge-Kutta technique was used.[20]

Flow Approximation

To place an upper bound on the brine pressure (P^B), it is possible to further simplify the pressure-differential constitutive equation (3.83) and completely neglect the elastic components and assume that all stress induced deformation is due the the viscous flow of the ice. In this case, the brine pressure can be approximated by

$$P_{ub}^B = \left\{ \frac{\dot{e}_T^B}{\mathcal{N}} \right\}^{1/n}. \tag{3.96}$$

This approximation considers only secondary creep and does not model any form of primary creep.

Example

Material Parameters To define the elastic components for the parameter $\mathcal{M}$, defined in Equation (3.84), suppose the bulk modulus for the brine (K^B) is equal to 2.0 GPa, the elastic modulus for the ice (E^I) is equal to 9.41 GPa and Poisson's ratio (ν^I) for the ice is equal to 0.308 (Derradji-Aouat 1992, Table 4.3).

To define the flow parameters for the power-law model, consider the relation developed by Goodman, Frost & Ashby (1981) based on creep measurements. With

[20] For the Runge-Kutta approximation,

$$P_i^B = P_{i-1}^B + \mathcal{M}\left(\tilde{e}_T^B(T_i) - \tilde{e}_T^B(T_{i-1})\right) - \frac{\Delta t}{6}(A_{i-1} + 2B_{i-1} + 2C_{i-1} + D_{i-1}),$$

where

$$A_{i-1} = \mathcal{M}\mathcal{N}_i(P_{i-1}^B)^n \qquad B_{i-1} = \mathcal{M}\mathcal{N}_{i+1/2}(P_{i-1}^B + A_{i-1}/2)^n$$
$$C_{i-1} = \mathcal{M}\mathcal{N}_{i+1/2}(P_{i-1}^B + B_{i-1}/2)^n \qquad D_{i-1} = \mathcal{M}\mathcal{N}_i(P_{i-1}^B + C_{i-1})^n.$$

this model, the Arrhenius parameter (B), defined in Equation (3.66), takes the form

$$B = \frac{\tilde{A}}{\mu^n} \exp\left(\frac{-\Delta F_g}{kT}\right), \tag{3.97}$$

where

$\tilde{A} = 2.133 \times 10^{17}$ s^{-1} $\quad$ $\Delta F_g = 1.290 \times 10^{-19}$ J molecule^{-1}
$\mu = 2.910 \times 10^{9}$ Pa $\quad$ $k = 1.381 \times 10^{-23}$ J molecule^{-1} K^{-1}
$n = 3$ $\quad$ T = Absolute Temperature (K).

This also completes the definition of the flow parameter $\mathcal{N}$, Equation (3.85).

Transformation Strain As a case study, a piecewise linear model will be used for the temperature history of a brine cell. As shown in Figure 21, the history begins with an initial stress-free temperature of $-2\,^{\circ}$C and cools over a 48 hour period to a final temperature of $-3\,^{\circ}$C. This cooling stage is then followed by a 48 hour period where the temperature is held constant at $-3\,^{\circ}$C. The corresponding volumetric strain profile is also shown in Figure 21.

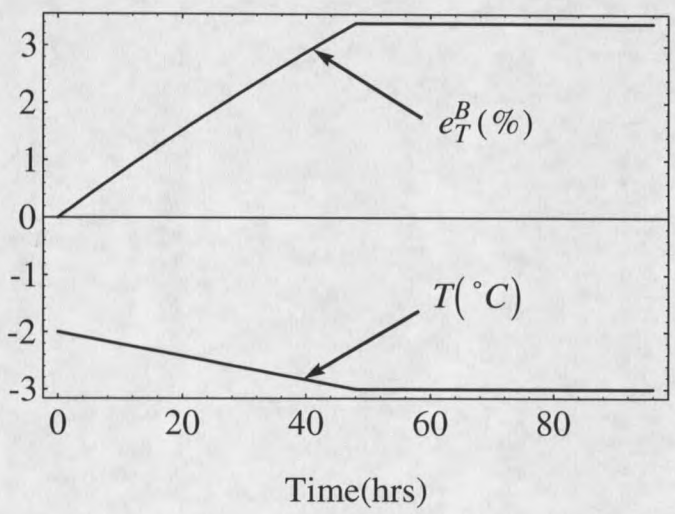

Figure 21. Temperature and corresponding volumetric-transformation strain

This temperature/transformation-strain profile (Figure 21) will provide comparisons of the brine pressure profiles resulting from the different inelastic models (i.e.

finite element, finite difference, and flow).

Inelastic Response In the plots that follow, the output of the finite element (FE) model is displayed using dashed curves. The output of the finite difference (FD) approximation is displayed using solid curves, and the output of the corresponding flow approximation is displayed using dotted curves.

For the finite element solution, curves based on brine stress estimates at the interface will be illustrated using thick dashed lines while curves based on ice stress estimates at the interface will be illustrated using thin dashed lines. For a non-linear analysis, such as creep or flow, ANSYS simply copies data from the nearest integration point to the node of interest (i.e. at the interface) and does not extrapolate. Therefore, a relatively fine grid was used so that the nearest integration points would lie sufficiently close to the interface. Values taken from the brine side of the interface, which is in a hydrostatic state of stress, are spatially constant so that accurate approximations can be obtained at the integration points without extrapolating to the interface. Unfortunately, this only yields the radial stress component for ice at the interface. Radial stresses taken from both sides of the interface were plotted to demonstrate that data taken from both sides of the interface were in agreement, indicating that the interpolation errors are minimal.

The transformation strain profile in Figure 21 resulted in the responses shown in Figure 22. Most of these responses are from the finite element version of the model.

In Figure 22a, the tangential component of the transformation strain ($(e_T^B)_t$) is graphed along with the non-dimensional radial displacement of the interface ($\epsilon_t = u/r^i$). Comparing u/r^i with $(e_T^B)_t$, it is clear that the brine compresses very little as the model brine cell expands isotropically, driving the interface outward. This driving behavior results from the relatively incompressible nature of the elastic brine model

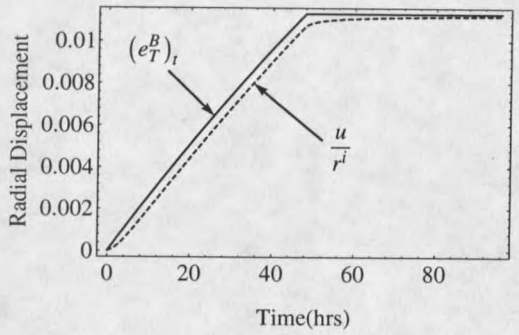

(a) Radial displacement with $(\epsilon_T^B)_t$

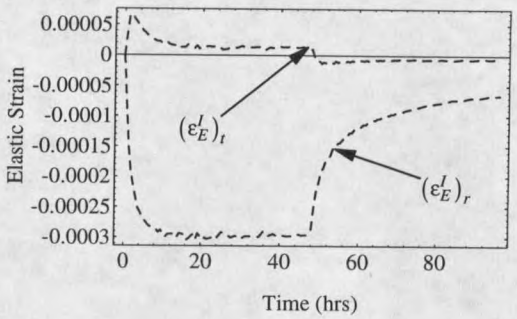

(b) Elastic Strain Components

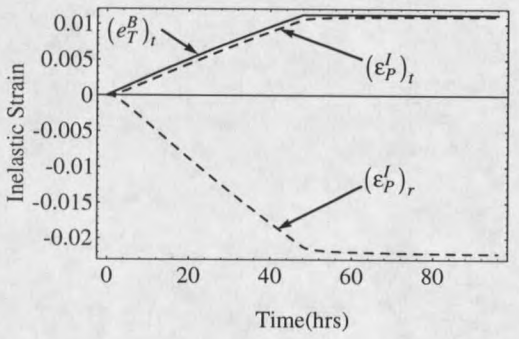

(c) Inelastic strain components with $(\epsilon_T^B)_t$

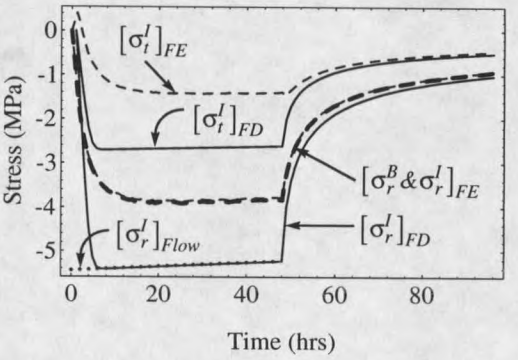

(d) Stress Components

Figure 22. Interface responses for the spherical brine cell model

combined with the yielding nature of the ice model which "flows" at comparatively low stresses.

As displayed in Figure 22b and Figure 22c, the finite element solution starts off with a typical elastic type response, as the tangential component of the elastic strain goes into a tensile mode; however, once the stresses reach a sufficient level, inelastic deformation dominates and allows the elastic tensile component to "relax".

In Figure 22d, the stress responses are compared for the different solutions to the model. The top dashed and solid curves are estimates for the tangential stress component (σ_t) at the brine ice interface based on the finite element (FE) solution and finite difference (FD) approximation, respectively. All four of the lower curves are estimates of the radial stress (σ_r) at the interface, which is the negative of the brine

pressure (P^B). Of these four, the two dashed curves are based on the finite element version. The thicker dashed curve is taken from the brine side of the interface and is considered the more accurate of the two; the thinner dashed curve is taken from the ice side of the interface demonstrates relatively good agreement with the same component taken from the brine side of the interface. The solid curve at the bottom is based on the finite difference version and the corresponding dotted curve is based on the flow version.

Observe the discrepancy between the stress estimates from the finite element solution and the other two approximations in Figure 22d. These differences result from the lack of an elastic effect in the stress distribution of the finite difference and flow approximations. Notice how the curves of the finite element and finite difference models converge (Figure 22d) when the temperature is held constant and the elastic strains relax, Figure 22b. While the model is in a state of "flow", the finite difference and flow models overestimate the magnitude of the radial stress component by nearly forty percent and the tangential component by ninety percent.

Though the estimates of the stress components don't match very well, the equivalent stress estimates at the interface show relatively good agreement, Figure 23. In this case the finite difference and flow models overestimate the magnitude of the equivalent flow stress by less than nine percent.

In light of this reduced difference, recall that, in the model, the equivalent stress defines the level of flow. The elastic part of the strain field (Figure 22b), serves to increase the equivalent stress (i.e., the difference between radial and tangential stress components). As a result, flow can occur at lower component magnitudes as it does in the FE solution, which includes the elastic part. This assertion implies that the neglect of the elastic component introduces error in the equivalent stress and this error then propagates into the resulting estimates for the stress components and

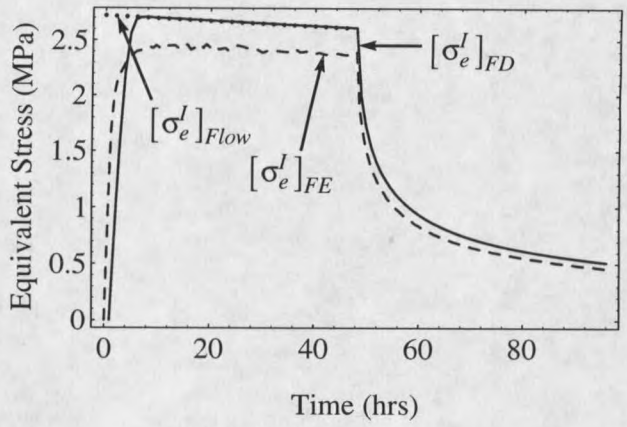

Figure 23. Equivalent Stress in the Ice at the Interface

brine pressure. Thus, it appears, that the flow assumption yields a more reasonable estimate for the equivalent stress than for the principal stress components, where the errors are magnified.

To substantiate the belief that the discrepancy in the magnitude of the stress components resulted from the flow assumption used to derive the equivalent stress expression (3.81), a model uniaxial specimen was compressed with a constant displacement rate and then held with a fixed displacement. The stress responses were modeled using finite difference and FE models that were equivalent to those developed for the spherical brine cell. The stress responses matched so well that the different curves were barely distinguishable. The primary distinction between the spherical brine cell model and the uniaxial specimen model was that the flow assumption was not used for the uniaxial finite difference version because the equivalent stress was fully defined by the uniaxial stress.

Discussion

The brine cell model developed in this paper gives us a tool for estimating the inelastic deformation that might occur in the neighborhood of a brine cell. Of the three solutions to the spherical brine cell model considered, the flow and the finite difference

approximations provide us with insight into the assumptions required and some of their consequences. In addition, these two approximations serve to provide upper bounds for the magnitude of the stress components (σ_r and σ_t) at the interface and the brine pressure (P^B), and they are useful for estimating the significance of yielding at the interface based on the magnitude of the equivalent stress (σ_e). The equivalent stress distribution (3.81) may be modeled as a function of the brine pressure estimate (P^B) taken from the finite difference or flow approximations.

In this model, the delayed elastic component of deformation that allows for time-dependent relaxation of the elastic parameters has been neglected. For polycrystalline ice, Sinha (1979) indicates that the delayed elastic response is primarily due grain boundary sliding mechanisms. Others (Vassoille, Mai & Perez 1978, Cole 1995) have modeled the delayed elastic response in terms of dislocation mechanisms. To increase the accuracy of the model, it appears it would be useful to include at least those delayed elastic components due to dislocation-related mechanisms. Unfortunately, for monocrystalline ice there does not appear to be any existing models for the delayed elastic component. The best data on single crystals seems to be that recorded by Gold (1958, Fig. 3), based on a load that was ramped to 10 kg/cm^2 ($\approx$ 1 MPa) over 5 seconds and then held constant at this stress for another 5 seconds before the load was released. In the physical case, the effective elastic modulus would vary over time between the dynamic value (9.41 MPa) and the relaxed value (8.34 MPa) and could possibly drop slightly lower than this relaxed value. To determine the significance of the delayed elastic component, the same model was evaluated using Gold's effective elastic modulus. When the models using the two different elastic parameters were compared, the difference in the responses could not be distinguished when the model was in a "flow" state, only during the initial transient was there a slight distinction in the responses of the two models. As a result of this comparison, the anelastic

component was deemed relatively insignificant for this model.

The accuracy of all three solutions of the brine cell model proposed here is dependent on the accuracy of the Prandtl-Reuss constitutive model combined with the assumption that the equivalent plastic strain rate can be modeled with a power-law dependence on equivalent stress and an Arrhenius type dependence on temperature, Equation (3.64). In particular, the isotropic nature of this model does not characterize the anisotropic inelastic deformation that would occur in the neighborhood of a brine cell.

Application of the Inelastic Model

Using the previously developed brine cell model, the next step is to determine how different temperatures and cooling rates might alter the macroscopic behavior of saline (sea) ice. If cooling rates are sufficiently slow the phase transformation mechanism can compel the neighboring ice to deform inelastically, leading to the introduction of a large mobile dislocation density. If a brine cell cools sufficiently fast, the cell wall will crack; these local "micro"-cracks can nucleate dislocations at their tips or provide for other modes of deformation. For the present, the boundary between these two local stress relief mechanisms will be represented with relatively simple criteria.

Criteria for Local Crack Formation

In conjunction with the relative simplicity of the brine cell model, two relatively simple criteria will be used to imply the formation of local micro-cracks.

The first criterion will be based on the experimental results of Visagie (1969), who recorded pressures inside water drops as they froze from the outside in. During the initial freezing process, Visagie reported that once shells of ice encased the droplets, the internal pressure would quickly rise to approximately 2 MPa where the

shells would crack and allow a small amount of leakage (expulsion). Then the cracks would re-seal and the pressures would rise again. As the thickness of the ice shell increased, the cracking pressure would increase. Using drops with outside diameters on the order of 7 mm, Visagie recorded inner pressures as high as 7.6 MPa before the outside shell would crack and relieve the pressure.

For brine cell geometry, Anderson & Weeks (1958) recorded initial cell diameters on the order of 0.07 mm with platelet thicknesses on the order of 0.46 mm and a diametral spacing between cells on the order of 0.23 mm If the structural effect of salt precipitates is neglected, it is reasonable to assume that the structural nature of the ice surrounding a brine cell is similar to that of the ice shells tested by Visagie. Therefore, for "thick" cell walls, pressures are likely to climb as high as 7.6 MPa before micro-cracks develop. Similarly for "thin" cell walls, pressure as low as 2 MPa are likely to nucleate micro-cracks. However, because the pressure estimates are based on the assumption that the cell walls are "thick", this lower bound will be rather unreliable.

As a second criterion, assuming the ice surrounding a brine cell maintains a single crystalline nature, an upper bound of 2 MPa will be used for shear stress on the basal plane (Wakahama 1966), corresponding to an equivalent shear stress of 4 MPa. Wakahama implies that fracture occurs at a basal plane shear stress of 2 MPa induced by uniaxial stresses both in tension and compression. Again, because the brine cell model assumes "thick" cell walls, the basal plane shear stress criterion will be most accurate for brine cells with "thick" cell walls.

If this second criterion is compared with the deformation mechanism map constructed by Duval, Ashby & Anderman (1983, Fig. 1), the criteria corresponds to the lower bound for cleavage fracture in polycrystalline ice for a uniaxial tensile load. Duval *et.al.* point out that for increased accuracy, stress-based fracture models must

be based on all three invariants of the stress tensor. In particular, the fracture stress is quite dependent on the hydrostatic stress (Rist & Murrell 1994, Rist, Jones & Slade 1994). In the case modeled here, the hydrostatic stress is relatively small; therefore, this stress criterion, based on the second invariant, will serve as a first approximation with the recognition that it serves as a rough lower bound for fracture.

Relevance to Sea Ice

As Cox and Weeks (1975) point out, the phase transformations for brine in sea ice and saline (NaCl) ice are similar at temperatures above $-8.2\,^{\circ}\mathrm{C}$. At temperatures below $-8.2\,^{\circ}\mathrm{C}$, solid salt ($Na_2SO_4{\cdot}10H_2O$) begins to precipitate out of the brine in sea ice and, according to Peyton (1966, §6.2.2), merge with the precipitating ice to form an inner shell of "salty" ice. For uniaxial specimens, Peyton concluded that the solid salts did not significantly alter the tensile behavior, but that they did have a stiffening effect on the compressive behavior. Slightly in contradiction to Peyton's conclusions, Sinha (1977), using a scanning electron microscope, observed that solid salt crystals were only loosely attached to the sides of the brine cell indicating that the solid salts were not incorporated into the ice surrounding a brine cell. If, as these observations suggest, the solid salts increase the strength on the brine planes by increasing the friction between platelets under compression, then the precipitation of solid salts will not significantly alter the structural response that is being modeled, as the solid salts will continue to "float freely" in the brine cell. If solid salts are incorporated in the ice, the structural model will lack accuracy for temperatures below $-8.2\,^{\circ}\mathrm{C}$.

Likewise, if solid salts are not incorporated in the ice, the interference strain estimate (e_T^B) should be reasonably accurate; except that it does not include the volume change due to the additional phase transformation. By using the NaCl phase curve, the volume that precipitates as ice (H_2O) is "isolated" , in an approximate

fashion. If solid salts are incorporated into the ice shell, it would be more accurate to estimate the interference strain (e_T^B), due to the multiple phase transformations, from the phase curve for sea ice (Assur 1958, Fig. 6).

In summary, the model assumes that incorporation of the solid salt ($Na_2SO_4 \cdot 10H_2O$) in the ice matrix is minimal. If this assumption holds true, the model should be reasonably accurate for sea ice as well as NaCl ice; otherwise, at temperatures below -8.2 °C, the model will become increasingly inaccurate for sea ice.

Gas Inclusions

Notice the model does not include the effects of gas that will be coincidentally trapped along with the brine. When the brine is sealed in a cell, it will contain a certain amount of dissolved gas. As ice precipitates from the brine, the gas and salt in the brine will remain relatively constant. Hence, the remaining brine will become increasingly saturated with gas. At the same time, the remaining brine will become increasingly salty and increasing brine salinity results in decreasing gas solubility in the brine, sometimes referred to as "salting-out"[21]. To counter these two factors, both the brine pressure increase and the temperature decrease which occur coincidentally with the reduction in brine volume will each increase the gas solubility. In the situation modeled, the dissolved gas may never nucleate a bubble.

Whether a bubble forms or not, consider the amount of gas that might coexist in a brine cell. As a rough upper bound for the dissolved gas, consider the closest solubility data provided by Weiss (1970). This data is for sea water with a salinity of 0.035 and at a temperature of -1 °C. In this case, the sum of the solubilities of N_2, O_2, and Ar yield a gas solubility of 0.02326 *(l of gas)/(l of brine)*; so, up to 2.3% of

[21]To illustrate the "salting-out" effect, consider data provided by Weiss (1970). For distilled water at 0 °C the sum of the solubilities of N_2, O_2, and Ar is 0.02914 *(l of gas)/(l of brine)*. Compare this case with that of sea water at a temperature of 0 °C and a salinity of 0.035 for which the summed solubility of the same components is 0.02235 *(l of gas)/(l of brine)*.

the original cell volume might be occupied by dissolved gas. At the same time, it is possible that a bubble will float up from below and enter the cell before it is sealed off. In summary, the volume occupied by gas in a brine cell is likely to vary anywhere between 1 and 100%.

The more gas there is in the cell, whether dissolved or in bubble form, the less brine there is available to transform to ice; therefore, the less the cell contents will expand relative to their initial size. Coincidentally, the gas in the cell will compress much more readily, so that the pressure generated will be significantly reduced. As a lower bound, a cell filled completely with gas will generate virtually no internal stress; the model therefore gives an upper bound for brine cells containing gas.

The role that bubbles play in the transformation process is also dependent on the directional nature of the freezing process. Nakaya (1956, Plate 44), in his study of internal melt figures, demonstrated that typically when freezing is "isotropic", the vapor bubble will shrink in size as the water/ice transformation progresses. In the case of bubbles generated by internal melt, the bubble will eventually vanish. If the freezing process is orthotropic, in particular if the rate of freezing is faster from the top down, the buoyancy of a bubble will typically result in its isolation as the precipitating ice freezes around it (Nakaya 1956, Plate 45-47). Once a bubble has been isolated, the model proposed in this paper provides an approximation for the strain and pressure build up, though with altered initial conditions.

Constitutive Assumptions

The inelastic flow model (Goodman et al. 1981) used previously is based on creep data from polycrystalline ice. If the case where a brine cell is sealed in the ice matrix is considered, the ice surrounding the brine cell is likely to be of a monocrystalline nature. Therefore, it appears that the proper constitutive model should be based on

data from single crystals. However, due the localized nature of the load induced by brine cell phase transformations, slip on the basal plane will be severely limited by material constraints of the surrounding ice.

To maintain constant volume, arbitrary deformation of crystals requires slip in at least five independent directions (von Mises 1928, Taylor 1938) and for crystals with hexagonal symmetry, such deformation might occur with a minimum of four independent slip directions (Hutchinson 1977). Based on this argument, deformation of polycrystalline ice requires each grain to slip in at least four independent directions. By the same argument, local deformation in the neighborhood of a brine cell must satisfy the same requirements. Because there are only two independent slip directions on the basal plane in ice, at least two non-basal components will be necessary for deformation to take place. Though basal slip may provide a significant percentage of the deformation, the rate of deformation in the neighborhood of the brine cell will be limited overall by the more resistant non-basal components of deformation (i.e., slip or climb).

Constitutive equations for deformation of single crystals of ice are typically defined in terms of basal plane slip, which dominates as long as there is shear stress on the basal plane. If single crystals are loaded such that there is no shear stress on the basal plane, then non-basal deformation takes place and the stress required for deformation increases by as much as a factor of 60. In either case, the constitutive equations for single crystals typically model basal and non-basal components of deformation independently.

As a brine cell expands, the stress in ice near the brine cell will develop in a three dimensional fashion due to material constraints. To model the three dimensional stress state, a constitutive model derived from polycrystalline ice will serve as a more accurate representation than one derived for planar slip in monocrystalline

ice. To clarify the need for a constitutive equation based on polycrystalline data, for deformation in the neighborhood of a brine cell, consider the similarity between the nature of deformation in the neighborhood of a pressurized brine cell and local deformation from an indenter in a hardness test. In both cases, basal slip is constrained by the surrounding material so that non-basal components of deformation must be mobilized before extensive inelastic deformation can develop. Because hardness data compares well with other forms of polycrystalline data (Goodman et al. 1981, Fig. 4), it is fair to assume that the use of a polycrystalline based model is reasonable.

At temperatures above $-10\,^{\circ}\mathrm{C}$, polycrystalline creep accelerates faster than would be expected based on data below $-10\,^{\circ}\mathrm{C}$ (Duval et al. 1983). This relative acceleration, commonly attributed to grain boundary effects (such as melting), is not observed in single crystals. As a result, the Goodman et al. (1981) model will be used in its unmodified form at temperatures up to the melting point, assuming grain boundary type effects will be minimal in the deformation of a brine cell wall. This model can be expressed in the following extended form (Frost & Ashby 1982, §16.1):

$$\dot{\epsilon}_e^p = \begin{cases} B\sigma_e^n & \text{if } \mathcal{F}(\sigma_e) \leq 1 \\ B\sigma_e^n \mathcal{F} & \text{if } \mathcal{F}(\sigma_e) > 1 \end{cases} \tag{3.98}$$

where the extension factor ($\mathcal{F}$) is expressed by

$$\mathcal{F}(\sigma_e) = \left(\frac{\sqrt{3}kT}{2.5b^3\sigma_e(1-\sigma_e/(\sqrt{3}\tau_G))} \right)^{\frac{1}{2}} \exp\left\{ \frac{\Delta F_k}{kT} \left(\frac{\sigma_e}{\sqrt{3}\tau_o} \right)^{\frac{1}{2}} - 0.06 \left(\frac{\sqrt{3}\mu}{\sigma_e} \right)^{\frac{1}{2}} \right\} \tag{3.99}$$

and in addition to the parameters defined previously (3.97),

$$b = 4.52 \times 10^{-10}\ \mathrm{m} \qquad \tau_G = 0.1\mu$$
$$\Delta F_k = 0.15\mu b^3 \qquad \tau_o = 0.09\mu$$

This extended power law (3.98) is based on secondary creep and hardness data which, in the case of ice, refers to the minimum strain rate. Mellor & Cole (1982) recorded data from uniaxial constant load (CL) and constant displacement

(CD) rate experiments for isotropic polycrystalline ice at $-5\,^{\circ}\mathrm{C}$. Based on these experimental records, Mellor & Cole (1983) demonstrated that there was a strong correlation between key points abstracted from the response of both load cases (CD and CL). Of particular interest, Mellor and Cole defined a stiffness rate parameter by the ratio of the stress (σ) to a power (n) divided by the strain-rate ($\dot{\epsilon}$) and showed that:

$$\underbrace{\frac{\sigma_{const}^{n}}{\dot{\epsilon}_{min}}}_{CL} \approx \underbrace{\frac{\sigma_{max}^{n}}{\dot{\epsilon}_{const}}}_{CD} \tag{3.100}$$

Because the load cases considered here are better represented by the constant displacement (CD) rate experiments than the constant load (CL) experiments, the flow-law can be represented by

$$\dot{\epsilon}_{const} \approx \underbrace{\frac{\dot{\epsilon}_{min}}{\sigma_{const}^{n}}}_{CL} \sigma_{max}^{n} = B\sigma_{max}^{n} \tag{3.101}$$

More specifically, because the boundary conditions are defined in terms of transformation strains, the flow stress response for the model can be represented by

$$\sigma_{max} \approx \left(B^{-1}\dot{\epsilon}_{const}\right)^{1/n} \tag{3.102}$$

In the inelastic deformation of polycrystalline ice and in the case being modeled, the internal structure undergoes constant modification (changes in dislocation density, recrystallization, etc.). In this model, the internal structure is essentially assumed to maintain a steady state, represented by the internal state near the maximum flow stress (Equation 3.102); because this is not the case, this component of the flow model will in general over estimate the stress-pressure response. However, in polycrystalline ice under a constant displacement rate, this maximum stress state occurs at strains on the order of 1%. Because most of the strains modeled here are on the order of 1%, it will be assumed that this simple model serves as a reasonable representation of the inelastic deformation of ice in the neighborhood of a brine cell.

Allowable Cooling Rates

As demonstrated earlier, it is reasonable to estimate the equivalent shear stress under flow conditions using the flow approximation. Using the original differential equation (3.63) and neglecting the elastic component yields

$$\frac{3}{2}\dot{e}_e^p = \dot{e}_T^B. \tag{3.103}$$

If the basal plane shear stress (σ_{xz}) criterion is used to indicate the onset of micro-cracking, for the spherical brine cell model,

$$(\sigma_{xz})_{max} = \frac{\sigma_1 - \sigma_3}{2} = \frac{\sigma_e}{2}. \tag{3.104}$$

Assuming the maximum basal plane shear stress ($(\sigma_{xz})_{max}$) to be 2 MPa, corresponding to an equivalent shear stress of 4 MPa, the inelastic strain rate ($\dot{e}_e^p$) can still represented reasonably well by the power-law (3.64). At the same time, the volumetric strain rate can be expressed as a function of the cooling rate, Equation (3.91). Using these substitutions and solving for the cooling rate implies

$$\dot{T}(T) = 12B(\sigma_{xz})_{max}^n \left(\frac{de_T^B}{ds^B}\frac{ds^B}{dT}\right)^{-1}. \tag{3.105}$$

This relationship provides an estimate for the temperature dependence of the onset of cracking for a thick walled brine cell. The thermal dependence of this vague boundary between the deformation modes, as defined by this simple model, is displayed in Figure 24.

Initially as temperatures drop below -2 °C, the allowable cooling rate increases as the corresponding expansion rate decreases, Figure 20. As temperatures drop below -8 °C, the allowable cooling rate declines as the surrounding ice begins to "stiffen" up. Given the significant change in the structural behavior over this temperature range the basal plane failure stress ($(\sigma_{xz})_{max}$) should more realistically be expressed

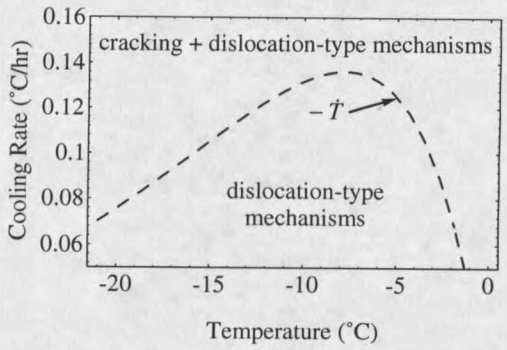

Figure 24. Critical stress as a function of temperature (T) and cooling rate ($-\dot{T}$). Cooling rates above the dashed curve are likely to result in cracking and the associated inelastic deformation. Cooling rates below the curve are more likely to result in general inelastic deformation without cracking.

as a function of temperature. However, this estimate at least gives us an order of magnitude estimate for determining the probable role that the phase transformation mechanism can play in modifying the compliance of saline (sea) ice. In other words, if the cooling rate is much greater than 0.1 °C per hour, then the mechanism is likely to introduce micro-cracks and a low level of associated dislocation nucleation and motion. For cooling rates significantly below 0.1 °C hr^{-1}, the mechanism is likely to provide the energy for a high level of dislocation nucleation and motion and for cooling rates near 0.1 °C hr^{-1}, responses are likely to be mixed.

Thermal Variations

Using the spherical brine cell model, it is possible to estimate those cooling rates that have the potential to generate dislocations and those that have the potential to generate micro-cracks. The next question is: What kind of cooling rates do brine cells in saline (sea) ice normally experience.

For Lab Specimens

To evaluate the effects of the temperature variations in a lab specimen, consider a Bessel function solution to the heat equation for cylindrical specimens as given by

Pounder (1960, Eq.6).

$$T(r,t) = T_f + (T_i - T_f) \sum_{n=1}^{\infty} \frac{2}{a_n J_1(a_n)} \left[J_0 \left(a_n \frac{r}{r_s} \right) \right] \exp \left(\frac{-a_n^2 K t}{r_s^2} \right) \tag{3.106}$$

where r is the radius from the center, r_s is the radius of the specimen, K is the diffusivity, T_i is the initial temperature of the specimen, and T_f is the final surface temperature. This solution is based on the assumption that the diffusivity (K) can be modeled as a constant and that the temperature change at the surface of the specimen, i.e., T_i to T_f, occurred as a step function at time (t) equal zero.

Using this expression for the temperature, a non-dimensional temperature change can be defined by

$$\theta(r^*,t) = \frac{T(r,t) - T_i}{T_f - T_i} \tag{3.107}$$

$$= 1 - \sum_{n=1}^{\infty} \frac{2}{a_n J_1(a_n)} \left[J_0 \left(a_n r^* \right) \right] \exp \left(\frac{-a_n^2 K t}{r_s^2} \right) \tag{3.108}$$

where $r^* = r/r_s$, then the non-dimensional rate of temperature change takes the form:

$$\frac{\partial \theta(r^*,t)}{\partial t} = \sum_{n=1}^{\infty} \frac{-a_n^2 K 2}{r_s^2 a_n J_1(a_n)} \left[J_0 \left(a_n r^* \right) \right] \exp \left(\frac{-a_n^2 K t}{r_s^2} \right) \tag{3.109}$$

For a saline ice specimen with a bulk salinity of 0.006 at a temperature of -5 °C, the diffusivity (K) takes a value near 3.34×10^{-3} cm^2 s^{-1} (Weeks & Ackley 1982, Fig. 89). Consider the temperature variations as they progress into a specimen with a radius (r_s) of 3.75 cm, Figure 25.

This model assumes an instantaneous change in temperature at the surface of the specimen. In Figure 25a, it is clear that any temperature change imposed at the surface will reach the center of the specimen in less than an hour. Figure 25b, displays the dampening nature of the outer layer of ice. Since cooling rates greater than .1 °C per hour are likely to induce micro-cracking, it is clear that the brine cell mechanism will induce internal micro-cracking unless the surface of a specimen is cooled very slowly.

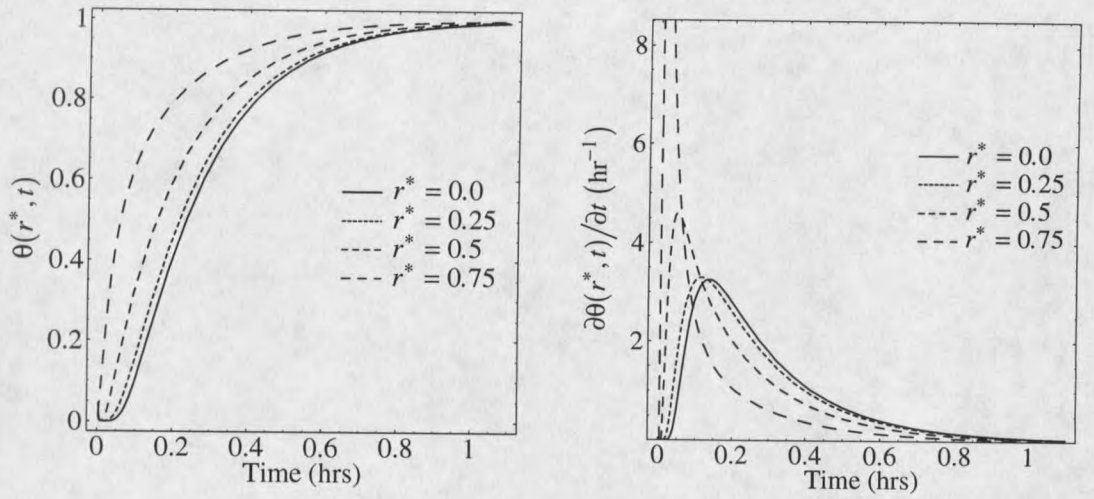

(a) Relative temperature change (b) Rate of temperature change

Figure 25. Relative temperature variations in a 7.5 cm cylindrical specimen.

For Sea Ice (*in situ*)

To understand the significance of the role played by the thickness of an ice sheet and the thermal mass of underlying sea water, a sheet of sea ice can be treated as an infinite slab with isothermal upper and lower surfaces. With these assumptions, the heat transfer through the sheet can be modeled with the 1-D heat equation. For sea ice, it is reasonable to assume that the temperature of the bottom surface is constant and for a relatively short period of time that the thickness (h) is constant. If in addition, the diffusivity (K) is assumed constant, a closed form solution can be obtained. Pounder (1965, Eq.59) provides the following Fourier series solution for such a model, i.e.,

$$\mathcal{T}(z,t) = \mathcal{T}_f \frac{z}{h} + (\mathcal{T}_i - \mathcal{T}_f) \sum_{n=1}^{\infty} (-1)^{n+1} \frac{2}{n\pi} \exp\left(-n^2\pi^2 \frac{Kt}{h^2}\right) \sin\left(\frac{n\pi z}{h}\right), \quad (3.110)$$

where, at time t after a temperature change at the top surface, $\mathcal{T}$ is the difference between the temperature at a distance z from the bottom surface and the temperature at the bottom surface. Then $\mathcal{T}_i$ is the difference between the initial surface temperature and the temperature at the bottom, and $\mathcal{T}_f$ is the difference between

the final surface temperature and the temperature at the bottom. This solution is based on the assumption that the temperature change at the surface, i.e., $\mathcal{T}_i$ to $\mathcal{T}_f$, occurred as a step function at time (t) equal zero.

Using this expression for the temperature, a non-dimensional temperature change can be defined by

$$\theta(z^*,t) = \frac{\mathcal{T}(z,t) - \mathcal{T}_i z/h}{\mathcal{T}_f - \mathcal{T}_i} \tag{3.111}$$

$$= z^* + \sum_{n=1}^{\infty}(-1)^n \frac{2}{n\pi} \exp\left(-n^2\pi^2 \frac{Kt}{h^2}\right) \sin(n\pi z^*) \tag{3.112}$$

where $z^* = z/h$. Then the corresponding rate of non-dimensional temperature change takes the form:

$$\frac{\partial\theta(z^*,t)}{\partial t} = \sum_{n=1}^{\infty}(-1)^{n+1} \frac{2n\pi K}{h^2} \exp\left(-n^2\pi^2 \frac{Kt}{h^2}\right) \sin(n\pi z^*) \tag{3.113}$$

For the diffusivity (K), a value of 3.34×10^{-3} $cm^2\ s^{-1}$, given in Pounder (1965) will be used. Consider the temperature profiles in Figure 26a, which demonstrate how an instantaneous temperature change at the surface is relayed down through a 1 m homogeneous slab with a diffusivity similar to that of ice. Figure 26b displays the corresponding cooling rates. Notice the significant lag in the rate of cooling for points near the bottom compared to the "instantaneous" change that was assumed at the surface.

For the time dependent temperature model (3.112, 3.113), consider the relationship between the parameters for time (t), diffusivity (K), and the thickness of the ice (h). If the diffusivity is held constant and the thickness is doubled, the argument of the exponential function is reduced by a factor of four. This reduction implies that it will take four times as long to reach a steady state value. Coincidentally, for the same relative positions (z^*) in the homogeneous slabs, the magnitude of the cooling rate (3.113) drops by a factor of four in the thicker slab. If the diffusivity is allowed

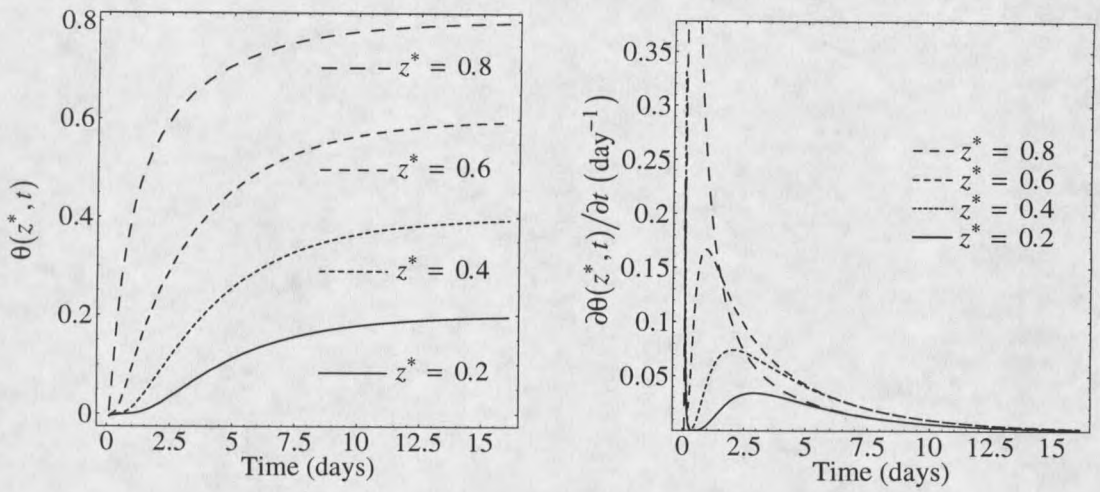

(a) Relative temperature changes (b) Rate of temperature change

Figure 26. Relative temperature variations through a 1 m ice sheet.

to vary, the variations in the responses will be similar. If the diffusivity increases the rate of cooling increases by a like order of magnitude.

Diffusivity

As Pounder (1965) points out, in the case of sea ice, the assumption that the diffusivity is constant is not very accurate. Diffusivity is defined as

$$K = \frac{k}{C\rho} \tag{3.114}$$

where k is the conductivity, C is the specific heat, and ρ is the density. For sea ice, Schwerdtfeger (1963) demonstrates that, for a given macro-scale salinity (S^I),[22] all three of these parameters are monotonic functions of temperature. As temperature

[22]The *macro-scale salinity* of sea ice (S^I) can be defined by

$$S^I = \frac{m^S}{m^S + m^I + m^W}$$

averaged over a local volume that is large relative to the size of the brine cells but small relative to the thickness of the ice sheet. Here m^S, m^I, and m^W represent the mass of salt, ice, and water, respectively. Notice that, at a spatial point, the macro-scale salinity remains constant relative to phase changes and hence temperature changes, but will vary due to brine drainage mechanisms.

rises, the conductivity decreases while the heat capacity and the density increase. As a result, the diffusivity decreases significantly, by as much as two orders of magnitude as the temperatures approach the macro-scale melting point.

The most significant component in the reduction of the diffusivity is the specific heat. The specific heat of sea ice is chiefly dependent on the following three components: heat capacity of ice, heat capacity of brine, and the latent heat of the brine-ice phase change from internal brine cells. Heat storage via latent heat gives sea ice an abnormally high specific heat, i.e., at temperatures above -10 °C. Fortunately, the components of specific heat can be described in terms of temperature and the macro-scale salinity (S^I) of sea ice.[23]

Models for the thermal conductivity of sea ice depend chiefly on the thermal conductivity of primary components (pure ice, brine, trapped gas) combined with assumptions on the spatial arrangement of the brine cells and air bubbles. Schwerdtfeger demonstrates that, at temperatures approaching the macro-scale melting point, variations in the thermal conductivity are highly dependent on the salinity (S^I); and that reductions in conductivity over all temperatures are predominantly due to reductions in density. According to Schwerdtfeger, the most important factor in determining the density is the air bubble content. With assumptions on the spatial distribution of brine cells and air bubbles, the thermal conductivity can be expressed in terms of the macro-scale salinity and the macro-scale density.

To model the diffusivity, and hence the thermal behavior of sea ice, it is reasonable to combine models for the thermal conductivity, specific heat, and density. At first glance, use of the diffusivity model requires knowledge of the macro-scale salinity (s^I) and macro-scale density. However, changes in density are reflected by changes in the thermal conductivity such that the diffusivity is relatively indepen-

[23]For details and illustrations related to specific heat, see Schwerdtfeger (1963, Fig.2) and (Yen 1981, Fig.19).

dent of density[24] and hence air content. In other words, a reduction in the amount of material available for conducting heat results in a like reduction in material available for storing heat. As a result, the diffusivity is predominantly a function of salinity.[25]

Snow on the Surface

In many cases, sea ice is covered by a layer of snow during the winter. To understand the effect of a layer of snow, consider the 1-D heat transfer model. In the 1-D case, it is possible to use the analogy of an electrical circuit (Incropera & DeWitt 1981, §5.8). In this case, the components of the diffusivity can be modeled as thermal resistances (R_t) and capacitances (C_t), where

$$R_t = \frac{h}{k} \qquad C_t = \rho c h, \tag{3.115}$$

where h represents the thickness of the component, k its thermal conductivity, ρ its density, and c its specific heat. Then the temperature difference between the top and bottom surfaces is conceptually represented by a voltage that has been imposed across the components.

In these terms, a surface covering of snow will dampen a temperature change in two ways. First the capacitance of the snow will serve to delay any changes in the surface temperature from reaching the sea ice below. Second, the relatively high thermal resistance of a snow cover (R^{sn}) will support a large part of the temperature difference between the top and bottom surfaces. For example, if the temperature difference between the top and bottom surfaces is $\mathcal{T}$, the temperature difference across the sheet of sea ice ($\mathcal{T}^{si}$) at steady state will be

$$\mathcal{T}^{si} = \frac{R^{sn} + R^{si}}{R^{si}} \mathcal{T} \tag{3.116}$$

[24]For an illustration of the relative independence of diffusivity and density, consider Schwerdtfeger (1963, Table VI).

[25]For an illustration of the relation between diffusivity and salinity (s^I), consider Weeks and Ackley (1982, Fig.89).

$$= \frac{h^{si}k^{sn}}{h^{si}k^{sn} + h^{sn}k^{si}}\mathcal{T} \tag{3.117}$$

Suppose the depth of the snow layer is 10 percent of the depth of the snow (h^{sn}) and sea ice (h^{si}) combined. Let the thermal conductivity of the snow (k^{sn}) and sea ice (k^{si}) take values on the order of 0.28 and 2.1 W m^{-1} $°C^{-1}$, respectively (Yen 1981). Then the steady state temperature difference across the sheet of sea ice is only 55 percent of the total temperature difference ($\mathcal{T}$), even though the sea ice makes up 90 percent of the total thickness. As a result, temperature changes at the interface between the sea ice and snow are dampened significantly relative to temperature changes at the surface of the snow.

Surface Temperatures

To define boundary conditions, it is necessary to consider thermal variations at the top surface. Consider a sheet of sea ice that is covered by a layer of snow. On the this subject, Overland & Guest (1991) point out that minimum snow surface temperatures on sea ice result from a net radiative loss balanced by latent heat, from freezing brine, that is conducted from below and a small sensible heat flux from the air to the snow. In essence, the transfer of heat from sea water below the ice moderates decreases in the snow temperature relative to those that would otherwise occur. To emphasize this point, Overland and Guest state that during polar nights, winter temperatures over sea ice often drop to $-30\,°C$ and in rare cases to $-40\,°C$ while temperatures of $-60\,°C$ are reported at Arctic land stations. In addition, Overland and Guest report that, except in very calm conditions, air temperatures (3–10 m above the snow surface) do not differ from snow surface temperatures by more than several degrees.

Application

Combining the heat flow models with the brine cell model, it is possible to evaluate the likely mechanical responses for migrating brine cells in a sheet of sea ice. For the brine cell model, the dominant parameters for modeling a brine cells response are its temperature and cooling rate. The temperature and cooling rate depend primarily on changes in the snow surface temperature combined with variations in the components of diffusivity.

First Year Sea Ice

As a study case for first year sea ice, consider the thermal variations in a model ice sheet, based on data reported by Nakawo & Sinha (1981, Fig.6) for sea ice in Eclipse sound (lat. 72.7° N., long. 78.0° W.), Baffin Island, Canada. For the winter of 1977-78, the snow cover on the ice averaged 11.4 centimeters in depth with a density of 0.35 gm cm^{-3}. Though the salinity of newly formed sea ice was quite high ($\sim$0.025), drainage mechanisms acted to significantly reduce the salinity of the ice within a week after formation. After this initial reduction, the salinity at each given depth maintained a quasi-stable value, decreasing only about 0.0005 per month. Variations in the profile reflected major weather patterns with higher and lower salinities corresponding to ice formation during cold and warm spells, respectively. As the thickness of the ice sheet increased and surface changes were buffered by the ice and snow above the freezing interface, weather patterns were not reflected so dramatically in the rate of ice growth and hence in the developing salinity profile. Except for the top and bottom surfaces, the quasi-stable salinities varied less than 0.003 about an average bulk salinity of 0.006.[26]

For thermal events, Nakawo and Sinha recorded five major cooling-warming

[26]This value for the bulk salinity (0.006) is in agreement with data recorded by Perovich & Gow (1991, Fig.3). Additional salinity data is presented in Weeks & Ackley (1982, Fig.62).

cycles over the winter. For major thermal events, Overland and Guest state that it is common for snow temperatures over sea ice to change by 15 °C due to changing weather systems. Based on thermal profiles recorded in Overland & Guest (1991, Fig.18), these temperature changes typically take 12 or more hours. As a model for changes due to an incoming cold front, assume the snow surface temperature drops from −15 to −30 °C over a period of 12 hours and then remains relatively constant at −30 °C for the next $9\frac{1}{2}$ days.

For thermal parameters, the specific heat (c^{si}) and thermal conductivity (k^{si}) of sea ice were modeled using relationships documented in Yen (1981, Equations 52 and 71). Because the combination of terms defining thermal diffusivity is relatively independent of density variations in sea ice, the density (ρ^{si}) was assumed constant with value of 0.9 gm cm^{-3}. Similarly, the salinity was assumed constant with a value of 0.006, corresponding to the bulk salinity recorded by Nakawo and Sinha. At the same time, the snow covering the sea ice was assumed to maintain a density of 0.35 gm cm^{-3} while the specific heat and thermal conductivity were modeled using relationships also documented in Yen (1981, Table 2 and Equation 35). With these assumptions, the thermal conductivity and specific heat were modeled solely as functions of temperature.

As study depths, the sea ice was modeled with thicknesses of 50 cm and 100 cm with a layer of surface snow that was 10 cm in depth in both cases. To incorporate the temperature dependence of the thermal parameters, the variable cooling rate, and the damping effect of a surface covering of snow, a nonlinear finite element model (ANSYS 1995) was used. The model responses for the 50 and 100 cm ice sheets are shown in Figures 27 and 28, respectively.

For the 50 cm ice sheet, it takes 2.5 hours before the temperature at the snow-ice interface ($z^* = 1$) changes by more than a tenth of a degree. Once the thermal

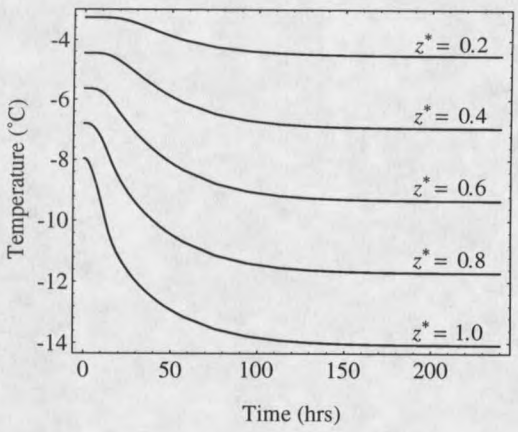

(a) Temperature Profiles

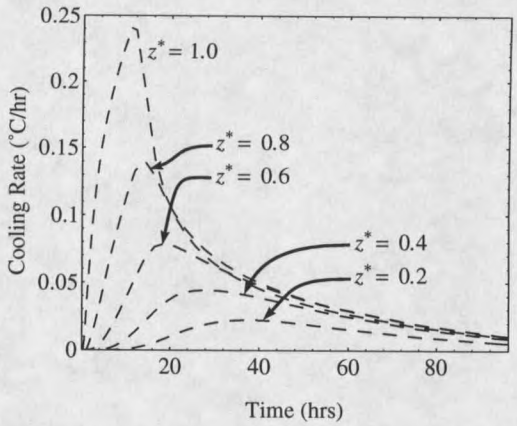

(b) Cooling Rates

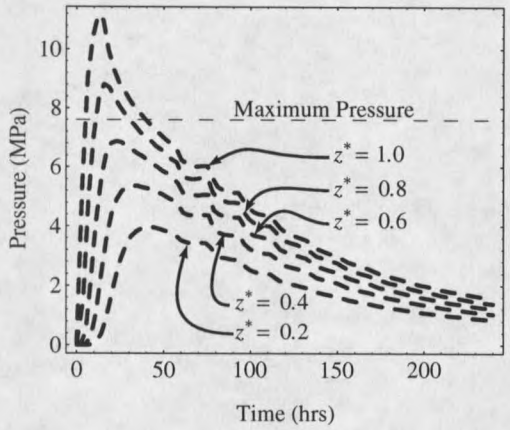

(c) Brine Pressure

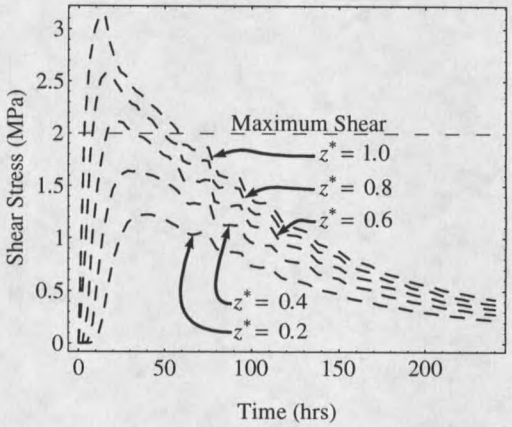

(d) Maximum Shear Stress

Figure 27. Thermally activated responses for a 50 cm snow-covered sheet of sea ice.

change reaches the interface, the temperature at the interface begins to change relatively rapidly (Figure 27a), approaching a maximum cooling rate of $0.24\,^{\circ}\mathrm{C\ hr}^{-1}$ (Figure 27b). At a point 10 cm from the bottom ($z^* = 0.2$), it takes a full day before the temperature changes by more than $0.1\,^{\circ}\mathrm{C}$ and at the same time the maximum cooling rate is more than an order of magnitude less than that at the interface (Figure 27b). Substitution of each respective temperature profile into the brine cell model yields the brine pressure profiles displayed in Figure 27c. If the pressure data recorded by (Visagie 1969) is considered as a rough upper bound on the attainable

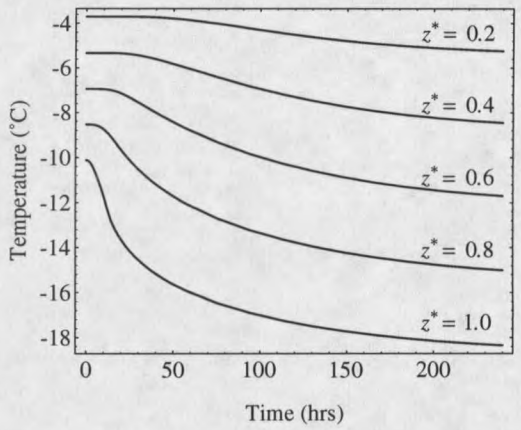

(a) Temperature Profiles

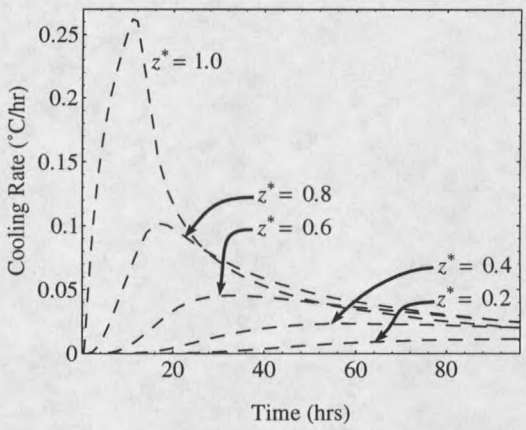

(b) Cooling Rates

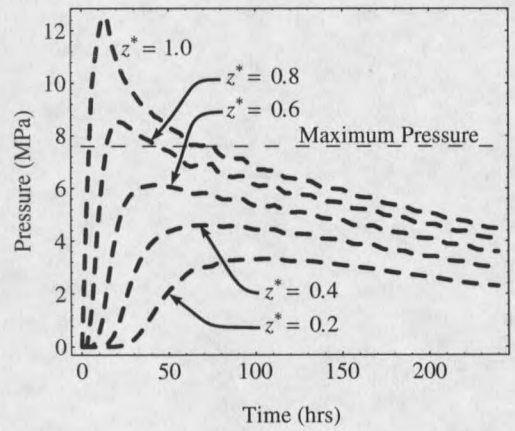

(c) Brine Pressure

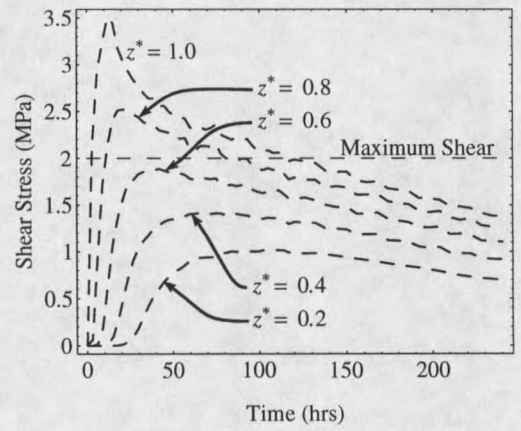

(d) Maximum Shear Stress

Figure 28. Thermally activated responses for a 100 cm snow-covered sheet of sea ice.

brine pressure before micro-cracking develops, then for an incoming cold front that induces snow surface temperatures similar to those in the model, the expansion of brine cells in the top 15 cm is likely to result in micro-cracking. For brine cells in the bottom 35 cm, the expansion mechanism could lead to micro-cracking and/or local inelastic deformation. Toward the bottom of the ice sheet, inelastic deformation is likely to serve as the dominant stress relief mechanism. Notice that similar conclusions result if the maximum basal plane shear stress of 2 MPa is used as a criteria (Figure 27d). In this case, micro-cracking is likely for those brine cells in the top

20 cm, and mixed responses are likely for those brine cells below, depending on the thickness of the cell walls. For smaller changes in the surface temperature, the brine cells near the surface are likely to nucleate dislocations.

Comparing the responses of the model 100 cm ice sheet with those of the 50 cm ice sheet, at the same non-dimensional coordinates, the thermal responses are quite similar. For the 100 cm model, this similarity is due to simultaneous increase in the thermal capacitance and resistance of the ice sheet, corresponding to the increase in the thickness of the ice sheet. The increase in the relative thermal resistance, implies that the ice sheet must carry a larger percentage of the temperature difference. At the same time, because the snow depth is the same in both models, the thermal capacitance of the snow layer is unchanged implying that the time lag between the temperature change at the snow surface and at the snow-ice interface is relatively unchanged.

In summary, for first year sea ice that is covered with a layer of snow on the order of 10 cm in depth, major cold fronts are likely to induce micro-cracking in the top third of the ice sheet. For the middle third of the ice sheet, responses are likely to be mixed depending on the thickness of the walls formed around the brine cells. For the bottom third, the brine cell mechanism is likely to induce inelastic deformation and hence lead to the nucleation of dislocations.

Multi-year Sea Ice

In perennial ice, cooling rates are significantly slower than those in first year ice. These ice sheets are typically greater than 3 meters in depth during the winter months. Based on observations from several drifting stations (Hanson 1965), Untersteiner (1964) estimated that summer ablation was on the order of 30 cm at the surface and 10 cm at the bottom and that the ablated ice was then replaced by accretion at the

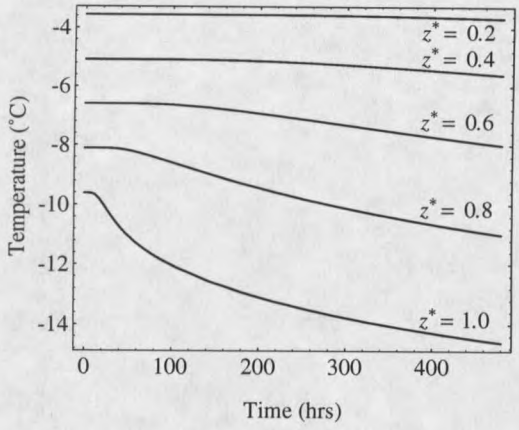

(a) Temperature Profiles

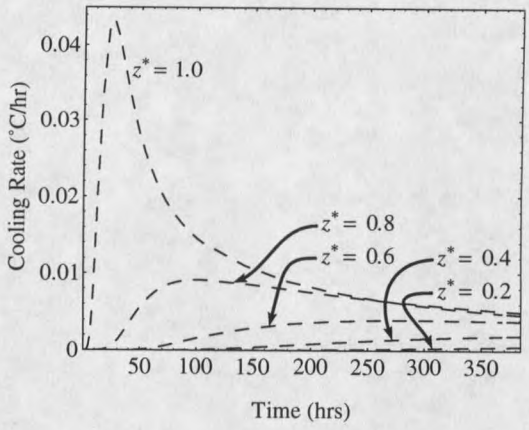

(b) Cooling Rates

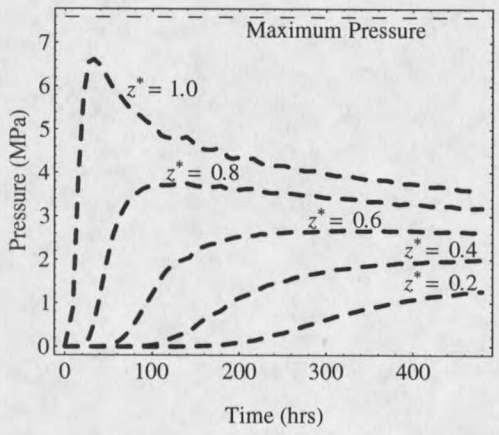

(c) Brine Pressure

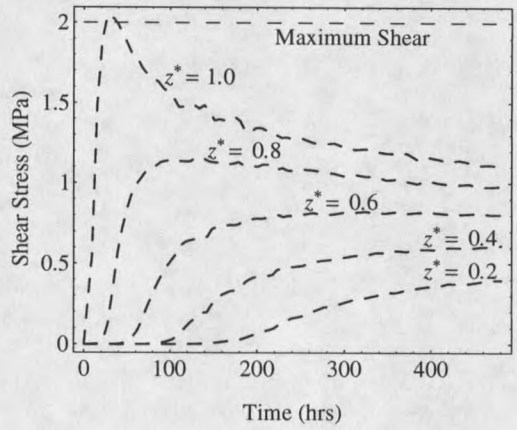

(d) Maximum Shear Stress

Figure 29. Thermally activated responses for a 350 cm snow-covered sheet of sea ice.

bottom during the winter months. The average thickness through this process was on the order of 3.5 meters. Except for any newly accreted ice, the salinity of perennial sea ice (s^I) is on the order of 0.003–0.0035 (Weeks & Ackley 1982, p.63) and tapers to zero near the upper surface (Untersteiner 1964, Fig. 1). Untersteiner stated that, during February, surface snow is typically on the order of 40 cm in depth.

Using these parameters, Untersteiner modeled the mean temperature distribution in an ice sheet throughout a 1 year cycle. However, this model did not include the higher frequency fluctuations due to changing weather systems. For Untersteiner's

geometry with the snow-surface temperature changing from -15 to $-30\,^{\circ}C$ over a period of twelve hours and then remaining relatively constant for another 20 days, the model yields the thermal variations shown in Figure 29.

In the perennial ice model, the cooling rates are severely dampened. The cooling rate at the snow-ice interface is sufficient to introduce probable micro-cracking, but at points near the snow-ice interface the sea ice is relatively brine free. At points well below the interface, the model leads us to believe that sealed brine cells are more likely to induce inelastic deformation and nucleate dislocations than they are to induce micro-cracking.

Migration of Brine Cells

To get a feel for the dynamic role that the phase transformation mechanism might play during the growth of a sheet of saline ice, consider the possible "migration" of a brine cell in a temperature gradient. A migrating brine cell can, over time, affect a larger part of the macroscopic ice matrix than can a stationary brine cell.

A brine cell in a temperature gradient is constantly striving to maintain phase equilibrium. As ice precipitates out at the cold end of a brine cell, the local salinity increases. The local concentration then diffuses toward the warm end of the brine cell, lowering the melting temperature such that ice at the warm end melts to maintain equilibrium. The melt process reduces the local brine concentration and salt will continue to diffuse from the cold end, eventually raising the freezing temperature at the cold end. As a consequence, more ice precipitates out to maintain equilibrium and the process continues. As this process continues, the brine cell migrates toward the highest temperature.

The rate of migration due to a temperature gradient can be characterized in terms of two distinct mechanisms (Tiller 1963). First is the rate of the interface reac-

tions (melting or freezing) which serve to maintain local phase equilibrium. Second is the rate of solute transport (diffusion) from the cold interface to the warm interface as a result of the solute gradient produced by the first mechanism. For temperatures near $-10\,^{\circ}\mathrm{C}$ and presumably lower, the limiting factor is the diffusion rate of salt in brine (Jones 1973).

This diffusion velocity (v_b), based on Fick's law (Weeks & Ackley 1982, p. 78), can be modeled by

$$v_b = \frac{D}{s^B}\frac{ds^B}{dT}\underbrace{\frac{dT}{dz}}_{local} \tag{3.118}$$

where D the diffusion coefficient for salt in a brine solution. This diffusion velocity then reflects the velocity of the migrating brine cell.

Because the model assumes the existence of two phases (brine and ice), the salinity (s^B) must approach zero as local temperatures approach $0\,^{\circ}\mathrm{C}$. As a result, this diffusion based model (3.118) has a singularity at $0\,^{\circ}\mathrm{C}$ and will not yield a reasonable approximation near $0\,^{\circ}\mathrm{C}$. For temperatures near $0\,^{\circ}\mathrm{C}$, the model developed by Tiller (1969), which includes interface reactions, would yield a better estimate. Because temperatures in sea ice are typically below $-2\,^{\circ}\mathrm{C}$, the diffusion based model will serve as a reasonable approximation.

Because the thermal conductivity of ice (k^I) is about four times the thermal conductivity of the brine (k^B), the local temperature gradient in the brine cell will be different than the macroscopic temperature gradient. Tiller (1963) related the local gradient to the macroscopic gradient using Laplace's equation for spheres. Seidensticker (1966) used an approximation of Tiller's solution and included a density correction factor allowing the diffusion velocity to be expressed in terms of the macroscopic temperature gradient as follows:

$$v_b = \frac{D}{s^B}\frac{ds^B}{dT}\left(\frac{3k^I}{2k^I + k^B}\right)\left(\frac{\rho^B}{\rho^I}\right)\underbrace{\frac{dT}{dZ}}_{macro} \approx 1.46\frac{D}{s^B}\frac{ds^B}{dT}\frac{dT}{dZ} \tag{3.119}$$

In terms of the macroscopic temperature gradient (dT/dZ), both Hoekstra, Osterkamp & Weeks (1965) and (Jones 1973) recorded data that indicate that the velocity of a brine cell at each temperature is proportional to dT/dZ, at least for gradients between 0.5 and 4 °C hr^{-1} with a local temperature near −10 °C.

As Seidensticker pointed out, there is relatively little data for the diffusion coefficient (D) of NaCl in brine at low temperatures. However, he was able to derive temperature dependent values for D based on the conductivity of brine. With these values for the diffusion coefficient and the model above, he compared the predicted values with the measured values of Hoekstra et al. (1965), based on a unit temperature gradient. The trends between the model and the data matched, but the model over predicted the measured values by 20%. Seidensticker attributed the difference to the uncertainty in diffusion coefficient.

Because the data of Hoekstra et al. (1965) is fairly representative of the case of interest and reliable diffusion coefficient data could not be located for low temperatures, a simple empirical approach was used to improve the accuracy of the model. To capture the temperature dependent trend of the diffusion coefficient, a linear fit was applied to the values recorded by Seidensticker (1966). The diffusion coefficient was then multiplied by an arbitrary constant which was defined by applying a least squares match between the model (3.119) and the empirical data (Hoekstra et al. 1965). The least squares match, based on seven points, gave a correlation coefficient of 0.997 and a standard error of 0.020 microns hr^{-1}. The resulting approximation for the diffusion coefficient is $D = (5.47 + 22.3T) \times 10^{-6}$ cm^2 sec^{-1} where T is in °C.

Kingery & Goodnow (1963) experimentally evaluated the migration of brine cells using 56 samples of arctic sea ice. Their samples were four inches thick with a temperature of −5 °C at the top surface and −20 °C at the bottom surface so that the brine cells had to migrate against gravity. With these conditions, Kingery and

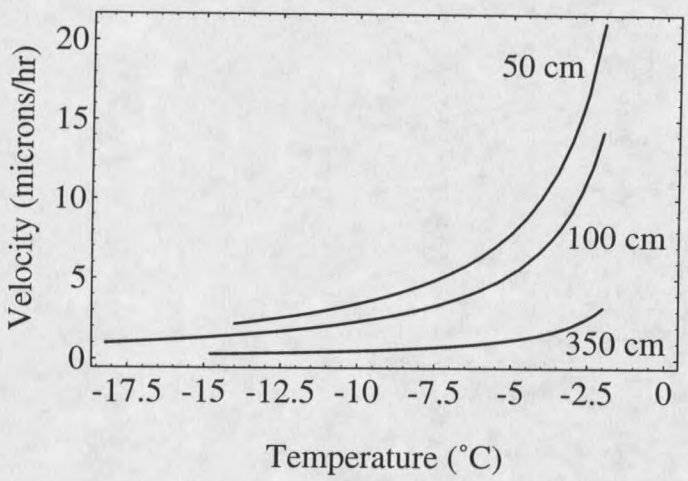

Figure 30. Brine cell migration velocities in the model ice sheets

Goodnow observed a range of brine cell velocities. The most frequently observed velocity was on the order of 2 microns per hour; however, velocities ranged as high as 30.6 μ hr^{-1} with a mean velocity of 7.9 μ hr^{-1}, where the mean is biased toward the higher velocities. Assuming very little data was recorded near the top and bottom surfaces, the model can be integrated over the temperature range between -7 and $-18\,^{\circ}$C to obtain a mean cell velocity of 17 μ hr^{-1}. Comparing this with the mean velocity observed by Kingery and Goodnow indicates that the model may overestimate the velocity of a brine cell in general, but will at least provide the right order of magnitude.

If this migration model is applied to the example ice sheet cases, a range of migration velocities is obtained, Figure 30. As illustrated in Figure 30, brine cells located near the bottom of an ice sheet can be significantly more mobile. In first year ice, brine cells can be quite mobile throughout the entire ice sheet, particularly early in the season as reflected by the 50 cm case.

Because brine cells in a sheet of sea ice will migrate, each bulk temperature decrease will produce local deformation in a different part of the ice matrix.

Range of Local Deformation

For a better understanding of the geometrical significance of the local deformation imposed by phase transformations, consider the geometry of the ice matrix.

For the spatial distribution of brine cells in sea ice, Anderson & Weeks (1958) recorded initial cell diameters on the order of 0.07 mm with platelet thicknesses on the order of 0.46 mm and a diametral spacing between brine cells in the brine layer on the order of 0.23 mm. Given the relative spacing between brine cells, it is possible that a significant part of the ice matrix yields with each small temperature decrease.

In the finite element models, inelastic deformation in the neighborhood of a brine cell was significant at distances up to five times the radius of the brine cell. In light of the tight spatial distribution of brine cells combined with their mobility in a temperature gradient, it is not unreasonable to assume that two or three bulk cooling cycles can lead to the introduction of a steady state mobile dislocation density without the application of an external stress.

CHAPTER 4

CONCLUSIONS AND FUTURE RESEARCH

Much of what is discussed in this dissertation is physically significant for an understanding the mechanical behavior of saline (NaCl) ice and sea ice. In particular, this dissertation addresses a physical process that is potentially responsible for variations in the initial compliance of saline ice and sea ice.

Review of New Observations

For new issues, this dissertation presents mathematical models for the expansion of encapsulated brine as evidence that such a mechanism can act as a source for variations in the observed structural response of saline ice. These models also provide evidence that such a mechanism might also explain some of the more significant differences between the initial responses of saline and non-saline ice. In particular, this dissertation addresses the problem of whether or not phase transformations in brine cells can be responsible for the generation of dislocations.

Elastic models indicate that the stresses that can be reached due to freezing of water from brine in these pockets can, due to expansion, produce stresses of sufficient magnitude to nucleate and multiply dislocations. Combined elastic and inelastic models indicate that even small changes in temperature are capable of inducing extensive microscopic deformation in the neighborhood of a brine cell. These results are in agreement with experimental observations of strain figures near brine cells.

To identify the resulting changes in the ice near a brine cell, the modes of deformation can be divided into two classes, i.e., fracture and inelastic deformation.

The structural brine cell model indicates that, if a brine cell cools at a rate on the order of $0.1\,^{\circ}\mathrm{C\ hr^{-1}}$ or faster, the structural response is likely to be fracture dominated. For cooling rates slower than $\sim 0.1\,^{\circ}\mathrm{C\ hr^{-1}}$, the pressure build up occurs slowly enough that thermally activated dislocations have time to act and provide a mode of stress relief.

For first year sea ice with a light covering of snow ($\sim$10 cm), the model indicates that major cold fronts, cooling the surface on the order of $-15\,^{\circ}\mathrm{C}$ in 12 hours, will induce microcracking in the top third of an ice sheet. In the middle third there is likely to be a combination of microcracking and dislocation nucleation, depending on the thickness of the cell walls. In the bottom third, phase transformations are likely to nucleate dislocations as a result of the reduction in temperature. At the same time, smaller changes in the surface temperature, can provide a mechanism for introducing dislocations in the upper sections of the ice sheet.

In perennial ice with relatively thick snow cover ($\sim$40 cm), major temperature changes in surface temperatures are likely to induce a combination of microcracking and dislocation nucleation. In the bottom half of the ice sheet, inelastic deformation should serve as the dominant relaxation mechanism.

In ice that is under a temperature gradient, brine cells are likely to migrate. In natural sea ice, migration models indicate that migration velocities are relatively small ($\sim 10\ \mu\mathrm{m\ hr^{-1}}$); however, because the mean distance between brine cells is also small ($\sim 230\ \mu$m), the dynamic nature of migration implies that the phase transformation mechanism can, over a period of time, affect a significant fraction of the ice structure.

Once dislocations begin to nucleate, stress relaxation occurs; as freezing continues, inelastic deformation continues. Eventually, a quasi-equilibrium balance between expansion and relaxation processes may be reached, rendering stresses substantially lower than those calculated here. This balance, of course, depends on the rate of

cooling, the cooling patterns, and, in general, the temperature history of the total brine/ice system.

This dissertation provides an outline of the complex interactions that affect the structural response of a brine cell and its probable role in the macroscopic behavior of sea ice. In essence, the brine cell mechanism has the ability, with a suitable temperature history, to introduce a stationary (annealed) dislocation density and a multitude of microcracks. In this regard, this dissertation provides evidence that phase transformations can play a significant role in the macroscopic behavior of saline (sea) ice.

Avenues for Future Research

By demonstrating the range of possible variations for the initial dislocation density of ice, this dissertation, in a sense, lays a firmer foundation for at least two other avenues of study. The first avenue involves the collection of experimental data to either confirm or refute the importance of the phase transformation mechanism. The second avenue involves the pursuit of a mechanism-based model for the structural behavior of saline ice with a recognition of the possible variations in the initial dislocation density.

Following is a list of possible branches of these two avenues of research that will add to our understanding of the structural behavior of saline ice, relative to non-saline ice.

I. *Using experimental methods, evaluate the structural behavior of saline (sea) ice with respect to varied growth and storage (thermal) histories.* Based on results presented in this dissertation, it appears highly probable that variations in the thermal history of sea ice can lead to significant variations in the microstructure

of sea ice. In particular, varied cooling rates can lead to variations in mobile dislocation densities and micro-crack densities. Possible studies include:

- *Evaluate, experimentally, the dependence of brine cell pressure on temperature history.* Using a single crystal of non-saline ice, build a "large" scale brine cavity. Fill the cavity with brine of a known salinity. Insert a pressure transducer and a thermocouple, then allow the "brine cell" to seal. Monitor the pressure in the brine cell corresponding to known temperature histories. Compare the experimental pressure profile with the modeled pressure profile based on the known temperature history.
- *Evaluate the dependence of structural behavior on temperature history.* MSU now has the tools to grow quasi-single saline and non-saline crystals at a nearly constant temperature. Crystals grown under constant temperatures can be used to evaluate significant changes in macroscopic structural behavior of sea ice for varied thermal histories. It would not be difficult to vary thermal histories of specimens and correlate these thermal variations with variations in the structural response. Any significant changes can then be evaluated in light of models presented in this dissertation.
- *Compare structural behavior of quasi-single crystals of sea ice and bubbly ice.* To further establish the role of phase transformations in the inelastic behavior of saline (sea) ice, we can compare the behavior of quasi-single crystals of saline ice and bubbly ice, taking into consideration the differences in the ice geometry-connectivity. Again, any significant differences in the behavior of these two forms of ice can be evaluated in light of models presented in this dissertation.[27]

[27]This test was suggested by Dave Cole at CRREL.

II. *Build a mechanism-based constitutive equation for the multiaxial deformation of non-saline ice.* Most constitutive equations are based on gross macroscopic assumptions of the microscopic nature of ice and lend little physical insight into the underlying nature of ice. For a mechanism based model, it should not be difficult to:

- *apply knowledge of variations in initial mobile dislocation densities,*
- *include coupling between basal and non-basal dislocations based on single crystal data, and*
- *include evolution of mobile dislocation densities.*

By acknowledging possible variations in the initial dislocation density of saline ice, it should not be difficult to extend a model for non-saline ice to saline ice.

III. *Build a statistical model for the geometry of sea (saline) ice.* The model presented by Assur (1958), i.e., ice with individual brine cells, seems to work reasonably well for macroscopic models at colder temperatures. However, this model does not characterize the platy-mosaic structure that will most likely be important for micro-structurally based models. In particular, it seems worthwhile to develop the geometry and coordination of the connections between platelets using three dimensional techniques possibly combined with quantitative stereology and shape skeleton techniques. Worthwhile geometric models include:

- *a statistical model for 3-D bridging-connectivity between "pure" ice platelets,*
- *a statistical model for 3-D platelet connectivity-geometry with dependence on growth rate, and*

- *a statistical model for 3-D platelet connectivity-geometry with dependence on temperature history.*

IV. *Build a continuum model for sea ice based on statistical connectivity of ice platelets.* Using experimental results on the platelet geometry-connectivity, we can develop a more accurate microstructure-based continuum model for the macroscopic deformation of sea ice.

REFERENCES CITED

Anderson, D. L. (1958). A model for determining sea ice properties, *Arctic Sea Ice*, U.S. National Academy of Sciences - National Research Council, Pub. 598, pp. 148–156.

Anderson, D. L. & Weeks, W. F. (1958). A theoretical analysis of sea-ice strength, *EOS, Transactions, American Geophysical Union* **39**(4): 632–640.

ANSYS (1995). *Engineering Analysis System*, Swanson Analysis Systems, Inc., Houston, Pennsylvania. Revision 5.2.

Assur, A. (1958). Composition of sea ice and its tensile strength, *Arctic Sea Ice*, U.S. National Academy of Sciences - National Research Council, Pub. 598, pp. 106–138.

Atkinson, K. E. (1989). *An Introduction to Numerical Analysis*, 2nd edn, Wiley, New York.

Bennington, K. O. (1963). Some crystal growth features of sea ice, *Journal of Glaciology* **4**(36): 669–688.

Brown, R. & Kawamura, T. (1991). A preliminary comparison of the properties of pure ice and sea ice single crystals, *Cold Regions Science and Technology* **19**: 275–284.

Cole, D. M. (1995). A model for the anelastic straining of saline ice subjected to cyclic loading, *Philosophical Magazine A* **72**(1): 231–248.

Cox, G. & Weeks, W. (1975). Brine drainage and initial salt entrapment in sodium chloride ice, *Research Report 345*, USA Cold Regions Research and Engineering Laboratory, Hanover, New Hampshire.

Cox, G. & Weeks, W. (1983). Equations for determining the gas and brine volumes in sea-ice samples, *Journal of Glaciology* **29**(102): 306–316.

Dantl, G. (1968). Die elastichen moduln von eis-einkristallen, *Physics of Condensed Matter* **7**: 390–397.

Dantl, G. (1969). Elastic moduli of ice, *in* N. Riehl, B. Bullemer & H. Engelhardt (eds), *Physics of Ice*, Plenum Press, New York, pp. 223–230.

Derradji-Aouat, A. (1992). *Mathematical Modelling of Monotonic and Cyclic Behaviour of Polycrystalline Fresh Water Ice*, PhD thesis, University of Ottawa, Dept. of Civil Engineering, Ottawa, Canada.

Duval, P., Ashby, M. & Anderman, I. (1983). Rate controlling processes in the creep of polycrystalline ice, *The Journal of Physical Chemistry* **87**(21): 4066–4074.

Finnie, I. & Heller, W. (1959). *Creep of Engineering Materials*, McGraw-Hill, New York.

Fletcher, N. (1970). *The Chemical Physics of Ice*, Cambridge University Press, Cambridge, p. 271.

Frost, H. & Ashby, M. (1982). *Deformation-Mechanism Maps*, Pergamon Press, Oxford.

Glen, J. (1953). The creep of polycrystalline ice, *Proceedings of the Royal Society of London, Ser. A* **228**(1175): 519–538.

Gold, L. (1958). Some observations on the dependence of strain on stress for ice, *Canadian Journal Physics* **36**: 1265–1275.

Goodman, D., Frost, H. & Ashby, M. (1981). The plasticity of polycrystalline ice, *Philosophical Magazine* **43**(3): 665–695.

Grenfell, T. C. (1983). A theoretical model of the optical properties of sea ice in the visible and near infrared, *Journal of Geophysical Research* **88**(C14): 9723–9735.

Gupta, V., Picu, R. & Frost, H. (1993). Crack nucleation mechanism in saline ice, *Ice Mechanics, AMD-Vol. 163*, American Society for Mechanical Engineers, Applied Mechanics Division, New York, pp. 199–215. Proceedings of the First Joint Mechanics Meeting of the American Society of Mechanical Engineers, the American Society of Civil Engineers, and the Society of Engineering Science.

Hamming, R. (1973). *Numerical Methods for Scientists and Engineers*, 2nd edn, Dover, New York.

Hanson, A. (1965). Studies of the mass budget of Arctic pack-ice floes, *Journal of Glaciology* **5**: 701–709.

Harrison, J. & Tiller, W. (1963). Controlled freezing of water, *in* W. Kingery (ed.), *Ice and Snow: Properties, Processes, and Applications*, M.I.T. Press, Cambridge, Mass, pp. 215–225.

Higashi, A. (1966). Mechanisms of plastic deformation in ice single crystals, *in* H. Oura (ed.), *Physics of Snow and Ice*, Institute of Low Temperature Science, International Conference on Low Temperature Science, I. Conference on Physics of Snow and Ice, Hokkaido University, Sapporo, Japan, pp. 277–289.

Higashi, A., Koinuma, S. & Mae, S. (1964). Plastic yielding in ice single crystals, *Japanese Journal of Applied Physics* **3**(10): 610–616.

Higuchi, K. (1958). Etching of ice crystals, *Acta Metallurgica* **6**(10): 636–642.

Higuchi, K. & Muguruma, J. (1958). Etching of ice crystals by the use of plastic replica film, *Journal of the Faculty of Science* **1**(2): 81–95. Hokkaido University, Japan, Series VII.

Hirth, J. P. & Lothe, J. (1982). *Theory of Dislocations*, Wiley, New York.

Hobbs, P. (1974). *Ice Physics*, Clarendon Press, Oxford, pp. 434–441. Section 6.7: Surface Energies of Ice.

Hoekstra, P., Osterkamp, T. & Weeks, W. (1965). The migration of liquid inclusions in single ice crystals, *Journal of Geophysical Research* **70**(20): 5035–5041.

Hull, D. & Bacon, D. (1984). *Introduction to Dislocations*, Pergamon Press, New York.

Hutchinson, J. W. (1977). Creep and plasticity of hexagonal polycrystals as related to single crystal slip, *MECH-1*, Division of Engineering and Applied Mechanics, Harvard University, Cambridge, Massachusetts.

Incropera, F. & DeWitt, D. (1981). *Fundamentals of Heat Transfer*, Wiley, New York.

Jones, D. (1973). The temperature-gradient migration of liquid droplets through ice, *Journal of Crystal Growth* **20**: 145–151.

Kawamura, T. (1986). A method for growing large single crystals of sea ice, *Journal of Glaciology* **32**(111): 302–303.

Kingery, W. & Goodnow, W. (1963). Brine migration in salt ice, *in* W. Kingery (ed.), *Ice and Snow: Properties, Processes, and Applications*, M.I.T. Press, Cambridge, Mass, pp. 237–247.

Knight, C. (1962). Polygonization of aged sea ice, *Journal of Geology* **70**(2): 240–246.

Lake, R. & Lewis, E. (1970). Salt rejection by sea ice during growth, *Journal of Geophysical Research* **75**(3): 583–597.

Love, A. (1944). *A Treatise on the Mathematical Theory of Elasticity*, Dover, New York.

McKittrick, L. & Brown, R. (1993). On the effect of phase transformations and dislocation density gradients on saline ice compliance, *Ice Mechanics, AMD-Vol. 163*, American Society for Mechanical Engineers, Applied Mechanics Division, New York, pp. 189–198. Proceedings of the First Joint Mechanics Meeting of the American Society of Mechanical Engineers, the American Society of Civil Engineers, and the Society of Engineering Science.

Mellor, M. & Cole, D. (1982). Deformation and failure of ice under constant stress or constant strain-rate, *Cold Regions Science and Technology* **5**: 201–219.

Mellor, M. & Cole, D. (1983). Stress/strain/time relations for ice under uniaxial compression, *Cold Regions Science and Technology* **6**: 207–230.

Mendelson, A. (1968). *Plasticity: Theory and Application*, Krieger, Malabar, Florida.

Michel, B. (1978). *Ice Mechanics*, Les Presses De L'Universite Laval, Quebec.

Nakawo, M. & Sinha, N. (1981). Growth rate and salinity profile of first-year sea ice in the high Arctic, *Journal of Glaciology* **27**(96): 315–330.

Nakaya, U. (1956). Properties of single crystals of ice, revealed by internal melting, *Research Report 13*, U.S. Army Snow, Ice, and Permafrost Research Establishment.

Overland, J. E. & Guest, P. S. (1991). The arctic snow and air temperature budget over sea ice during winter, *Journal of Geophysical Research, C* **96**(3): 4651–4662.

Perovich, D. & Gow, A. (1991). A statistical description of the microstructure of young sea ice, *Journal of Geophysical Research* **96**(C9): 16,943–16,953.

Peyton, H. (1966). Sea ice strength, *Technical Report UAG R-182*, Geophysical Institute of the University of Alaska.

Picu, R., Gupta, V. & Frost, H. (1994). Crack nucleation mechanism in saline ice, *Journal of Geophysical Research* **99**(B6): 11775–11786.

Pounder, E. (1960). Heat flow in ice sheets and cylinders, *Publication 46*, International Association of Scientific Hydrology.

Pounder, E. (1965). *The Physics of Ice*, Pergamon Press, Oxford.

Rist, M., Jones, S. & Slade, T. (1994). Microcracking and shear fracture in ice, *Annals of Glaciology* **19**: 131–137.

Rist, M. & Murrell, S. (1994). Ice triaxial deformation and fracture, *Journal of Glaciology* **40**(135): 305–317.

Savitzky, A. & Golay, M. (1964). Smoothing and differentiation of data by simplified least squares procedures, *Analytical Chemistry* **36**: 1628–1639.

Schwerdtfeger, P. (1963). The thermal properties of sea ice, *Journal of Glaciology* **4**(36): 789–807.

Seidensticker, R. (1966). Comment on paper by P. Hoekstra, T.E. Osterkamp, and W.F. Weeks, 'the migration of liquid inclusions in single ice crystals', *Journal of Geophysical Research* **71**(8): 2180–2181.

Sinha, N. (1977). Instruments and methods: Technique for studying structure of sea ice, *Journal of Glaciology* **18**(79): 315–323.

Sinha, N. (1979). Grain boundary sliding in polycrystalline materials, *Philosophical Magazine A* **40**(6): 825–842.

Taylor, G. (1938). Plastic strain in metals, *Journal of the Institute of Metals* **62**: 307–324.

Tiller, W. (1963). Migration of a liquid zone through a solid: Part I, *Journal of Applied Physics* **34**(9): 2757–2762.

Tiller, W. (1969). Migration of a liquid zone through a solid, *Journal of Crystal Growth* **6**: 77–85.

Timoshenko, S. & Goodier, J. (1970). *Theory of Elasticity*, 3rd edn, McGraw-Hill, New York.

Untersteiner, N. (1964). Calculations of temperature regime and heat budget of sea ice in the central Arctic, *Journal of Geophysical Research* **69**(22): 4755–4766.

Vassoille, R., Mai, C. & Perez, J. (1978). Inelastic behavior of ice single crystals in the low frequency range due to dislocations, *Journal of Glaciology* **21**(85): 375–384.

Visagie, P. (1969). Pressures inside freezing water drops, *Journal of Glaciology* **8**(53): 301–309.

von Mises, R. (1928). *Z. angew. Math. Mech.* **8**: 161–.

Wakahama, G. (1966). On the plastic deformation of single crystal of ice, *in* H. Oura (ed.), *Physics of Snow and Ice*, Institute of Low Temperature Science, International Conference on Low Temperature Science, I. Conference on Physics of Snow and Ice, Hokkaido University, Sapporo, Japan, pp. 291–311.

Weeks, W. & Ackley, S. (1982). The growth, structure, and properties of sea ice, *CRREL Monograph 82-1*, USA Cold Regions Research and Engineering Laboratory, Hanover, New Hampshire.

Weeks, W. & Assur, A. (1967). The mechanical properties of sea ice, *CRREL Monograph II-B3*, USA Cold Regions Research and Engineering Laboratory, Hanover, New Hampshire.

Weiss, R. (1970). The solubility of nitrogen, oxygen and argon in water and seawater, *Deep-Sea Research* **17**: 721–735.

Wilkinson, D. & Ashby, M. (1975). Pressure sintering by power law creep, *Acta Metallurgica* **23**: 1277–1285.

Winegard, W. (1964). *An Introduction to the Solidification of Metals*, The Institute of Metals, London.

Yen, Y.-C. (1981). Review of thermal properties of snow, ice and sea ice, *CRREL Report 81-10*, USA Cold Regions Research and Engineering Laboratory, Hanover, New Hampshire.